

Lifetime Measurements in $^{62,64,66}\text{Fe}$

Inaugural-Dissertation

zur

Erlangung des Doktorgrades

der Mathematisch-Naturwissenschaftlichen Fakultät

der Universität zu Köln

vorgelegt von

Wolfram Rother

aus

Krefeld

Verlag Dr. Hut, München

2011

Gutachter:

Prof. Dr. Jan Jolie

Priv.-Doz. Dr. Alfred Dewald

Tag der mündlichen Prüfung:

08. April 2011

Abstract

This work reports on model-independent lifetime measurements of the 2_1^+ states in $^{62,64,66}\text{Fe}$ at the National Superconducting Cyclotron Laboratory. While confirming the known value for ^{62}Fe , the experiment on ^{64}Fe could reduce the experimental error on ^{64}Fe significantly. The lifetime of the 2_1^+ state in ^{66}Fe was not known beforehand. Excited states were populated by inverse kinematics Coulomb excitation after projectile fragmentation.

To account for Doppler shift attenuation in target and degrader, relativistic Lorentz Boost and solid angle related effects, a dedicated simulation tool was written. The program reproduces the line-shape of detected γ -rays using a discretisation approach.

Collectivity around $N = 40$ is discussed based on the new and on older $B(E2)$ data. The new values confirm the rising collectivity in iron isotopes at $N = 38$, that was recently reported. More so, the drastic reduction of the experimental error puts this statement on a sound footing. The present data on ^{66}Fe were the first to show the persistence of enhanced collectivity in the iron chain at $N = 40$.

While numerical calculations for this region of the nuclear chart were not successful in the past, the purely phenomenological approach of the modified Valence Proton Symmetry yields a rather good description of collective nuclei around $N = 40$.

The state-of-the-art effective LNPS interaction is basis for a beautiful shell-model description of the new data set. Improvements on the interaction and on the computational power side allow for a very detailed description of collective nuclei far from the valley of stability.

Kurzzusammenfassung

Im Rahmen dieser Arbeit wurden Lebensdauermessungen der 2_1^+ Zustände in $^{62,64,66}\text{Fe}$ durchgeführt. Neben einer Bestätigung des bekannten Wertes für ^{62}Fe , war es möglich, den vorliegenden Wert für ^{64}Fe mit einem erheblich kleineren experimentellen Fehler zu messen. Die 2_1^+ Lebensdauer in ^{66}Fe wurde erstmals im Rahmen der hier beschriebenen Experimente bestimmt.

Alle drei Kerne wurden als schnelle Fragmente am National Superconducting Cyclotron Laboratory, Michigan State University zur Verfügung gestellt. Die 2_1^+ Zustände wurden durch inverse Coulomb Anregung bevölkert.

Zur Auswertung der gewonnenen γ -Spektren wurde eine Linienformsimulation geschrieben. Sie berücksichtigt die Abschwächung der Dopplerverschiebung in Target und Degradier, den relativistischen Lorentz Boost und die Änderung des vom Detektor bedeckten Raumwinkels. Die Zahl der Diskretisierungsschritte ist nunmehr frei wählbar. Im vorliegenden Fall waren 36 Schritte ausreichend.

Auf Basis der neuen und den in der Literatur vorhandenen $B(E2)$ Werten wird die Kollektivität in der Massenregion um $N = 40$ diskutiert. Die zunehmende Kollektivität in der Eisenreihe bei $N = 38$, ^{64}Fe , kann durch den neuen Messwert bestätigt werden. Durch den drastisch kleineren Fehler ist diese Aussage nun deutlich belastbarer als zuvor. Die dieser Arbeit zugrunde liegenden Experimente ermöglichen erstmals eine Aussage über die Kollektivität bei $N = 40$. Tatsächlich zeigt auch der 2_1^+ Zustand in ^{66}Fe stark kollektive Züge.

Diese Massenregion entzog sich bis dato weitgehend (erfolgreichen) fundamentalen numerischen Ansätzen. Als rein phänomenologische Beschreibung liefert die modifizierte Valence Proton Symmetry (VPS) eine vollständig parameterfreie Beschreibung der kollektiven Kerne der Region.

Die Übereinstimmung mit Schalenmodellrechnungen unter Verwendung der modernsten effektiven Wechselwirkung für diese Region (LNPS) wird zum Abschluss der Arbeit betrachtet. Die Resultate beider Ansätze werden mit den experimentellen Werten verglichen. Die VPS zeigt eine gute Übereinstimmung mit dem Experiment und ist in der Lage, das generelle Verhalten in der Massenregion um $N = 40$ zu beschreiben. Zukünftige Messungen werden zeigen, ob dieser rein phänomenologische Ansatz Vorhersagekraft hat. Die Schalenmodellrechnungen auf Basis der LNPS-Wechselwirkung liegen in nie dagewesener Nähe zu den experimentellen Daten in einer Region der Nuklidkarte, die zuvor nicht erfolgreich durch Schalenmodellrechnungen erfasst werden konnte.

Contents

1	Introduction	7
2	Experimental Setup	11
2.1	Beam Preparation	12
2.2	SeGA	13
2.3	RDDS	14
2.4	Target and Degradar	16
2.5	The S800 Spectrograph	24
3	Data Preparation	29
3.1	Particle Identification	29
3.1.1	S800-Calibrations	30
3.1.2	PID-IN	32
3.1.3	PID-OUT	35
3.2	Calibration of γ -Spectra	40
4	Lifetime Analysis	45
4.1	Discretisation	47
4.2	Calibration of Angles	49
4.3	Normalisation	50
4.4	Excitation Ratio	51
4.5	Solid Angle Coverage	53
4.6	Final Results	55

5	Discussion	63
5.1	Placement of Results	63
5.2	Interpretation of Results	65
5.2.1	Valence Proton Symmetry	67
5.2.2	Shell Model	71
5.3	Summary	75
A	Lineshape Simulation	77
A.1	General Considerations	77
A.2	The Amplitudes	78
A.2.1	Excitation	78
A.2.2	Angles	83
A.2.3	Energies	85
A.2.4	Efficiencies	86
A.3	Spectra	87
A.3.1	Individual segments	87
A.3.2	Lineshape Function	88
	Bibliography	89

Chapter 1

Introduction

The nuclear shell model provides a basis for the description of nuclear structure. Densely packed nucleons move quasi freely at distances of the nuclear force's range in an average potential. While the parameters describing the average potential and therefore the ordering of the shells, including collective mode and deformation, have been known for half a century [35], the details are still on empirical grounds.

The energies of nuclear orbits, single-particle energies, have been known to change over the nuclear landscape for some time, as do the magic numbers in exotic nuclear matter [13, 41, 49]. Consequently, the community's focus has shifted towards more and more exotic, that is less stable, nuclei. The prevalent production methods for such nuclei are projectile fragmentation and isotope separation online (for a brief overview please see [12]. For a detailed review of fragmentation see [38]).

Nuclear level lifetimes are next to level energy, spin and parity key observables for nuclear structure studies. The experiments discussed in this work aimed at measuring level lifetimes of the first excited states in the exotic nuclei $^{62,64,66}\text{Fe}$. The following chapters give a detailed account of the measurement, the analysis and the interpretation of the obtained results.

Chapter 2 presents the experimental setup used at the National Superconducting Cyclotron Laboratory to perform the experiments described in this work. The particles of interest were produced by projectile fragmentation. Fragmentation

reactions yield so called cocktail-beams that make purification and particle identification methods necessary. Production and purification are discussed in Section 2.1. The first 2^+ states were excited by projectile Coulomb excitation. γ -rays emitted by the nuclei of interest were detected by the Segmented Germanium Array (SeGA), discussed in Section 2.2. The method of choice to measure level lifetimes in the picosecond-range is the Recoil Distance Doppler Shift (RDDS) method. A detailed discussion is given in Section 2.3. Further experimental parameters to be addressed are the reaction targets. The RDDS method uses two, a target and a degrader, their choice is not trivial, cf. Section 2.4.

The starting point of any data analysis—in the sense of extracting the desired quantities out of a data set—is the data preparation which is described in detail in Chapter 3. Although the cocktail beam has basically only two components (cf. Figures 3.3, 3.4) and the reaction is very simple (there is no other reaction channel), the offline identification of particles is not trivial. The data stream is first separated on incoming (Section 3.1.2) and then on outgoing particles (Section 3.1.3) while applying a series of calibrations and empirical corrections to the data (Section 3.1.1). The purity of the final result compared to the raw data is striking. So far the focus of this work has been on particle spectroscopy even though it actually deals with γ -spectroscopy. This will change from now on starting with Section 3.2 discussing the energy and efficiency calibration of the used γ -ray spectra and the applied Doppler-correction.

Finally, Chapter 4 addresses the main purpose of this work, the lifetime analysis. Based on previous work of Starosta et al. [43] and Dewald et al. [17], a dedicated lineshape simulation for the analysis of RDDS experiments at intermediate beam energies was used to extract lifetimes of the 2_1^+ states in $^{62,64,66}\text{Fe}$. Further details of the analysis procedure are given in Appendix A. The new computer code written in this work for the analysis at hand is the first to implement this simulation in its full generality. Chapter 4 leads through the analysis procedure, from the discretisation of target and degrader (Section 4.1) over the calibration of detector angles (Section 4.2) up to the normalisation of data taken at different distances. The latter is an exercise appearing in any RDDS analysis, details of the present solution are discussed in Section 4.3. A topic worth of serious consideration is addressed in Section 4.4, the ratio between excitations on the target and on

the degrader. Finally, Section 4.6 summarises the final procedures that led to the final lifetimes of the 2_1^+ states for the individual nuclei.

Chapter 5 places the new results in their nuclear neighbourhood. A discussion of possible trends in terms of shell structure is given in Section 5.1. Phenomenologically, the data may be described with a modification of the Valence Proton Symmetry (cf. 5.2.1). A comparison to recent shell model results from Lenzi et al. is made in Section 5.2.2.

Chapter 2

Experimental Setup

The experiments discussed in this work were performed during a six-week period in January, February and March 2009 at the National Superconducting Cyclotron Laboratory (NSCL) in East-Lansing, Michigan, USA. Lifetimes of the first 2^+ states in $^{62,64,66}\text{Fe}$ were measured using Coulomb excitation in inverse kinematics at intermediate beam energies [50].

Central to these experiments is the measurement of Doppler shifted γ -rays emitted from decaying excited states in exotic nuclei. A detailed analysis of these γ -rays will yield the lifetime of the state under investigation (cf. Chapter 4). Beams of the nuclei of interest are produced by fragmenting high energy stable ion beams on a primary target (production target). The result is a so called cocktail beam containing a wide range of nuclear species. Subsequent purification in a fragment separator supplies beams of the desired fragments (cf. Section 2.1). These are steered towards the secondary target (reaction target) mounted inside a γ -ray spectrometer optimised for the spectroscopy at large Doppler shifts (cf. Section 2.2). Lifetime measurements use a more complicated secondary target, a so called plunger device, introduced in Section 2.3. Recoils from the secondary reaction are identified in a subsequent spectrometer. Their trajectory may also be traced back to identify interaction point and angle on the secondary target (cf. Section 2.5).

2.1 Beam Preparation

In all three cases the coupled cyclotron facility [36] provided primary beams of ^{76}Ge at 130 AMeV. Fragmentation occurred on ^9Be production targets at the entrance of the A1900 fragment separator [37]. Target thicknesses were optimised for production and transmission using LISE++[46, 47] finding 235, 282 and 352 mg/cm² for $^{62,64,66}\text{Fe}$, respectively. The A1900 device is illustrated in Figure 2.1. The resulting cocktail beams were purified in the A1900 yielding beams of respectively $\approx 85\%$ of ^{62}Fe at a typical rate of 3.6×10^4 pps and an incident energy of 97.8 AMeV, $\approx 65\%$ of ^{64}Fe at a typical rate of 6×10^3 pps and an incident energy of 95.0 AMeV, $\approx 25\%$ of ^{66}Fe at a typical rate of 1×10^3 pps and an incident energy of 88.3 AMeV. The main contaminant in the beams was the corresponding Co isotope with the same neutron number. A summary of the quality of the Fe beams delivered to the target position of the S800 spectrometer is given in Table 2.1.

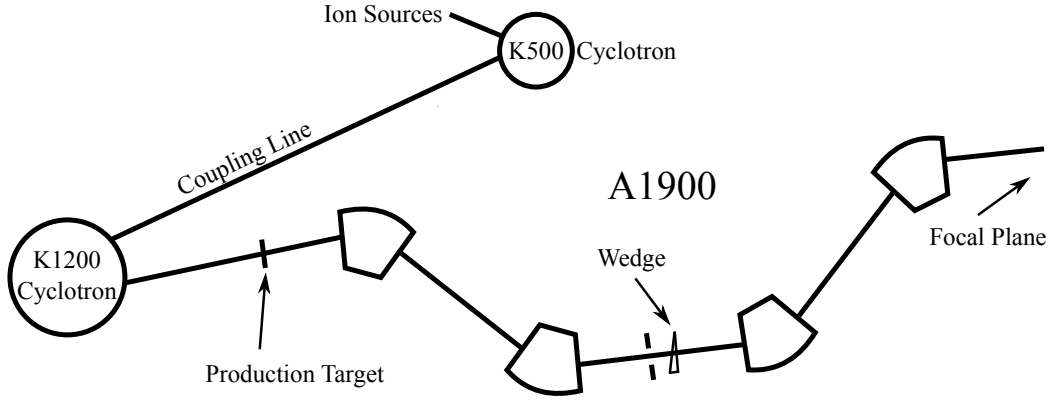


Figure 2.1: Schematic view of the A1900 fragment separator. Only dipoles are shown. The primary beam fragments on the production target, the resulting cocktail beam is separated by $B\rho$ in the first dispersive part in combination with the aperture at the centre of the device. Degradation of energy in the wedge is Z dependent, in combination with the second dispersive beamline this provides isotopic separation. (For details on particle separation cf. Section 2.5). The extended focal plane holds a plastic scintillator (126 μm) named XFP used for time of flight measurements.

A	$d_{Be}[\text{mg}/\text{cm}^2]$	purity[%]	rate $[10^3\text{Hz}]$	Energy[AMeV]
62	235	85	36	97.8
64	282	65	6	95.0
66	352	25	1	88.3

Table 2.1: Beams delivered to the secondary reaction target. d_{Be} is the thickness of the (primary) production target. The remaining fraction of the beam is dominated by the cobalt isotope with the corresponding $A + 1$.

2.2 The Segmented Germanium Array

The Segmented Germanium Array (SeGA) is a spectrometer dedicated to the γ -ray spectroscopy of fast secondary beams from fragmentation reactions. The array was conceived such that the high segmentation would allow for a Doppler correction of sufficient detail to provide for satisfyingly resolved γ -ray spectroscopy at beam velocities as high as $40\% c$ [39].

SeGA is built out of up to 18 high-purity germanium detectors. Each detector crystal is cylindrical in shape and 32-fold segmented. The circular base is divided into four equal sectors and the cylinder is divided lengthwise into eight equal intervals (cf. Figure 2.2). The segmentation’s purpose is the accurate determination of the first photon interaction to allow for a correct Doppler reconstruction. Unique characteristic of SeGA is the alignment of the detectors with respect to the source. While segmented capsules are typically aligned towards the source, SeGA capsules are aligned perpendicular to the source and parallel to the azimuthal spherical angle. A sketch of segmentation and alignment is given in Figure 2.2. The longitudinal segmentation provides sensitivity to the azimuthal angle and is the basis for the Doppler correction discussed in Section 3.2. The experiment at hand used SeGA in combination with the new Digital Data Acquisition System [44].

SeGA was used in the “plunger” configuration with angles optimised for a maximum Doppler shift (cf. Figure 2.3). This assembly has only room for 15 detectors, arranged in two rings, 7 at 30° , 30 cm from the centre of the degrader, 8 at 140° , 23 cm from the centre of the degrader¹. The forward ring (30°) is

¹As the degrader is static in this configuration, this is the reference.

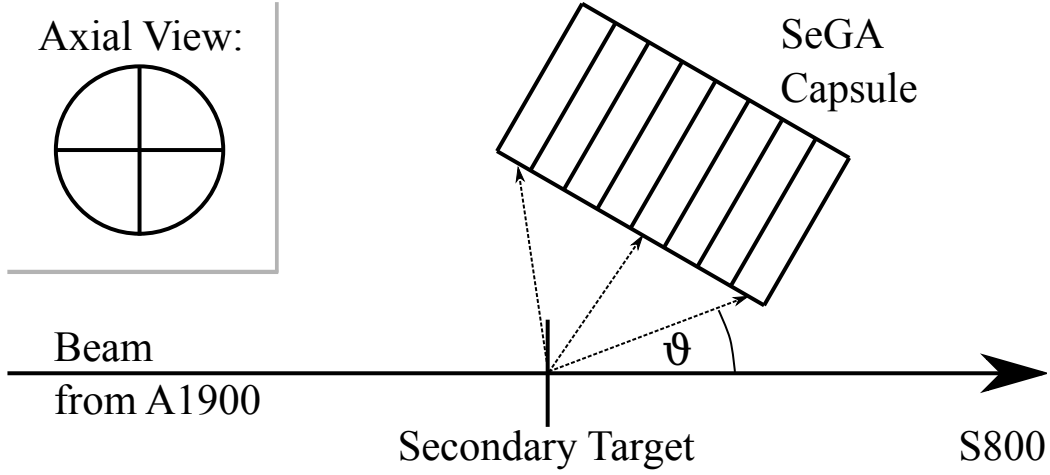


Figure 2.2: Schematic view of a segmented SeGA detector capsule mounted under thirty degrees with respect to the beam. Different γ -ray emission angles ϑ are shown to illustrate the azimuthal resolution of the detector.

constrained by the gate valve of the S800 spectrometer and holds one detector less than the backward ring (140°).

2.3 The Recoil Distance Doppler Shift Method and the Köln Plunger for Intermediate Energies

The recoil distance Doppler shift method (RDDS) [2] is a well established technique for the measurement of nuclear level lifetimes in the picosecond range. A typical setup consists of a reaction target and a stopper. Target and stopper are flat, parallel foils or plates and mounted at a variable distance with respect to each other.

The concept of the experiment is as follows. In this work, projectile Coulomb excitation is used to excite the 2_1^+ states in the nucleus of interest. Depending on where the excited state decays—whether it decays at a point in the target, between target and degrader, in the degrader or after the degrader—the nucleus will be at a characteristic velocity and a characteristic angle to the detector. Thus, the Doppler-shift of the emitted γ -ray is related to the position of the nucleus at the time of its decay. As the velocity is well known, this position is uniquely related to

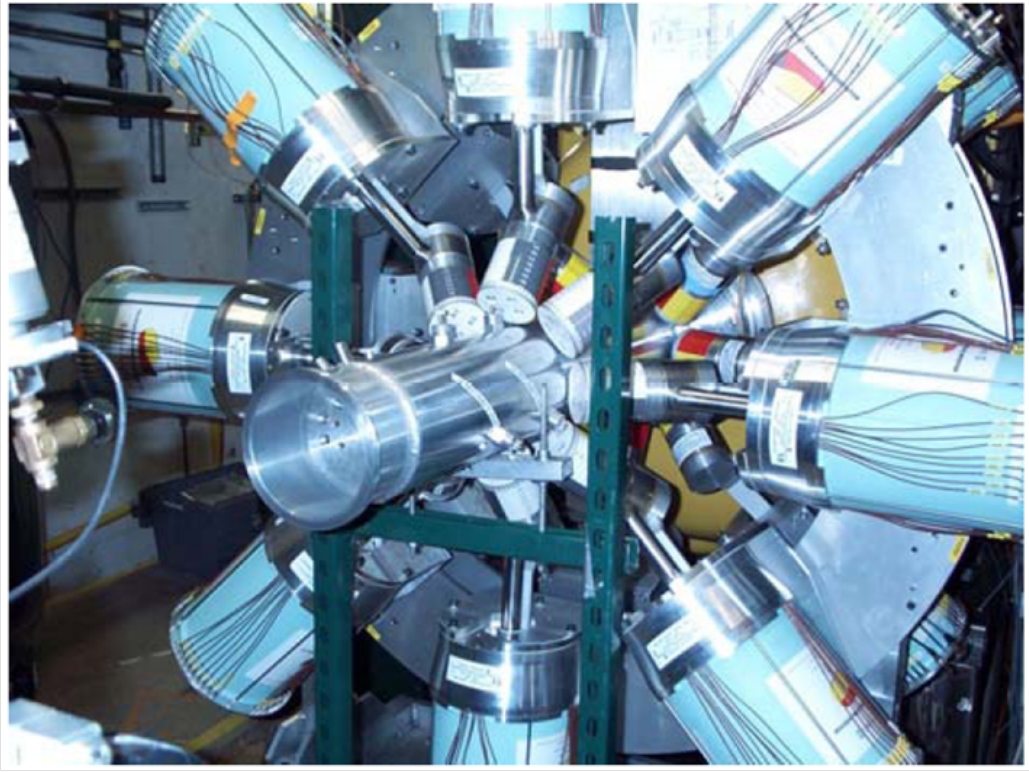


Figure 2.3: The Segmented Germanium Array in the plunger configuration mounted at the target position of the S800 spectrometer. Picture courtesy of Dirk Weisshaar, NSCL.

the flight-time of the recoiling nucleus and the lifetimes of excited states may be derived. Typical target degrader separations are rather long compared to the thickness of the targets. Here, targets from $300\text{ }\mu\text{m}$ to $400\text{ }\mu\text{m}$ were used, distances were mostly longer than $2000\text{ }\mu\text{m}$. The lineshape of the decay in γ -ray spectra shows two characteristic peaks, one originating mostly from decays between target and degrader² and the other one originating from decays in and after the degrader. The principle is illustrated in Figure 2.4. This method was first adopted to radioactive ion beams at intermediate energies by Chester et al. [14].

A dedicated plunger device was designed by A. Dewald for RDDS measurements at intermediate beam energies [43, 17]. Mounted at the target position of the S800 spectrometer (cf. Section 2.5), the plunger device itself is shoved into an

²Some decays might already take place whilst in the target

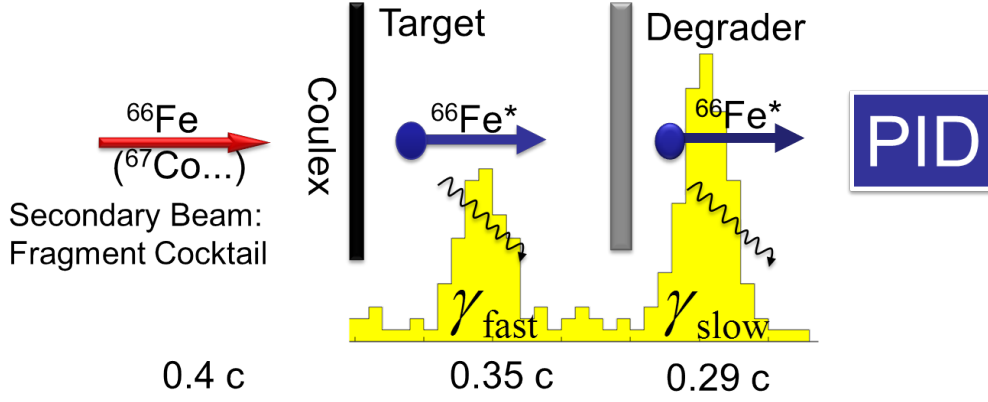


Figure 2.4: The Recoil Distance Doppler Shift Method (backward angles). The cocktail nature of the beam necessitates a particle identification (PID).

adopted S800 beam pipe where it is aligned using a sextuplet of screws. Distances can be set by means of a motor with an accuracy of a few fractions of a micron³ which compares to typical distances of a few millimetres. Distance information is either read from an inductive probe or directly from the motor device, measured optically in that case. A capacitive feedback control system [3]—suitable for very short distances—is implemented but has not been used in the experiment as only rather long distances have been considered.

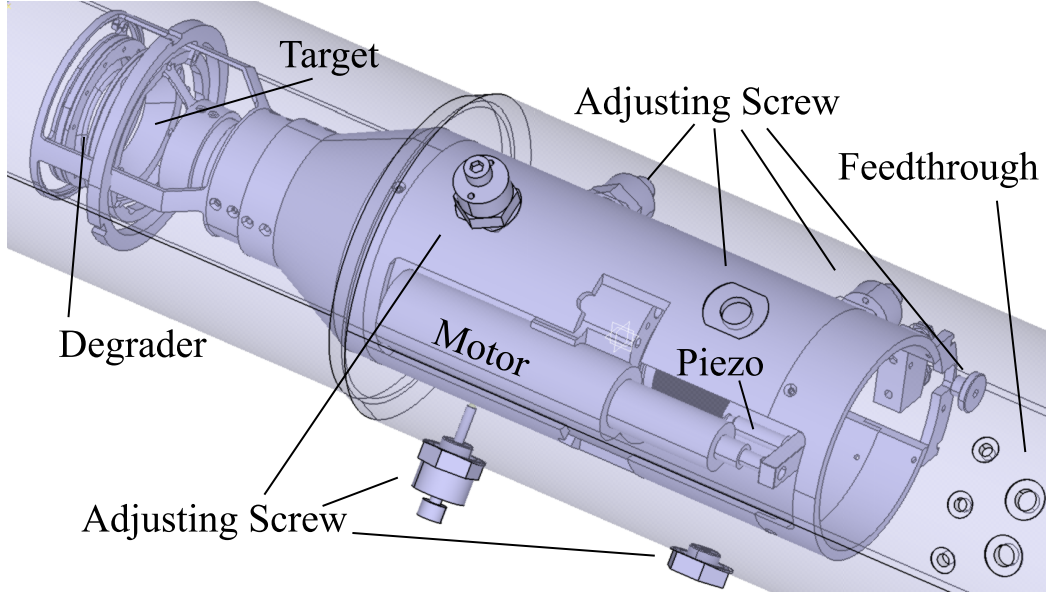
2.4 Relativistic Coulomb Excitation and the Choice of Target and Degradation Combinations

Coulomb excitation at relativistic beam energies was discussed in great detail by Winther and Alder [50] and has found frequent use in the past to study $B(E2; 0_1^+ \rightarrow 2_1^+)$ excitation strengths⁴ in a wide range of nuclei. For a review, please be referred to [25] and [23]. The analysis of these experiments is not model

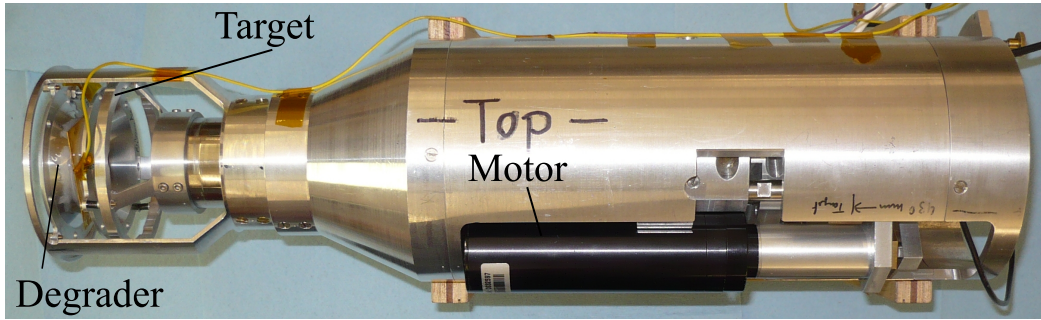
³In practice the limit on this is set by the flatness of the foils itself. As those are typically rather thick for this kind of experiment—rather sheets than foils—they cannot be stretched. This limits the determination of “absolute” distances to several tenth of microns in many cases.

⁴The reduced transition probability $B(E2)$ is directly related to the lifetime τ via the level energy E in MeV through:

$$1/\tau = 1.22 \cdot 10^9 \cdot E^5 \cdot B(E2)$$



(a) Schematic



(b) Photography

Figure 2.5: The Köln Plunger for Intermediate Beam Energies.

independent and may suffer from systematic errors in the assumptions being made. A detailed study on the resilience of the prevalent method is given by Gade et al. [21]. An important difference between conventional Coulomb excitation and relativistic Coulomb excitation is that the latter is a fast process. The average interaction time between a given projectile nucleus and a given target nucleus is so short that multiple excitation can be excluded. Relativistic Coulomb excitation is a pure one step process. Therefore, only the lowest lying nuclear level will be excited leading to a direct feeding of the 2_1^+ level.

The RDDS method measures level lifetimes directly in a model independent

way. Combining Coulomb excitation at relativistic energies with the RDDS method [14, 17] has the advantage of direct population over other excitation methods (e.g. knock-out reactions). Apart from that, cross sections are usually rather large (a few hundred mb).

We will outline now general considerations on the choice of targets and degraders followed by an example based on the proposal for the experiments discussed in this work.

In an idealisation of the present experiment, RDDS using Coulomb excitation, targets and degraders are infinitesimally thin. Any process occurring in the foil will occur instantaneously. A very thin target allows for a lot of very convenient assumptions. All nuclei get excited in the middle of the target. All nuclei get excited at the same speed. Virtually no nuclei start decaying in the target. Slowing down is an instantaneous, discontinuous process. Especially no velocity profile will be observed. The same arguments apply to the processes in the degrader. Foremost, the degradation of velocity is instantaneous in a very thin degrader. Again, *no* velocity profile is observed. Furthermore, excitations take place in the middle of a thin degrader. No excited states—whether they were excited in target or degrader—decay in a very thin degrader.

An infinitely thin target and degrader would simplify the observed spectra. The velocity profile resulting from a gradual stopping procedure and the resulting Doppler-broadening of the observed γ -ray spectra (cf. Section 3.2) would disappear. The present reaction mechanism, however, Coulomb excitation, is dominated by Rutherford scattering. Even though a thin target localises this process, the scattering nature of the process prevails. Within the acceptance of the S800 spectrograph (cf. Section 2.5) particles may be scattered up to 5° from the beam axis. This will smear out the observed photopeak (given by Equation 3.2, $E_{Lab} = \frac{E_0 \sqrt{1-v/c^2}}{1-v/c \cos(\theta)}$, cf. Section 3.2). Thus, for an infinitely thin target, the lower limit to the peak width is the Doppler corrected Rutherford cross section folded with the spectrograph acceptance.

The target material should have a high Z to provide a high Coulomb excitation cross section which scales with Z^2 . It is in the nature of the experiment that the projectile will be slowed down in the target. In an idealised experiment, this would proceed instantaneously. To make this stopping process as fast as possible, the target should have a high density. Gold is a typical choice. It is more easy to machine than lead or bismuth, which would offer a higher Z but a lower density. The thickness of the target has to be chosen carefully. A thicker target will provide a higher yield of the desired reaction product. A thin target is even more important if very short lifetimes are to be measured. The goal of an RDDS experiment is the observation of a fast and a slow component. Therefore, it is necessary that the excited nuclei can leave the target.

For the degrader another compromise has to be found. The degrader's main purpose is to degrade the velocity of the recoils from the target, as explained in Section 2.3. States that decay after the degrader shall do so at a considerably lower velocity. The emitted photons have to be observed at a distinctly Doppler shifted energy to provide well separated fast (between target and degrader) and slow (after the degrader) peaks in the recorded γ -ray spectra. The stopping power of the material scales with the electron density, that is $n = \frac{N_A \cdot Z \rho}{A \cdot M_u}$, where ρ is the density, $M_u = 1 \text{ g/mol}$ and N_A is Avogadro's constant. Ideally, the stopping should be instantaneous as discussed above. However, this is not sufficient to find an optimal $\frac{Z\rho}{A}$ ratio. In addition, the Coulomb excitation cross section on the degrader itself has to be taken into consideration. We have strong interest to keep this as low as possible in order to keep the lifetime information from γ -rays emitted after the degrader meaningful (cf. Section 4.4).

The production rate of $^{62,64,66}\text{Fe}$ was estimated in the proposal for experiment 06022⁵ based on calculations with LISE++[46, 47]. Assuming a transmission of 50% from the A1900 fragment separator to the target position of the S800 spectrometer (cf. Section 2.5), a rate of 5700, 3450 and 650 particles per second was expected to hit the secondary reaction target⁶, respectively for $^{62,64,66}\text{Fe}$. As noted

⁵The NSCL running number for the experiment at hand

⁶When the proposal was written, this rate seemed to be limited by the cathode readout drift chambers in the S800 spectrometer (cf. Section 2.5). During the experiment it turned out that they were not necessary for the particle identification.

above, gold is the favourable material for Coulomb excitation targets. It is easy to machine, very dense and has a high Z . An optimal thickness is estimated by calculating the reaction rate. The Coulomb excitation cross sections on gold were expected to be 300, 300 and 250 mb, again respectively for the three isotopes in ascending order. The interaction probability, w , is related to the cross section σ via $w = \sigma \frac{D_T \rho_T}{A_T u}$, where D_T is the thickness of the target, ρ_T represents the corresponding density, A_T is the mass number and u is the atomic mass unit. The interaction probability times the incoming beam rate is the quantity labelled Rate_T in Table 2.2. This is the actual γ -ray production rate. Significant for the choice of the target is the fraction $\frac{\text{Rate}_T}{D_T}$, the rate normalised on the target thickness. The estimates from the proposal yielded 10.5, 6.33 and $1.76 \text{ Hz} \cdot 10^5 / \mu\text{m}$. Combining these values with an expected transmission of 86% for the S800 spectrometer (cf. Section 2.5) and a photopeak efficiency, ϵ_{Ge} of about 1% for the 30° ring of SeGA, a rate estimate, $\frac{\text{Rate}_T}{D_T} \Theta_{S800} \epsilon_{Ge}$, is available. Based on these numbers and an idea of the amount of beam time that might be allocated to the project (less than six days) it is now possible to approach the choice of target thickness.

The rate estimate for ^{66}Fe was extremely low as a result of poor production rate. It was therefore proposed to measure the absolute Coulomb excitation cross section to the 2_1^+ state to deduce the $B(E2; 0^+ \rightarrow 2^+)$ value for this nucleus using a $500 \mu\text{m}$ Au target and no degrader. This would also have significantly reduced the measurement time for this nucleus as only one “distance” would have had to be measured. As discussed in the last part of this section these plans were changed during the experiment. The rate estimates for $^{62,64}\text{Fe}$ were more promising, a plunger experiment seemed possible. In the proposal a $300 \mu\text{m}$ Au target was found suitable for ^{64}Fe . For the case of ^{62}Fe a shorter lifetime was expected, to reduce the number of decays in the target $200 \mu\text{m}$ of gold were chosen. This leads to expected rates of 2.1, 1.9 and 0.88γ -rays per second for $^{62,64,66}\text{Fe}$, respectively.

The original proposal proposed iridium degraders for $^{62,64}\text{Fe}$. Iridium as a degrader for Coulomb excitation experiments has the advantage of a very high density (higher than gold) and the disadvantage of a high Z , thus a high excitation cross section itself. Furthermore, iridium is brittle and therefore difficult to machine. This compromise was made to allow for a fast stopping process in

the degrader so that a thinner degrader could be chosen. The necessary thickness can be derived from the resolution of SeGA which was expected to be about 2% for decays after the target. To allow for an appropriate peak separation, the Doppler-shifted γ -ray energy, $E' = \frac{E_0 \sqrt{1-(v/c)^2}}{1-(v/c) \cos(\theta)}$ (cf. Section 3.2), should differ by 6% = 1.5 (2% + 2%) for decays before and after the degrader. Using LISE++, this lead to the conclusion that it is possible to use the same 200 μm iridium degrader for both cases. A full summary of all the parameters is given in Table 2.2.

Unfortunately, no ready-made iridium foils of 200 μm thickness were on the market in the fall of 2008 and custom-made foils were too expensive. After stopping power calculations revealed the velocity loss in 250 μm Ir (available as ready-made foils) to be too large ($v/c_D = 0.299$ instead of 0.320), plans were changed. It was decided to go for an easily available and machinable foil. Based on positive experience in the past, the choice was on Nb and Mo. They come with the advantage of a significantly lower Coulomb excitation cross section due to the lower Z and the disadvantage of a density of $\rho \approx 10 \frac{\text{mg}}{\text{cm}^3}$, roughly half of the Ir value. This lead to choosing a degrader of 400 μm of the isotopically pure niobium, the velocities for $^{62,64}\text{Fe}$ agree within 2% with the values calculated for the iridium degrader (cf. Table 2.3).

The group participated in the experiment published in [33], in which lifetimes of the 2_1^+ states in $^{62,64}\text{Fe}$ were measured at GANIL. When the experiment at hand was performed no preliminary results from [33] were available. This made ^{66}Fe the primary goal of the campaign. Table 2.3 gives a 400 μm degrader for this case. The new schedule previewed to reduce the time allocated to ^{62}Fe , which was treated in sufficient quality by the French group leading later to [33], in favour of a very robust and sound RDDS measurement of ^{66}Fe . Beamtime allocated for ^{64}Fe was not to be changed. As the quality of the French data is lower and there was a definite interest in confirmation and improvement. Apart from that, going for ^{66}Fe was still a risky endeavour.

A	Rate_m [10^3 Hz]	v/c	σ_T [mb]	$\frac{\text{Rate}_T}{D_T}$ [$\text{Hz} \cdot 10^{-5} / \mu\text{m}$]	$\frac{\text{Rate}_T}{D_T} \Theta_{\text{S800}} \epsilon_{\text{Ge}}$ [$\text{Hz} \cdot 10^{-7} / \mu\text{m}$]	Au [μm]	v/c_T	Ir [μm]	v/c_D	Rate_T [Hz]	S800_γ [Hz]	Ge_T [Hz]
62	5.7	0.419	300	10.5	9.03	200	0.381	200	0.320	2.1	1.8	0.018
64	3.45	0.415	300	6.33	5.44	300	0.359	200	0.284	1.9	1.6	0.016
66	0.65	0.416	250	1.76	1.51	500	0.306	-	-	.88	.75	0.0075

Table 2.2: Experimental Parameters as estimated and proposed in the proposal [16]. Rate_m is the number of particles transported from the A1900 to the target position of the S800 spectrograph assuming a transmission of 50%. Gold was proposed as target material for all three species, iridium was previewed for $^{62,64}\text{Fe}$ while for ^{66}Fe a pure Coulomb excitation run without degrader was planned. Rate_T is based on the estimated cross sections on the target, σ_T , S800 $_\gamma$ gives the number of these that are identified by the S800 spectrometer assuming a transmission of 86%. Ge_T gives the expected rate in the forward ring of SeGA (cf. Section 2.2) assuming a photopeak efficiency of 1%. All values are taken from [16] except for ^{64}Fe S800 $_\gamma$, which suffered from a typo and Rate_T/D_T which is derived from the other values.

A	Au-Target [μm]	v/c_T	Nb-Degrader [μm]	v/c_{Ir}	v/c_{Nb}
62	200	0.381	400	0.320	0.325
64	300	0.359	400	0.284	0.290
66	300	0.362	400	-	0.299

Table 2.3: Degrader alternatives. The velocities after the degrader agree within 2%. In terms of stopping power, 400 μm of niobium are equivalent to 200 μm of iridium.

The measured experimental parameters are shown in Table 2.4. The velocities given stem from the $B\rho$ settings of the spectrometer⁷. The uncertainty for the given velocities is about 1% in root mean square. The rates differ from the values in the proposal. This is mainly due to improvements made in the meantime to the sources and the transmission of the system. As the system was tuned for rates, the v/c values are different from the proposal as well, so a revision of degrader settings was performed just before the experiment. ^{64}Fe was measured first, the peak separation was found to be more than sufficient and therefore 300 μm of niobium were chosen for ^{66}Fe following the philosophy that a foil should always be as thin as possible. The degrader was not removed again till the end of the campaign. No further optimisation was made for ^{62}Fe due to time limitations.

A	Rate _{in} [10^3Hz]	v/c	Au [μm]	v/c_T	Nb [μm]	v/c_D
62	36	0.426(4)	300	0.368(4)	300	0.322(3)
64	6	0.420(4)	300	0.364(4)	400	0.298(3)
66	1	0.407(4)	300	0.346(3)	300	0.291(3)

Table 2.4: Targets and degraders used in this work and the resulting v/c values with errors in root mean square. v/c values are discussed in Section 4.1.

⁷Except for the v/c value after degrader for ^{62}Fe as discussed in 4.1.

2.5 Particle Identification and the S800 Spectrograph

Particle Identification

The reaction will take place at the target position of the S800 spectrograph. The mechanism is uniquely defined by the incoming and outgoing particles. The cocktail nature of the incoming beam makes an analysis of its composition indispensable. Incoming and outgoing particles have to be identified. The straightforward approach to particle identification is particle separation. By applying a magnetic field B to charged particles of a given kinetic energy, the bending radius ρ defines their charge to mass ratio. This can be shown by equating Lorentz and centripetal force:

$$\begin{aligned} qvB &= \frac{mv^2}{\rho} \\ &\Leftrightarrow \\ \frac{m}{q} &= \frac{B\rho}{v} \end{aligned} \tag{2.1}$$

A magnetic separation with an appropriate trigger condition behind the spectrometer can thus grant an identification of the quotient of $\frac{A}{q}$, where q is the overall charge of the ion of interest. The velocity of the incoming particles is measured as their time of flight through the spectrometer as the spectrometer length is fixed⁸. In order to fully identify the nucleus—that is gain access to Z or A directly—a strong dependence on one of the two has to be introduced into the system. One approach could be electrostatic deflection. Here, the quadratic dependency of the stopping power on the projectile's Z is used ($\frac{dE}{dx} \propto -\frac{Z^2}{E}$, [8]).

A typical setup consists of a $\Delta E - E$ telescope, i.e. a stack of calorimetric detectors of increasing thickness. The first measures a fractional energy deposition, the last is thick enough to stop the particle and measures the remnant of the energy. Two detectors are enough, the setup gets closer to a $dE - E$ telescope if more

⁸This will in fact allow for a bundle of trajectories as discussed in Chapter 3

detectors are used. Z is accessible now by comparing the coincident information of the detectors with each other. A two dimensional plot of ΔE over E will have a significant structure. Combining this with the $\frac{A}{q}$ information allows for an identification of the particles of interest. The exact procedure used in the experiments at hand is discussed in Chapter 3.

Furthermore, the spectrograph might be equipped with position and momentum sensitive detectors. The latter is realised by combining two pairs of the first kind (giving the trajectory) with the energy information from the $\Delta E - E$ telescope. In combination with an inverse map of the ion optics in use, the particle's trajectory can be tracked back to the point of interaction to deduce the scattering angle. This is not necessary for the identification itself but may increase the resolution of secondary detectors. In the case of ^{66}Fe this was used to improve the Doppler corrections of the detected γ -rays. Tracking is absolutely necessary when measuring absolute Coulomb excitation cross sections, as these depend on the scattering angle.

The S800

The experimental tool performing the particle identification is the S800 spectrograph [6, 51], sketched in Figure 2.6. The device has two major parts, the analysis line and the spectrograph itself. The former is used to tune the beam on target and to implement various optical modes. It takes also part in the tracking. Apart from focusing quadrupoles, the main component of the spectrograph is a three storeys high superconducting dipole magnet arrangement. The apparatus' focal plane consists of two position sensitive Cathode Readout Drift Chambers (CRDCs) measuring the direction of a particle's trajectory, a segmented ionisation chamber measuring energy loss and a series of scintillators working calorimetrically. Combining the reading of all devices, particle momenta can be calculated on an event-by-event basis. This allows also for the reconstruction of each particle's trajectory back to the position of the secondary reaction target using the optical map of the spectrograph. This procedure, called tracking, can improve the Doppler correction of measured γ -ray spectra.

Analysis Line

The major purpose of the analysis line is beam tuning and implementation of optical modes. The analysis line is symmetric around the intermediate image and allows for a maximum magnetic rigidity of about 5 Tm which corresponds to 800 MeV protons, naming the spectrograph. The experiments discussed in this work were run in the *focused* mode meaning that the beam was focused on the target. The analysis line is achromatic⁹. This mode offers the highest momentum acceptance of the spectrograph, $\pm 2\%$. The spectrograph itself will run in chromatic mode meaning that the intrinsic momentum spread of the beam folded with the momentum change induced by the reaction in target and degrader will be mapped on the focal plane. The image on the focal plane is therefore not focused which is why this mode allows for the highest count rates.

The particle identification procedure discussed in Chapter 3 requires a scintillator at the object position of the spectrograph for time of flight measurements. Here, a plastic scintillator (1 mm) was used. It can withstand rates up to 1MHz. It is also possible to place more sophisticated detectors in the object box to analyse the beam composition for short periods, usually they cannot support the full desired rate. The double bend structure following the object box (cf. Figure 2.6) makes it highly probable that eventual contaminants produced in reactions on the object scintillator will be filtered out before reaching the focal plane of the spectrograph. Furthermore, a large variety of tracking detectors are available to be placed at intermediate image and target position. Those were not used in the experiments at hand.

Spectrograph

The spectrograph's main building blocks are two superconducting dipole magnets and the focal plane box. The maximum magnetic rigidity reached is about 4 Tm. A main concept of the construction is to use as little trim magnets as necessary. Instead, the magnetic fields are measured, the aberrations are calculated and analytically corrected on an event-wise basis in the analysis code based on [7]. The

⁹Achromatic lenses focus light of different wavelength in the same plane.

whole device can rotate up to 90° . This feature has not been used in this work. The de facto resolution is 1 part in 2000 in energy and 10 mrad in scattering angle. The nominal resolutions are higher but can only be reached under very restrictive conditions. The spectrograph offers a huge acceptance of 20 mSr with an ellipsoidal shape ($\pm 3.5^\circ$ in the dispersive plane, $\pm 5^\circ$ in the non-dispersive plane).

Focal Plane Box The focal plane box of the spectrograph is illustrated in the inset in Figure 2.6. Its purposes are the identification of incoming particles and the reconstruction of their trajectories which is optional in the case at hand. As mentioned above, it holds two position sensitive cathode readout drift chambers (CRDC), an ionisation chamber and a series of stacked scintillators. The timing resolution is about 100 ps.

Cathode Readout Drift Chambers The purpose of the Cathode Readout Drift Chambers (CRDCs) is to provide the particle's trajectory. They are placed 1 m apart, by simple trigonometric operations two positions yield a vector. Extending ± 28 cm in the dispersive and ± 13 cm in the non-dispersive direction at a depth of 1.5 cm they reach a nominal resolution of 0.5 mm that is not reached in *focused* mode. Technically we are facing single wire drift detectors filled with 80% CF_4 and 20% C_4H_{10} ¹⁰ at 6.6 kPa. The position along the wire is obtained by induced cathode readout. As the drift velocity of electrons in gas is slow, these detectors cannot be run at high count rates. The CRDCs cannot be used without at least one scintillator signal as a timing reference for the drift time. For reasons under investigation efficiency losses appear above 5000 Hz.

Ionisation Chamber The ionisation chamber is a ΔE measurement device used in the particle identification procedure described in detail in Chapter 3. The chamber is a standard Frisch-gridded [20] model filled with $\text{P}10$ ¹¹ at 18.7 kPa. At this pressure particles up to $Z = 30$ can be separated, higher pressure and a thicker window are necessary for larger Z . The chamber is segmented into 16 anodes of 1 inch length. The electronic noise grows with the detector capacitance,

¹⁰Isobutane

¹¹90% argon and 10% methane

segmenting the anode reduces the capacitance and therefore the noise. As the segments are independent, their noise adds quadratically.

Scintillators Final part of the focal plane box is a stack of four large plastic scintillators of 3 mm, 5 cm, 10 cm and 20 cm thickness labelled E1, E2, E3 and E4 in the same order. Their purpose is timing and energy loss, respectively total energy measurement of incoming particles. Each is read out by two photodiodes. The E1 scintillator was used as trigger signal in the experiments discussed in this work. This scintillator doubles as downstream window of the ionisation chamber. E2 measured the total energy loss.

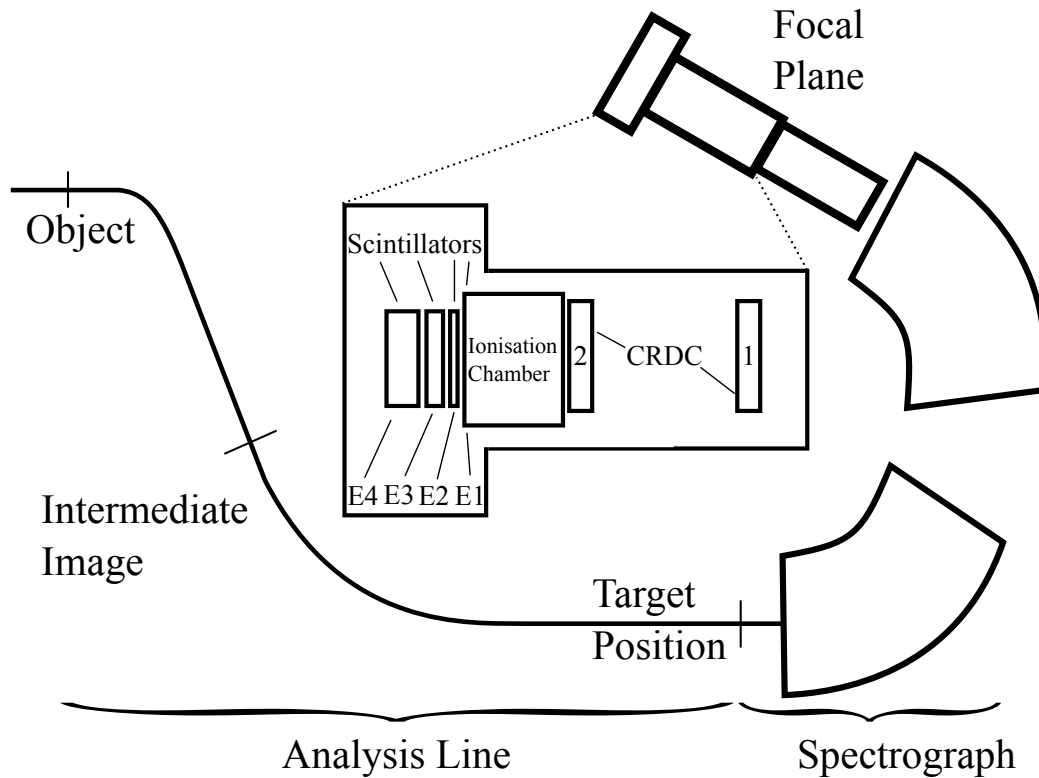


Figure 2.6: Sketch of the S800 Spectrograph, only dipoles are shown.

Chapter 3

Data Preparation

The experiments discussed in this work comprise about 750 GB of raw data, that reduce quite quickly to 50 GB when merged to proper events. Nonetheless, it is obvious that some preprocessing is necessary before the actual lifetime analysis can be tackled. This chapter interweaves sorting, separation and calibration in the natural way prescribed by the analysis procedure. The particle identification procedure will be discussed first, including the necessary calibrations applied to the different focal plane components of the S800 spectrograph (cf. Section 2.5). The second part of this chapter deals with the preparation of γ -ray spectra and the calibration of the SeGA spectrometer (cf. Section 2.2).

3.1 Particle Identification

The cocktail nature of the beam delivered to the S800 spectrograph makes a detailed analysis of the beam's composition necessary. Particle identification (PID) of incoming particles and outgoing particles, i.e. particles entering and particles leaving the plunger device, determines the reaction mechanism uniquely. In the case at hand, the PID is simplified as desired incoming and outgoing particles are identical and abundant in the beam.

The identification procedure is divided into two main stages, the identification of the incoming beam and the identification of the outgoing particles after the reaction. After each step the data stream is separated using the acquired gate. This

makes subsequent sorting runs significantly faster and keeps the sorting codes neater.

As discussed in Section 2.5, a separation on $\frac{A}{q}$ can be obtained by applying a magnetic field to travelling charged particles according to $\frac{A}{q} = \frac{B\rho}{v}$ (Equation 2.1). Isobaric resolution is obtained by calorimetric means, also discussed in Section 2.5, that will provide sensitivity to Z via the quadratic dependence of the stopping power on the nuclear charge ($\frac{dE}{dx} \propto -\frac{Z^2}{E}$).

The scintillators at the object position of the S800 spectrograph and in the focal plane box (cf. Section 2.5) measure the time of flight through the whole device. Knowing the length of the apparatus, this makes the magnetic rigidity $B\rho$ a direct selector for $\frac{A}{q}$. As the length of the spectrograph is fixed, particles of different mass to charge ratios will have a different velocity and therefore a different time of flight for a given magnetic rigidity. Apart from this time of flight, the passage time from the A1900 extended focal plane to the S800 object scintillator was measured, also on an event-wise basis. Isobaric resolution is based on the energy deposition in the ionisation chamber. By correlating any and all of these event-wise measurements, a unique identity could be assigned to every particle involved in the experiments at hand. Due to the simple reaction used for all three nuclei, the particle identification could mainly be done on a time of flight basis for $^{62,64,66}\text{Fe}$.

A detailed account of the identification of incoming and outgoing beams is given in the respective sections 3.1.2 and 3.1.3.

3.1.1 S800-Calibrations

Apart from four stacked scintillators that were used for timing in the present experiment, the focal plane box of the S800 spectrograph houses two Cathode Read-out Drift Chambers (CRDCs) and an ionisation chamber (cf. Section 2.5). The CRDCs are placed 1 m apart and are position sensitive. As a doublet they yield the trajectory of incoming particles. The ionisation chamber is a ΔE detector that plays an important role in the particle identification procedure discussed in Section 3.1.3. CRDCs and ionisation chamber need to be calibrated.

CRDC The x-y CRDCs (cf. Section 2.5) in the focal plane are hard wired in one dimension (in the dispersive plane, labelled X), the position information on the other axis is calculated from the drift time of the charge carriers through the gas and needs to be calibrated. As the gas pressure changes (very slowly) during the experiment, this was repeated for all three nuclei individually, twice for ^{66}Fe . In the case of ^{66}Fe the PID was found to be independent of the calibration used. The calibration is performed by moving a metal plate with a well defined hole and slit pattern (mask) into the fanned out beam directly in front of the CRDC in question¹. The well defined image of a mask is shown in Figure 3.1. Assigning metric values to electronic channels to first order is sufficient.

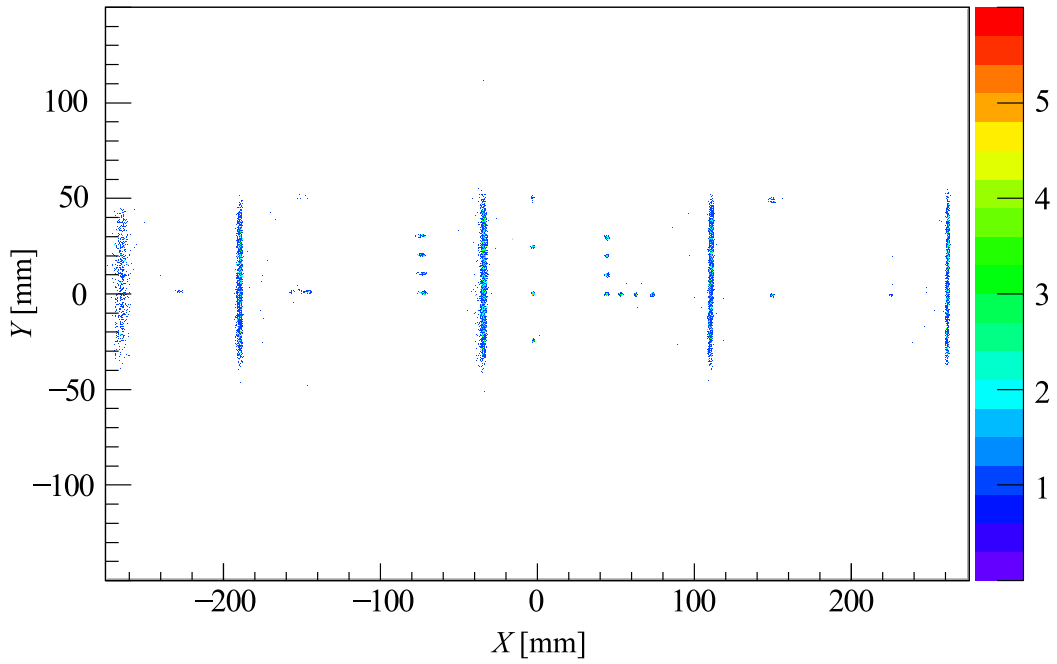


Figure 3.1: CRDC-Calibration X is the dispersive plane and hard-wired. The colour scale gives the number of counts.

¹There are two identical masks, one for each CRDC.

Ionisation Chamber The ionisation chamber (cf. Section 2.5) at the S800 focal plane is 16-fold segmented. Each segment is read out through its own electronics channel. Typically these require gain and offset matching. For all three nuclei, gains and offsets were literally matched to the channel with the smallest reading assuming a constant ionisation rate over the full volume of the chamber. In that sense, the word calibration is misleading, the ionisation chamber is gain matched.

Following the first assumption, the calibrated channel readouts are samples of the same normal energy loss distribution. Calculating centroid and standard deviation for each event, the energy loss is taken to be the average of those channels that are closer than one σ to the centroid of the normal distribution. The other channel readings are ignored.

3.1.2 PID-IN

As introduced in Sections 2.5 and 3.1, the identification of particles is based to a large part on the selectivity of the magnetic rigidity $B\rho$ over the $\frac{A}{q}$ ratio of the incoming particles, $\frac{A}{q} = \frac{B\rho}{v}$. In a first step, the data stream shall now be separated on the incoming beam (PID-IN). This selection cannot be based on the magnetic rigidity $B\rho$, as the velocity of the beam is due to change at the target position. It is not possible (at least not under reasonable conditions) to optimise the spectrograph for the undegraded and the degraded beam. Thus, any preselection of the data stream on the incoming beam has to be based on a quantity that is the same for reacted and unreacted beam. This means that it has to be measured before the beam hits the target. An easily accessible quantity that differs sufficiently for the components of the beam cocktail is their velocity when exiting the A1900 fragment separator. Measuring the time a particle takes to pass the transfer hall between the A1900 vault and the S800 vault—using the scintillators introduced in Sections 2.1 and 2.5—yields the desired velocity, as the path length is fixed. A schematic of the position of the timing devices and the times and time differences described in the following is given in Figure 3.2.

Thus, the identification of incoming particles is performed event-wise solely on a time of flight basis. The relevant times are:

1. T_{XFP} , the time from the extended focal plane scintillator (XFP, cf. Section 2.1) outside of the A1900 separator to the compulsory check-point of every particle taken into consideration, the E1 scintillator of the S800 spectrograph (cf. Section 2.5, the E1 scintillator serves as main trigger).
2. T_{OS} , the time from the object scintillator (OS, cf. Section 2.5) at the entrance to the S800 spectrograph to the E1 scintillator.
3. $T_{PID} = T_{XFP} - T_{OS}$, the quantity actually considered for the particle identification. This is the time it takes a given particle to pass through the transfer hall between the A1900 and the S800 (cf. Figure 3.2)

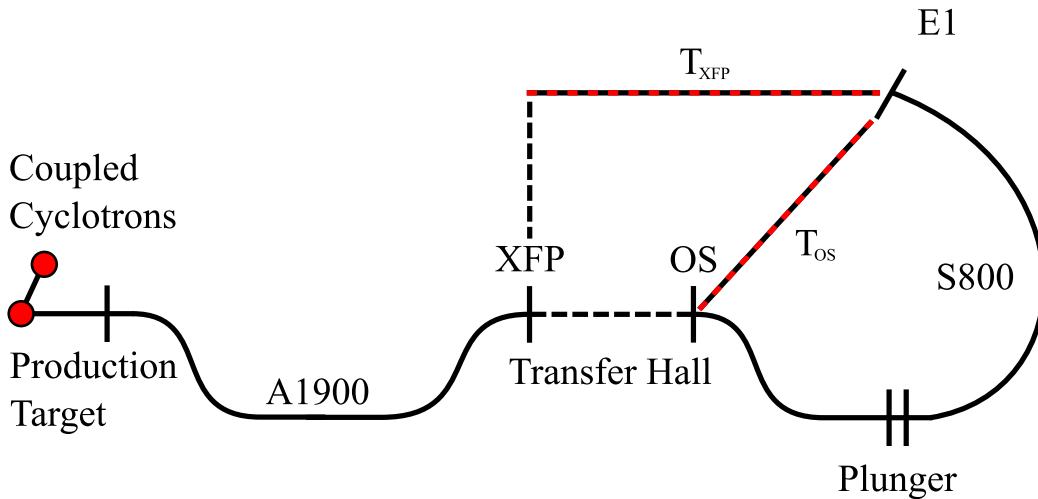


Figure 3.2: Schematic of the time-of-flight differences used

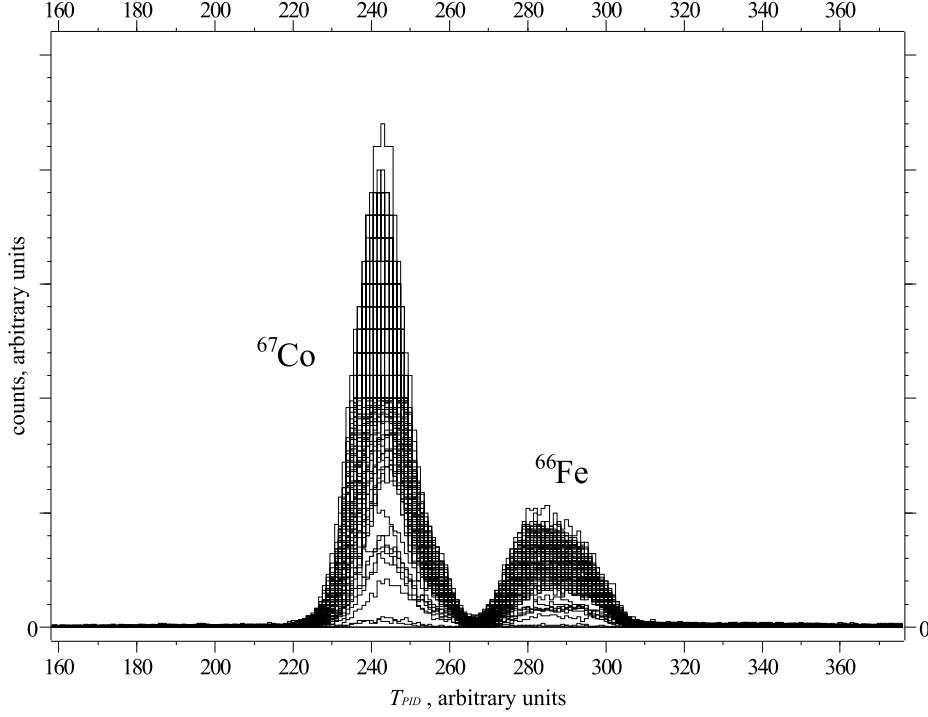


Figure 3.3: T_{PID} for all runs of ^{66}Fe . Clearly, a single gate can be used to separate ^{67}Co from ^{66}Fe . Plots of similar quality are obtained for $^{62,64}\text{Fe}$.

Histograms of T_{PID} for all runs of ^{66}Fe are overlaid in Figure 3.3. Clearly, ^{66}Fe and the main contaminant ^{67}Co can be separated by the same gate for all runs. Applying this gate to the data stream reduces the event data files² from 6.4 GB to 2.1 GB.

As an illustration Figure 3.4 shows T_{OS} plotted over T_{PID} for a run of ^{66}Fe with no target mounted. The y-axis is proportional to $\frac{A}{q}$ counting downwards, while the x-axis relates to the particle's velocity when leaving the A1900 fragment separator, increasing from right to left. The structure to the right of ^{66}Fe has not been identified as it is statistically not significant for this analysis.

²Those are the files that have to be processed every single time the data are sorted.

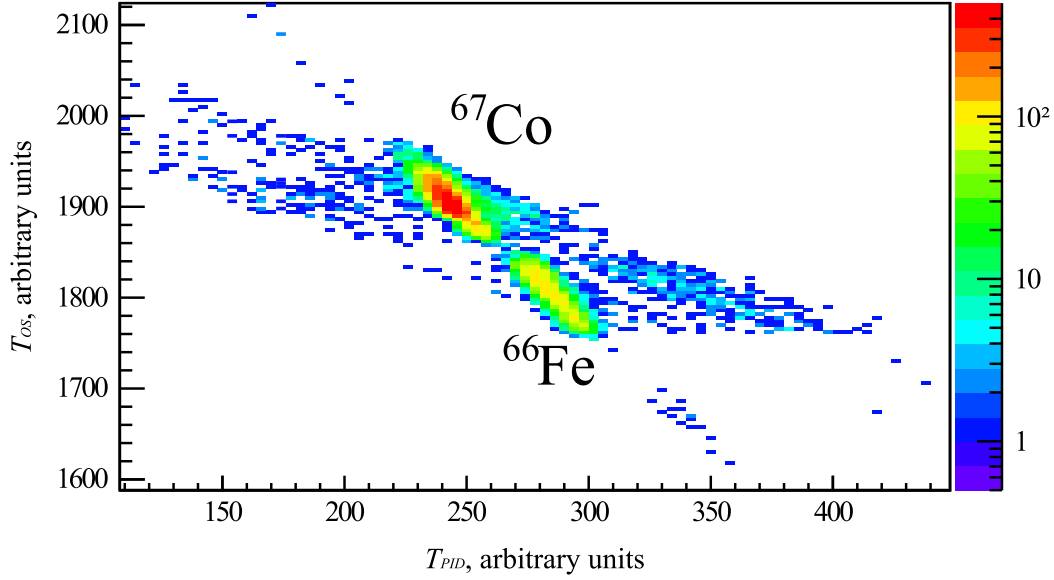


Figure 3.4: Typical PID-IN plot. Run 242, empty beam pipe, ^{66}Fe . The colour scale gives the number of counts.

3.1.3 PID-OUT

By the procedure described in Section 3.1.2, most of the disturbing cocktail components can be removed. A swift glance ahead at Figure 3.7—showing the data stream separated on incoming ^{66}Fe —will reveal that the desired Fe isotope is now by far the most abundant fraction in the beam.

The selection of particles based on magnetic rigidity $B\rho$ over the $\frac{A}{q}$ ratio of the incoming particles, $\frac{A}{q} = \frac{B\rho}{v}$, was discussed in Sections 2.5 and 3.1. The identification of particles is based to a large part on the selectivity of the magnetic rigidity. Again, as the length of the spectrograph is fixed, the particle velocity v is measured as T_{OS} , introduced in Section 3.1.2, the timing difference between S800 object scintillator and E1 focal plane scintillator (cf. Section 2.5). For a fixed spectrograph $B\rho$ this time scales directly with the particles $\frac{A}{q}$. Simultaneously, the energy loss in the focal plane ionisation chamber is measured, scaling with Z^2 (cf. Section 2.5). Correlating both, ionisation chamber readout and T_{OS} , yields isobaric resolution and the missing link to unique particle identification of the outgoing beam (PID-OUT).

Nonetheless, some ambiguity remains: a given magnetic rigidity of the spectrograph allows for a set of slightly different trajectories with corresponding slightly different velocities. These trajectories can be observed as correlations between the time of flight T_{OS} and the CRDC readings. Analogously, the energy loss in the ionisation chamber is correlated to the CRDCs. By empirically removing these correlations the quality of the separation can be improved significantly.

Correlation between T_{OS} and CRDCs / Ionisation Chamber and CRDCs

The finite diameter of the S800 spectrograph and its wide acceptance permit a limited bundle of curves at fixed $B\rho$. Different paths and different velocities are manifest in a correlation between T_{OS} (cf. Section 3.1.2) and CRDCs (cf. Section 2.5) and ionisation chamber (cf. Section 2.5) and CRDCs.

The correlation between the time of flight T_{OS} and the CRDC readings is illustrated in Figure 3.5a for a typical run of ^{66}Fe . Here, X is the position in the dispersive plane for CRDC1, ΔX is the difference in X between CRDC1 and CRDC2. Y and ΔY are defined analogously in the non-dispersive plane. RF is the radio frequency of the cyclotron. In all cases, the abscissa gives T_{OS} .

$X, \Delta X, Y, \Delta Y$ are indeed correlated with T_{OS} . A linear correction of the correlation, replacing $X, \Delta X, Y, \Delta Y$ respectively by

$$\Xi_{X,\Delta X,Y,\Delta Y} = a_{X,\Delta X,Y,\Delta Y} + b_{X,\Delta X,Y,\Delta Y} T_{OS} \quad (3.1)$$

yields a significant improvement of the corresponding spectra. Figure 3.5b shows the same data as Figure 3.5a after linear correlations have been removed empirically. The improvement is that, based on the corrected result, it is possible to gate out contaminants that were not visible before.

T_{OS} of the same run is shown as histograms with and without correction in Figure 3.6. Only the correction of T_{OS} makes a significant, background reducing identification of outgoing particles possible.

The correlations between the ionisation chamber and the CRDCs were processed in a strictly analogous way yielding results of similar quality.

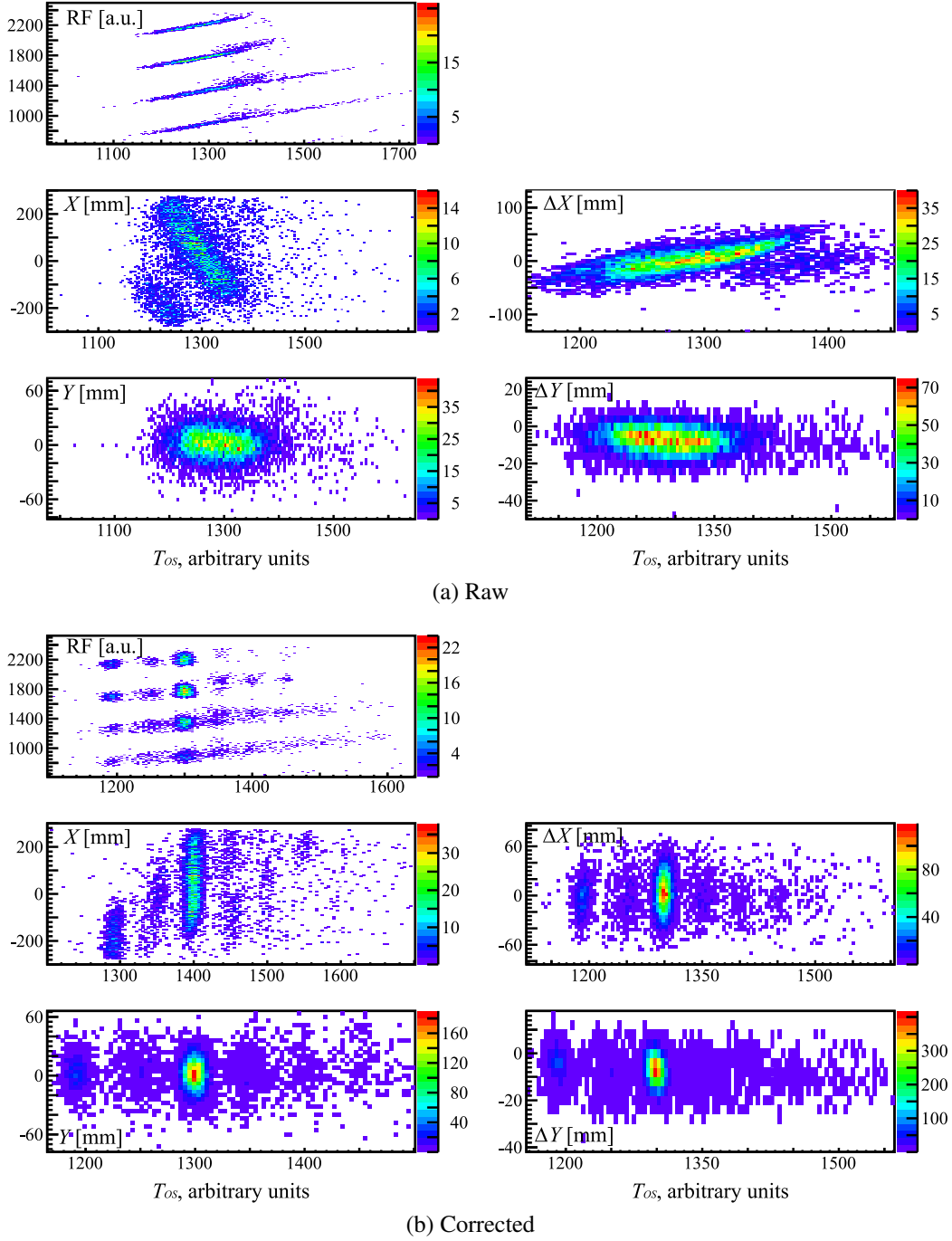


Figure 3.5: Raw and corrected plots of CRDC and RF readings over T_{OS} , Run 171 (3500 μm), ^{66}Fe . The colour scale gives the number of counts. For more details please see text.

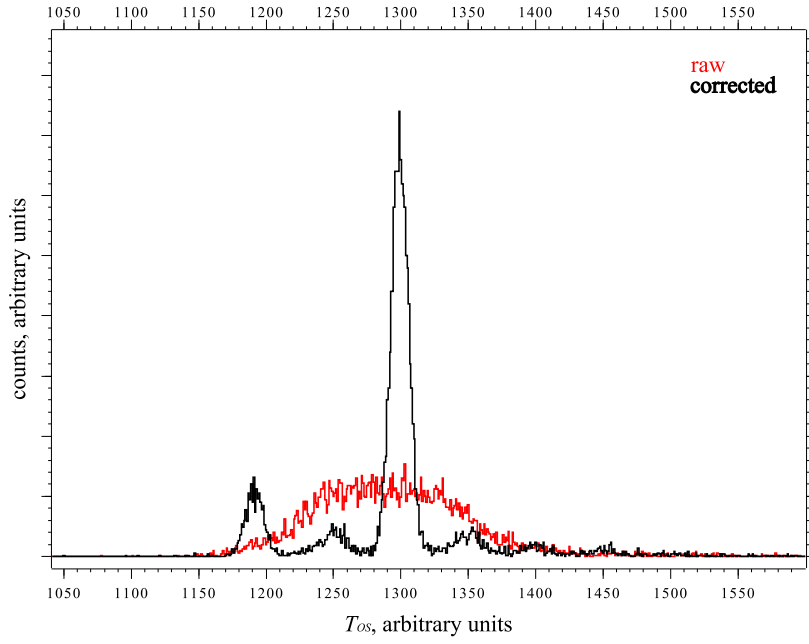


Figure 3.6: T_{OS} with and without correlations. Run 171 (3500 μm), ^{66}Fe .

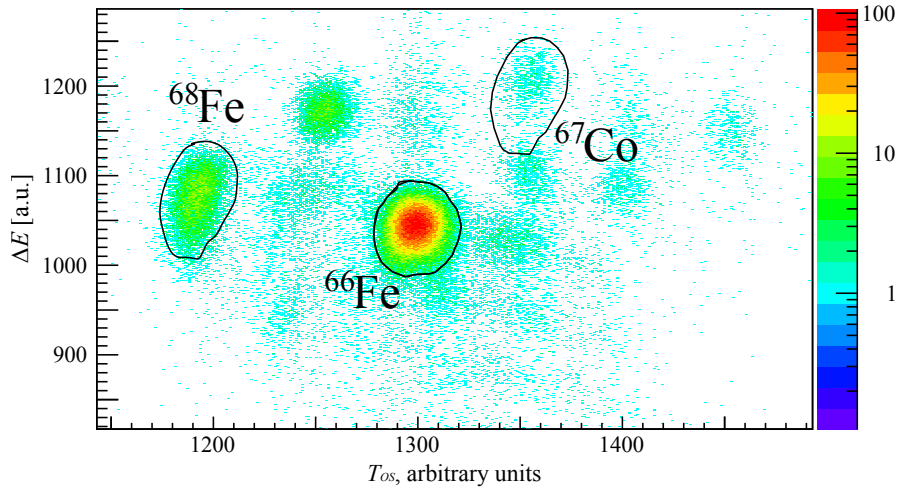


Figure 3.7: Typical PID-Out plot, ^{66}Fe , 1490 μm . The colour scale gives the number of counts. The data stream has been separated on ^{66}Fe beforehand on a pure T_{PID} basis. Note the suppression of the former main contaminant ^{67}Co .

Identification

Removal of correlations (cf. Section 3.1.3) brings more structure in T_{OS} to light, that could not have been observed beforehand, as shown in Figure 3.6.

T_{OS} is the flight time from object scintillator to E1 scintillator of the S800 spectrograph (cf. Section 2.5). As the path length is fixed, this is equivalent to a measurement of a given particle's velocity.

Thus, T_{OS} is directly related to the projectiles $\frac{A}{q}$ via $\frac{A}{q} = \frac{B\rho}{v}$. Therefore, the correction presented in Section 3.1.3 enhances the resolution of the particle separation significantly. An improvement of equal quality is reached for the correlation of ionisation chamber and CRDCs (cf. Sections 2.5 and 3.1.3).

As sketched above (cf. Section 3.1), the particle identification is completed by combining the T_{OS} reading with the energy loss data from the ionisation chamber. These grant access to the projectile's nuclear charge over the Z^2 dependence of the stopping power. A two dimensional plot of ΔE over T_{OS} is shown in Figure 3.7. Identification of outgoing particles is performed by setting a two dimensional gate, an example is given. At the same time, this illustrates the success of the separation on the incoming beam by highlighting the remnants of the former main contaminant ^{67}Co . The separation could also have been done in nearly the same quality based solely on the T_{OS} information. This degree of beam purity is a unique advantage of inverse kinematics Coulomb excitation experiments.

3.2 Calibration of γ -Spectra

As the experimental aim is essentially based on γ -spectroscopy, only events involving a hit in the E1 scintillator and the detection of a γ -ray with the SeGA detector (cf. Section 2.2) within a narrow time window³ were written to disk. The SeGA detectors were time matched as shown in Figure 3.8 and a gate was set on the prompt peak to suppress background.

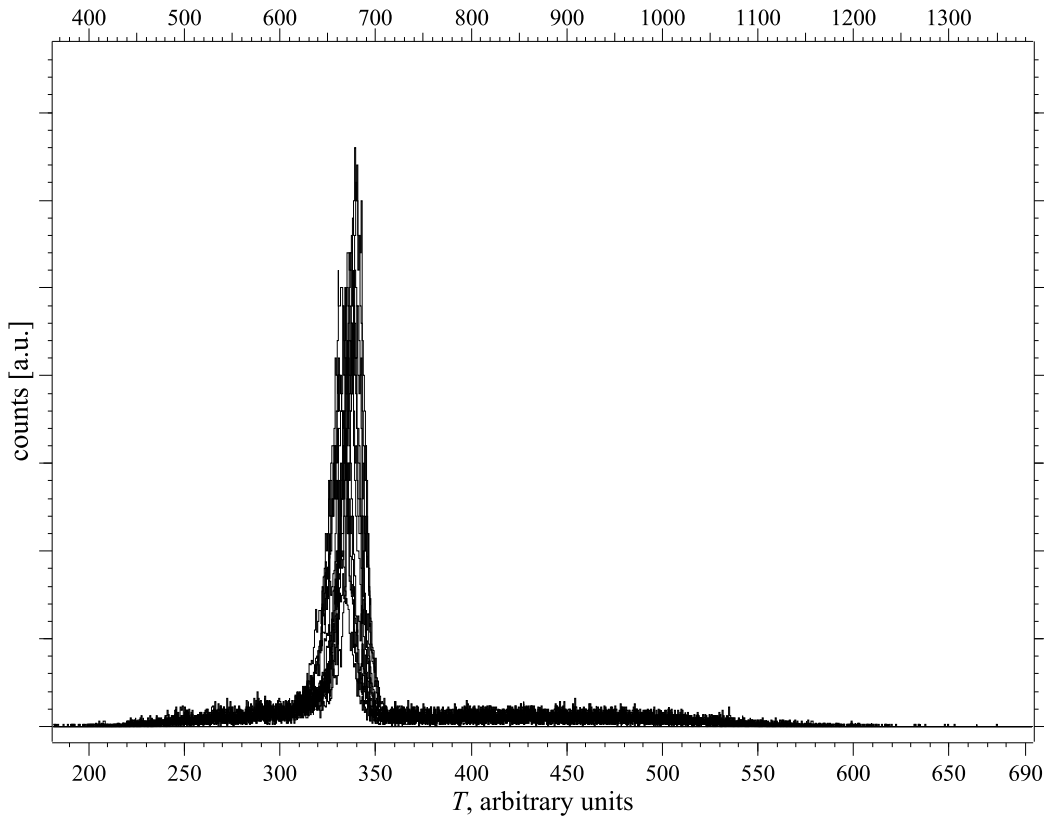


Figure 3.8: Time Spectra. ^{62}Fe , 700 μm

Energy and Efficiency Calibration

Energy and efficiency of SeGA were calibrated using a ^{152}Eu source. The efficiency calibration is based on two continuously differentiable continued polynomials of second order, as illustrated in Figure 3.9. The source was issued by the

³a few 100 ns

National Bureau of Standards as Standard Reference Material 4218-C [10]. Special care was taken to account for dead time losses in the data acquisition system⁴ to allow for an absolute efficiency calibration. In combination with data taken with only one target⁵ this calibration may be used to calculate absolute Coulomb excitation cross sections in a forthcoming work.

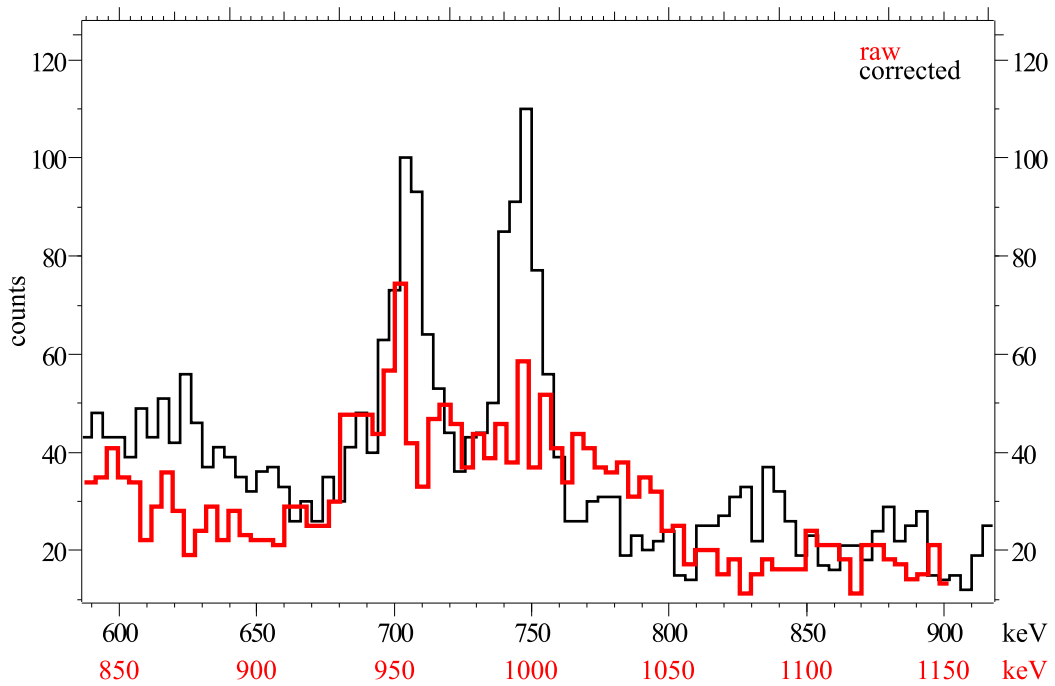


Figure 3.10: γ -ray spectrum of fast and slow component of the $2_1^+ \rightarrow 0_1^+$ transition in ^{64}Fe at 3000 μm distance, with and without Doppler correction in the detector ring under 30° .

⁴K. Starosta, private communication

⁵without degrader in our case, to measure the beam velocity after the target

Doppler Correction

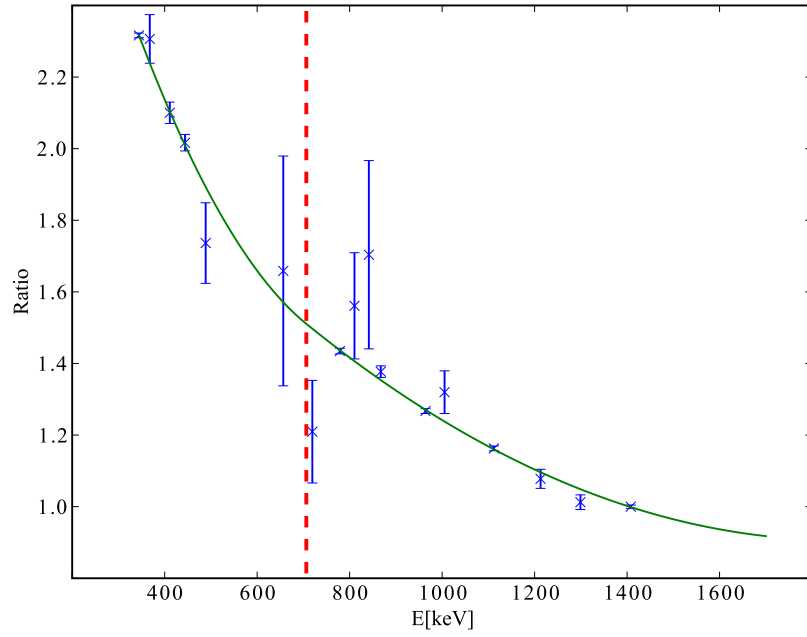
High beam velocities during γ -emission and large detector volumes lead to drastic Doppler broadening of observed γ -lines. The Segmented Germanium Array (SeGA), introduced in Section 2.2, was conceived for experiments with fast radioactive ion beams. The detector segmentation is optimised for azimuthal angular resolution as illustrated in Figure 2.2. Equation 3.2 gives the relation between the rest frame energy of the emitted γ -ray E_0 , the speed of the particle emitting v/c and the azimuthal angle θ to the observed energy in the laboratory frame E_{Lab} .

$$E_{Lab} = \frac{E_0 \sqrt{1 - v/c^2}}{1 - v/c \cos(\theta)} \quad (3.2)$$

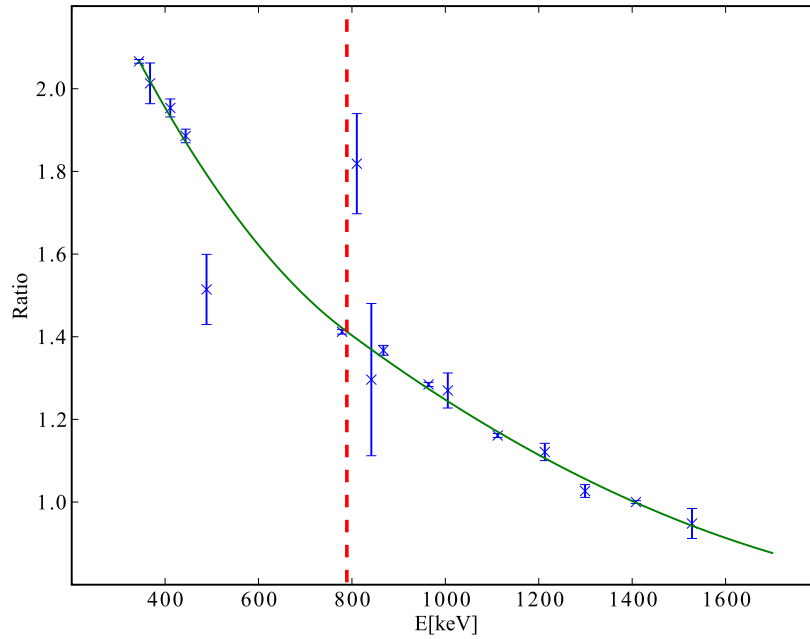
E_0 is known from previous experiments and the data sheets [34, 18], v/c is known from the spectrograph $B\rho$. Thus, the crucial quantity for a meaningful Doppler reconstruction is the azimuthal angle θ .

Assuming that all γ -rays are emitted from the centre of the degrader (that is the only possible assumption at this stage as this is the only static part in the configuration, cf. Section 2.3) and that the angle of emission of the γ -ray is defined by this point and the SeGA segment with the first interaction, a Doppler correction is possible as illustrated in Figure 3.10 for the case of ^{64}Fe at a distance of 3000 μm . $^{64,66}\text{Fe}$ were Doppler corrected using the spectrograph $B\rho$ from runs with the target only. As such runs were not taken for ^{62}Fe , the corresponding γ -spectra are corrected using the $B\rho$ from runs with target and degrader.

The cathode readout drift chambers in the S800 spectrograph's focal plane box allow for the tracking of a particle's trajectory through the spectrograph (cf. Section 2.5). Using this information, the angle of the particle's trajectory with respect to the degrader can be calculated. This improves the Doppler correction. The primary beam rate for $^{62,64}\text{Fe}$ was so high, that the CRDCs could not be used during the experiment (cf. Section 2.5), tracking was therefore only possible for ^{66}Fe .



(a) Efficiency calibration for the detectors at 30°



(b) Efficiency calibration for the detectors at 140°

Figure 3.9: Efficiency calibration used in the analysis. The solid line represents a fit with continuously differentiable continued polynomials of second order. The dashed line indicates the boundary between the two polynomials.

Chapter 4

Lifetime Analysis

In conventional (slow beam) recoil distance Doppler shift experiments the areas under the peaks of fast and slow component (cf. Figure 2.4) are integrated. These—normalised—intensities are fit in τ with a function¹ of the target-degrader-separation distance. When beam velocity, target and degrader thickness or target-degrader separation increase, several effects contribute significantly to the line-shape of the peaks. Thus, new sources of systematic errors arise and with them the need of a dedicated approach to analyse experiments with radioactive ion beams from fragmentation reactions.

- Fragmentation products are fast (e.g. 40% c for the ^{66}Fe beam used in this work), the relativistic Lorentz boost [30] cannot be neglected any more.
- Target-degrader separation distances are not negligible compared to the detector size. Thus, a continuously changing emission angle and a continuous change of the solid angle subtended by the detector crystal have to be considered.
- To compensate for low beam rates, the targets have to be very thick in comparison to stable beam experiments. If the target is not very thin compared to the separation distances the stopping process cannot be assumed to be instantaneous. Thus, a velocity profile in target and degrader has to be considered. This effect becomes dominant when very short distances of the order

¹Nowadays, the function of choice is given by the Differential Decay Curve Method [15], in cases with a known feeding pattern one may also use a combination of exponential functions [5].

of the target thickness are measured. This effect has been incorporated in the analysis procedure for the experiments at hand (cf. Section 4.1).

A lineshape simulation for recoil distance Doppler shift experiments, especially at intermediate energies, has been written in FORTRAN and PYTHON to analyse the data set at hand. The code implements the lineshape simulation described in Appendix A in its full generality, representing a generalisation of the procedure used in [43, 17]. This chapter shall focus on the determination of the lineshape parameters that are fed into the lineshape function, leading ultimately to the fit of the lifetime. The lineshape function itself is derived in full detail in Appendix A and defined in Equation A.24.

The main features of the lineshape simulation can be summarised as follows:

- Target, separation between target and degrader, degrader and the pathway behind were discretised and velocities at each sampling point were calculated as discussed in Section 4.1 to treat the relativistic Lorentz Boost in a quasi continuous fashion.
- The solid angle subtended by the SeGA capsules was respected as discussed in Section 4.5 in the same quasi continuous fashion.
- Feeding: As addressed in Section 2.4, Winther and Alder [50] showed that Coulomb excitation at intermediate beam energies is almost completely a one-step process. This assures, that only the first 2^+ state in the projectile and no higher lying states are populated. This makes the analysis highly robust as no assumptions on feeding—however weekly—from other transitions have to be made. Apart from yielding a high cross section this is one of the major advantages that led to the choice of this type of reaction.
- In analyses similar to the one at hand [43, 17], it was found suitable to summarise energy and angular straggling of the projectiles in four different width parameters (for each nucleus) respectively corresponding to decays before $(\sigma_T^{30^\circ, 140^\circ})$ and after the degrader $(\sigma_D^{30^\circ, 140^\circ})$ in the two rings. We followed this procedure. As discussed in Section 4.3, a rigid normalisation condition demands these parameters to be free fit parameters.

The lineshape function is fit simultaneously to all distances and both rings in the lifetime τ , the target-degrader excitation ratio \mathbb{D} (cf. Section 4.4), the global scaling parameters $\mathcal{N}_{30^\circ, 140^\circ}$ (cf. Section 4.3) and the four width parameters $\sigma_{T,D}^{30^\circ, 140^\circ}$. A detailed description of the procedure can be found in Section 4.6.

4.1 Discretisation and Velocities

The main feature of the lineshape simulation is the correct treatment of the gradual stopping of the projectile in target and degrader and the resulting changes in the relativistic Lorentz Boost [30].

The simulation discretises target, separation between target and degrader, degrader and the (user-defined) run out zone into a finite number of steps. The present implementation of the simulation allows for an arbitrary step number. In the experiment at hand the values of 10, 10, 6 and 10, respectively, yielded a very good description. These step numbers are above the lower limit for a smooth description. They are not canonical; increasing the number of steps will do no harm. For the cases at hand it will not bring any further improvement in the description.

The velocities at the steps in target and degrader have to be estimated using a stopping power calculation based on the measured sampling points. For $^{64,66}\text{Fe}$ three sampling points of the velocity are available (before the target², after the target and after the degrader). The other velocities were interpolated using the software LISE++ [47, 46].

The measured velocity after the target is reproduced by this calculation within $\approx 2\%$ (5%) for ^{66}Fe (^{64}Fe), starting from the measured velocity before the target. The measured velocity after the degrader agrees with the calculated velocity after the degrader on the same order of magnitude, starting from the measured velocity after the target. To bring the calculation in agreement with the experimental stopping power, the difference between measured and calculated values was distributed linearly on the steps in between, separately for target and degrader. The case of ^{62}Fe is more complicated and will be discussed in Section 4.2. All velocities used for the simulation are summarised in Table 4.1.

²measured with empty beam tube

^{66}Fe			^{64}Fe		^{62}Fe	
Step	[mm]	v/c	[mm]	v/c	[mm]	v/c
before the target						
0	0.0	$0.407(4)^m$	0.0	0.420^m	0.0	$0.425(4)^m$
in the target						
1	0.03	0.400	0.03	0.413	0.03	0.416
2	0.06	0.395	0.06	0.409	0.06	0.411
3	0.09	0.389	0.09	0.404	0.09	0.407
4	0.12	0.384	0.12	0.399	0.12	0.402
5	0.15	0.379	0.15	0.394	0.15	0.397
6	0.18	0.373	0.18	0.388	0.18	0.391
7	0.21	0.367	0.21	0.383	0.21	0.386
8	0.24	0.360	0.24	0.377	0.24	0.380
9	0.27	0.353	0.27	0.371	0.27	0.374
after the target						
10	0.30	$0.346(3)^m$	0.30	$0.364(4)^m$	0.30	$0.368(4)^f$
in the degrader						
11	0.05	0.335	0.07	0.357	0.05	0.360
12	0.10	0.327	0.13	0.347005082	0.10	0.353
13	0.15	0.319	0.20	0.337	0.15	0.346
14	0.20	0.311	0.27	0.325	0.20	0.339
15	0.25	0.301	0.33	0.312	0.25	0.330
after the degrader						
16	0.30	$0.291(3)^m$	0.40	$0.298(3)^m$	0.30	$0.322(3)^m$

Table 4.1: Velocity Set. m : Measured, from spectrograph $B\rho$. f : Fit, extracted from spectrum as described in Section 4.2. All other values are interpolated using LISE++. All velocities are given at the entry to the corresponding section. Errors are given—for measured values only—in root mean square.

The Nb foils were rolled at the IKP from a 0.5 mm foil. Measurements with a micrometer screw showed variations between 0.29 mm and 0.31 mm over the accessible area for the 0.3 mm foil. The variations are due to the intrinsic skewness of the rolling setup. The variation of the 0.4 mm foil—rolled with the same device—is therefore of the same absolute number but of lesser relative impact. The variations of both foils are at least a factor of five smaller than the step sizes (cf. Table 4.1) used in the simulation. The gold foil was bought from a commercial supplier at the design thickness. The production of large sheets of metal necessitates a high parallelism of the rolling setup. As this foil was cut from a rather large sheet, little variation in its thickness are to be expected.

4.2 Calibration of Angles

The setup has a limited degree of freedom in the positioning of the plunger device. This liberty becomes manifest in the simulated peak positions. These do not overlap with the γ -ray spectra from SeGA when simulation and spectra are prepared with the nominal angles of 30° and 140° . The Doppler correction is calculated with respect to the degrader. If the degrader is misplaced, the correction needs to be changed (cf. Section 3.2). The position of the plunger device inside the beam tube can in praxis only be validated³ up to ≈ 1 mm. However, the necessary adjustment of angles is small. It was found suitable to include the angle offset as a free parameter in the fit of the lineshape description to the data set, resort the data with the angles found and then to refit the data set with fixed angles to cross check.

Calibration of Angles and Velocities, the Case of ^{62}Fe

For ^{62}Fe the velocity set obtained analogously to Section 4.1 with LISE++ was based on only one $B\rho$ sampling point, due to limitations in available beam time. It was impossible to find an angle offset that allowed a description of fast and slow component in the spectra of ^{62}Fe . To solve this issue, the angle was fit to the slow

³The contact of collar and fence is verified by hand. The insertion depth is cross checked, however carefully, with a tape measure of a 1/16 Inch scale. 1 mm is about half of that scale. It is unlikely that such a heavy device as the plunger will slide back.

component only for ^{62}Fe . The data set was resorted with the calibrated angle, the v/c after the target was determined from the fast component's position and then used as a second sampling point for the velocity set calculation in Section 4.1. Subsequently, all parameters were fit to both components. The calibrated angles are summarised in Table 4.2.

A	Ring 1 (30°)	Ring 2 (140°)
62	30.79°	140.02°
64	30.91°	139.07°
66	31.14°	139.39°

Table 4.2: Calibrated Angles. All angles can be varied by $\approx 0.2^\circ$ before a misalignment between simulation and measured data is observed with the naked eye. The numerical error of the fit is of the order of the last digit given.

4.3 Normalisation

Normalisation of the Spectra

A requirement for any recoil distance Doppler shift lifetime measurement is that the number of γ -rays observed for the transition of interest for each distance must be equal. Experimentally this cannot be realised. Different measurement times at different distances and fluctuations in the beam current make a normalisation of data sets from different distances necessary. The most elegant choice is to normalise the γ -spectra on the rate of the incoming particles of interest. This rate is proportional to the integral of particles in the outgoing PID gate described in Section 3.1.3. Spectra taken at different distances and normalised to this rate should have the same integral number of γ -events in fast and slow component after background subtraction. As the application of the same background subtraction to different spectra is virtually impossible an additional factor $\mathfrak{N}_{30^\circ,140^\circ}$ was introduced for each ring of detectors⁴ and each distance to correct the normalisation within the region of interest. $\mathfrak{N}_{30^\circ,140^\circ}$ are set once and for all during the analysis.

⁴only for the 30° ring in the case of ^{62}Fe . As discussed later on, the ring at 140° suffers from a contamination. Here, it served only as a cross check for results obtained from the forward ring.

They are especially *not* free fit parameters but directly read from the γ -spectra. They are independent of the lineshape analysis. The results are summarised in Tables 4.3, 4.4 and 4.5.

Normalisation of the Lineshape

A main gauge for the quality of a lineshape simulation is the correct description of the integral of fast and slow component. By default, the lineshapes from the simulation have an exactly identical integral for all distances for a given ring (as do the experimental γ -ray spectra after the normalisation using $\aleph_{30^\circ, 140^\circ}$ in Section 4.3). The initial value of this integral in the lineshape simulation is not related to the experimental value. Therefore, the value of this integral for each ring has to be a free fit parameter.

This global⁵ scaling parameter for each ring ($\aleph_{30^\circ, 140^\circ}$, not related to $\aleph_{30^\circ, 140^\circ}$) is part of the set of fit parameters. The unconstrained fit may converge into a χ^2 -minimum that does not necessarily match the integral condition at the beginning of this section. To force the algorithm to prefer solutions describing the integral content correctly, the lineshape is integrated numerically after each iteration and renormalised via the global scaling parameters $\aleph_{30^\circ, 140^\circ}$. These are not free, but strongly constrained fit parameters.

The integral condition can only be fulfilled, if sufficient degrees of freedom are available. It proved impossible to find a sensible agreement between lineshape simulation and experimental data set by fitting only through scaling parameters, \mathbb{D} and τ while the rigorous normalisation condition was in place. At this point it became necessary to include the width parameters $\sigma_{T,D}^{1,2}$ as free parameters into the fit.

4.4 Excitation Ratio

Coulomb excitation of the projectile occurs on the target and on the degrader. The latter one is a disturbing effect that needs to be corrected in the analysis. The fast component, originating from decays in the target and between target and

⁵applying to all distances

^{66}Fe			
[mm]	Particles	\mathfrak{N}_{30°	\mathfrak{N}_{140°
1.49	63749	1.	1.
3.5	105250	1.0952	1.1939
6.0	72625	1.0794	1.125
9.0	79422	1.2305	1.0833
20	97436	1.2456	1.13592

Table 4.3: Normalisation Factors for ^{66}Fe

^{64}Fe			
[mm]	Particles	\mathfrak{N}_{30°	\mathfrak{N}_{140°
0.4	227912	1.150	1.028
1.0	168274	1.023	1.13125
1.8	210642	1.198	1.034
3.0	151459	1.	1.
4.5	211895	1.102	1.077
6.0	179812	1.130	1.110
12	239229	1.232	1.058

Table 4.4: Normalisation Factors for ^{64}Fe

degrader, cannot be affected. The slow component, originating from decays in and after the degrader will be affected at short and intermediate distances. At long distances, however, practically all projectile particles that were initially excited in the target will have emitted γ -rays before hitting the degrader. Therefore, the slow component in spectra taken at long distances should originate almost completely from projectile Coulomb excitation on the degrader.

For each nucleus, a longer distance was measured to gain sensitivity for the ratio between Coulomb excitation on target and degrader, \mathbb{D} , as defined in Equation A.23. The distances are tabulated in Table 4.6, given in μm and in relation to

^{62}Fe		
[mm]	Particles	\aleph_{30°
0.1	501054	1.03623
0.3	500790	1.09160
0.7	572158	1.
1.2	553290	1.33645
2.0	556872	1.02878
4.0	381237	1.144

Table 4.5: Normalisation Factors for ^{62}Fe

the state's lifetime. The parameter \mathbb{D} is fit simultaneously with the lifetime, τ , to all distances in both rings of detectors.

The final lineshape is shown unfolded into its target and degrader component in Figure 4.1. In forward rings (here 30°), γ -rays emitted from faster particles are shifted to higher energies (cf. Equation 3.2). Photons emitted between target and degrader—stemming solely from excitations on the target, solid black line—are therefore contributing only to the right peaks in Figure 4.1. The left peak is a sum of excitations on the degrader, solid red line and excitations on the target. At the shortest distance measured for ^{66}Fe , $3500\text{ }\mu\text{m}$, target and degrader excitations contribute equally to this slow component on the left side of the spectrum. At $6000\text{ }\mu\text{m}$ the share of degrader excitations contributing to the slow component is already way larger. When the separation increases, more and more particles that are excited on the target decay before reaching the degrader. Finally, at $20000\text{ }\mu\text{m} \approx 5\tau$, the fraction of excitations from the target contributing to the slow component in the spectrum is nearly at zero.

4.5 Solid Angle Coverage

This work considers for the first time the change of solid angle subtended by a SeGA detector capsule over the flight path of an excited projectile. Based on the work of Guest [26] the lineshape is corrected for the solid angle by a cylindrical

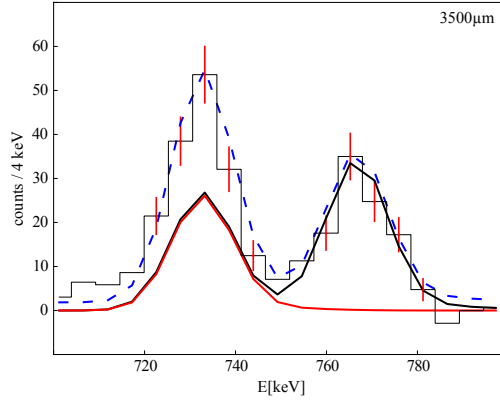
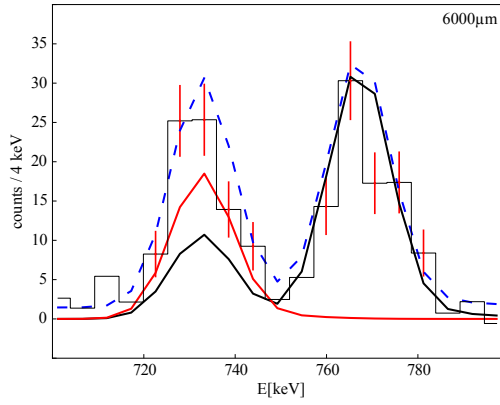
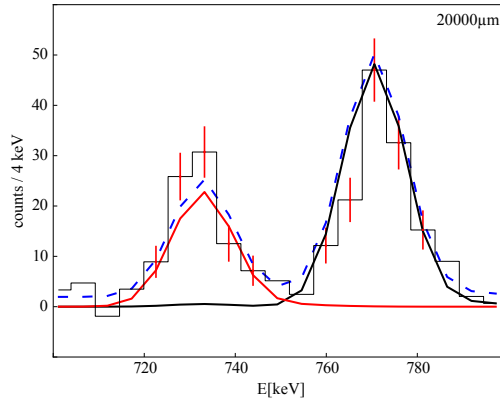
(a) 3500 μm (b) 6000 μm (c) 20000 μm

Figure 4.1: Lineshape description of γ -spectra of the fast and slow component of the $2_1^+ \rightarrow 0_1^+$ transition in ^{66}Fe taken with detectors under 30° . The lineshape is unfolded into excitation on target and degrader for three typical distances. Excitation on target: black solid line. Excitation on degrader: red solid line. The sum is plotted with an arbitrary offset of a few counts as a blue dashed line.

A	v/c_T	$\mu\text{m}/\text{ps}_T$	τ [ps]	Distance [μm]	Distance [τ]
62	0.368(4)	110.324	8.0(10)	4000	4.53
64	0.364(4)	109.124	10.3(10)	12000	10.7
66	0.346(3)	103.728	39.4(40)	20000	4.89

Table 4.6: The long distances measured in order to gain sensitivity to the excitation ratio \mathbb{D} . The distance is given in μm and as the flight time in multiples of the state's lifetime τ , cf. Section 5.1.

detector capsule (cf. ε_Ω in Section A.3). The solid angle is evaluated for every of the discrete steps defined in Section 4.1. Figure 4.2 illustrates the solid angle subtended by a single SeGA capsule in forward and backward angles.

4.6 How to Obtain the Final Results

As discussed in the previous sections, the fitting parameters of the lineshape are apart from the lifetime τ , the target-degrader excitation ratio \mathbb{D} (cf. 4.4), the global scaling parameters $\mathcal{N}_{30^\circ, 140^\circ}$ (cf. 4.3) and the four width parameters $\sigma_{T,D}^{30^\circ, 140^\circ}$.

After an initial simultaneous fit to all rings and all distances⁶, that brought the lineshape into the right shape and moved the parameters within the range of the present numerical errors, the sensitivity of the fit for the lifetime was tested. It was found, that the region around the peak summits is most susceptible to changes in the lifetime, whereas the tails of the peaks are—as expected—hardly sensitive at all. The final χ^2 fit of the parameter set was therefore restricted to the peak's sensitive ranges. These are given in Table 4.7 and highlighted in Figures 4.3, 4.4, 4.5 as the values given with errorbars. The ultimate fit results are summarised in Table 4.7.

⁶for $^{64,66}\text{Fe}$, the 140° ring for ^{62}Fe suffers from a contamination and was only used as a cross check

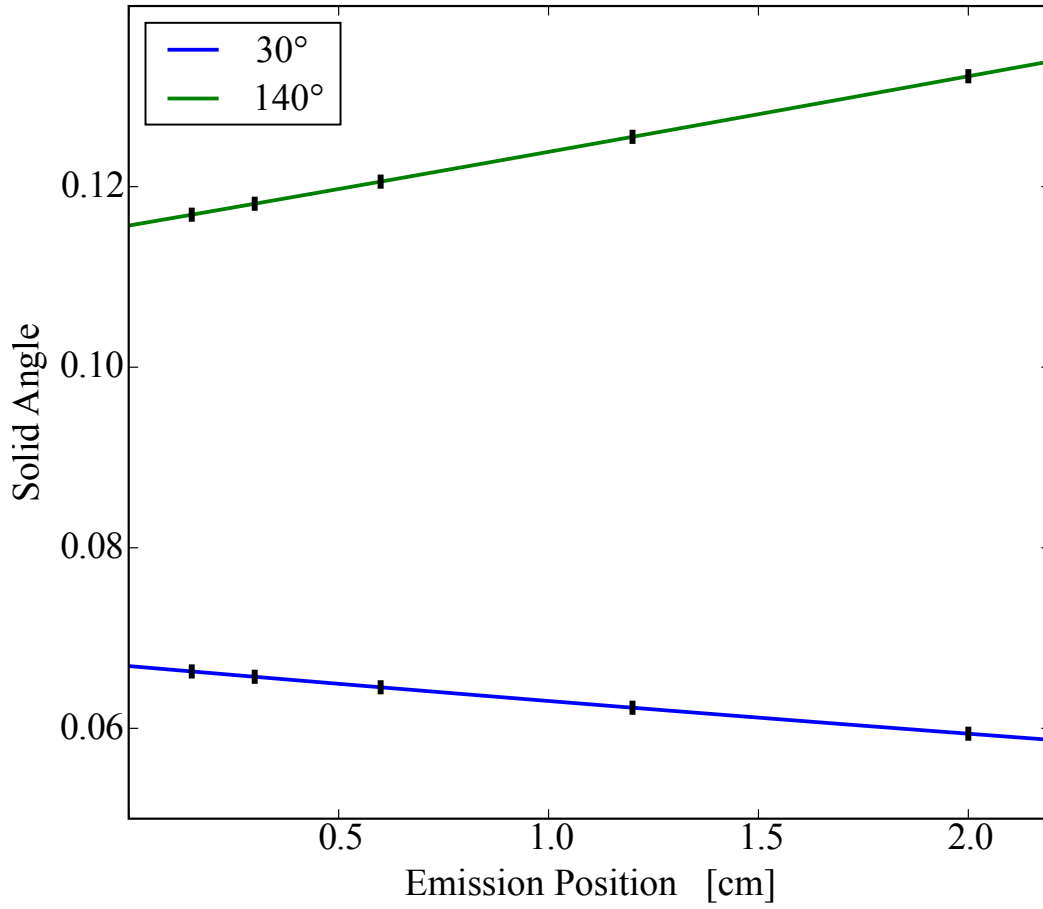


Figure 4.2: Calculated solid angle subtended by a SeGA detector crystal for different emission positions. The distances measured in the case of ^{66}Fe are indicated.

^{66}Fe

The fit to ^{66}Fe was performed completely unconstrained, simultaneously to both rings in all distances. The results are given in Table 4.7 and plotted in Figure 4.3. A magnificent agreement between the lineshape description and the experimental data, both to the naked eye and numerically, can be clearly seen.

	^{66}Fe	^{64}Fe	^{62}Fe
$\text{Range}_{\text{Slow}}^{30^\circ} [\text{keV}]$	[721, 742]	[938, 973]	[1134, 1160]
$\text{Range}_{\text{Fast}}^{30^\circ} [\text{keV}]$	[758, 780]	[999, 1028]	[1180, 1212]
$\text{Range}_{\text{Fast}}^{140^\circ} [\text{keV}]$	[422, 436]	[537, 554]	[627, 643]
$\text{Range}_{\text{Slow}}^{140^\circ} [\text{keV}]$	[446, 454]	[575, 590]	[659, 674]
$\tau [\text{ps}]$	39.4(40){35}	10.3(10){8}	7.8(10)
\mathbb{D}	0.40(5)	0.77(5)	0.49
\mathcal{N}_{30°	12.2(20)	3.4(7)	6.4
\mathcal{N}_{140°	2.2(2)	4.1	1.8
$\sigma_T^{30^\circ}$	6.75(0.37)	9.5(4)	10.7
$\sigma_D^{30^\circ}$	6.66(0.88)	9.0(4)	7.1
$\sigma_T^{140^\circ}$	4.30(0.44)	5.7(3)	5.8
$\sigma_D^{140^\circ}$	2.57(0.37)	5.0(3)	3.5

Table 4.7: Fit parameters. The errors given are the numerical errors from the χ^2 minimisation except for the error on τ . This represents the limits set by eye on τ when all other parameters are kept constant at the numerical optimum. For comparison the error from the χ^2 minimisation is given in curly braces.

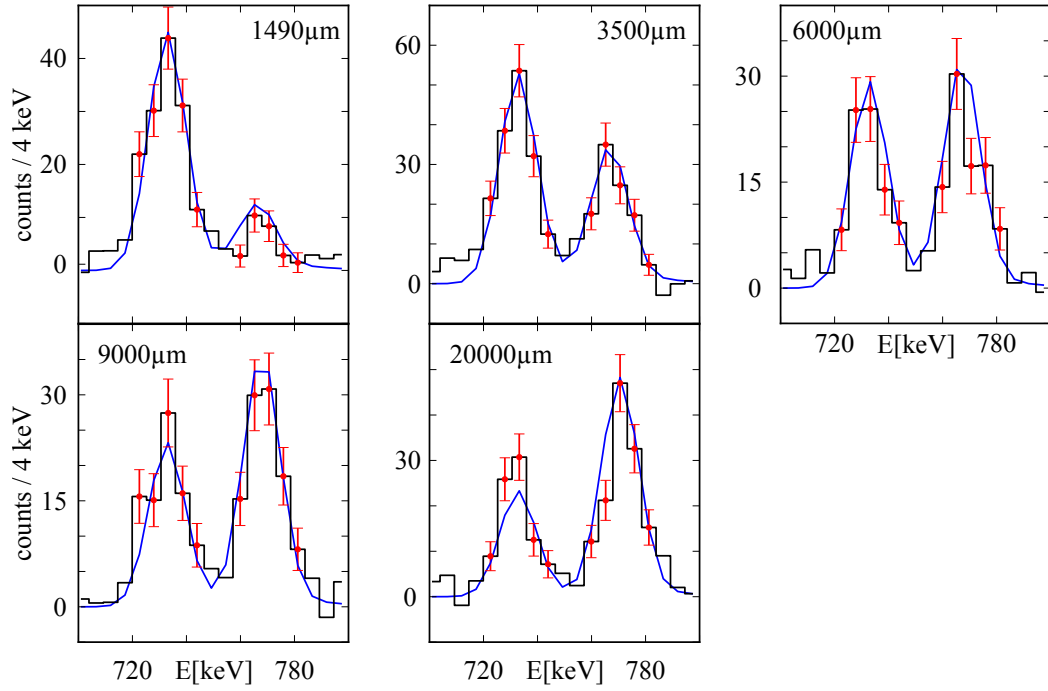
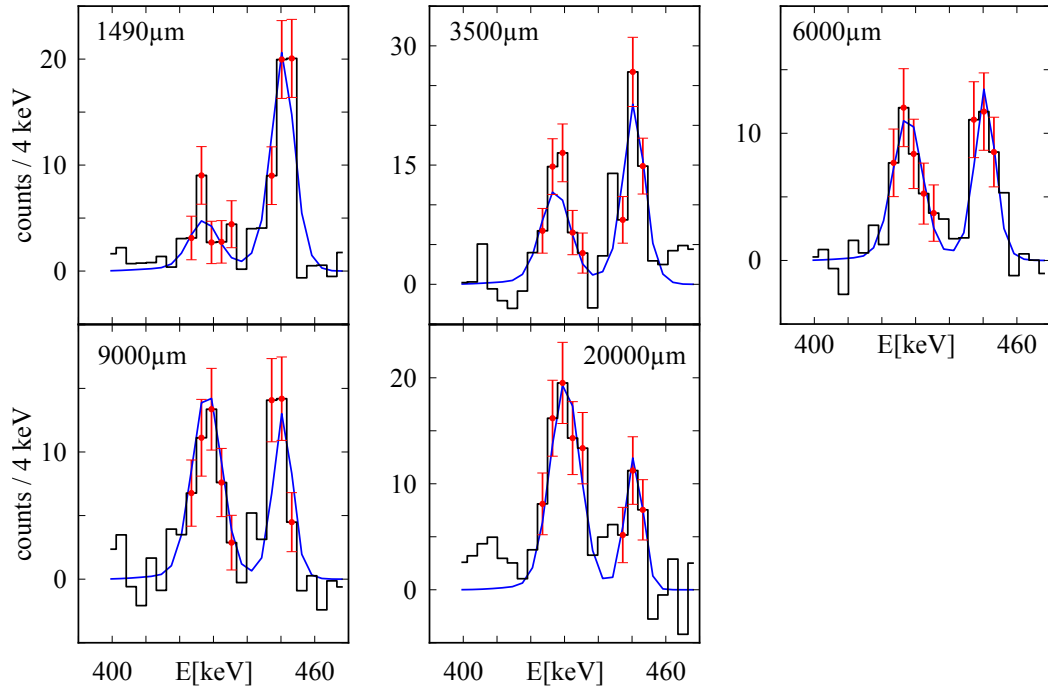
^{64}Fe

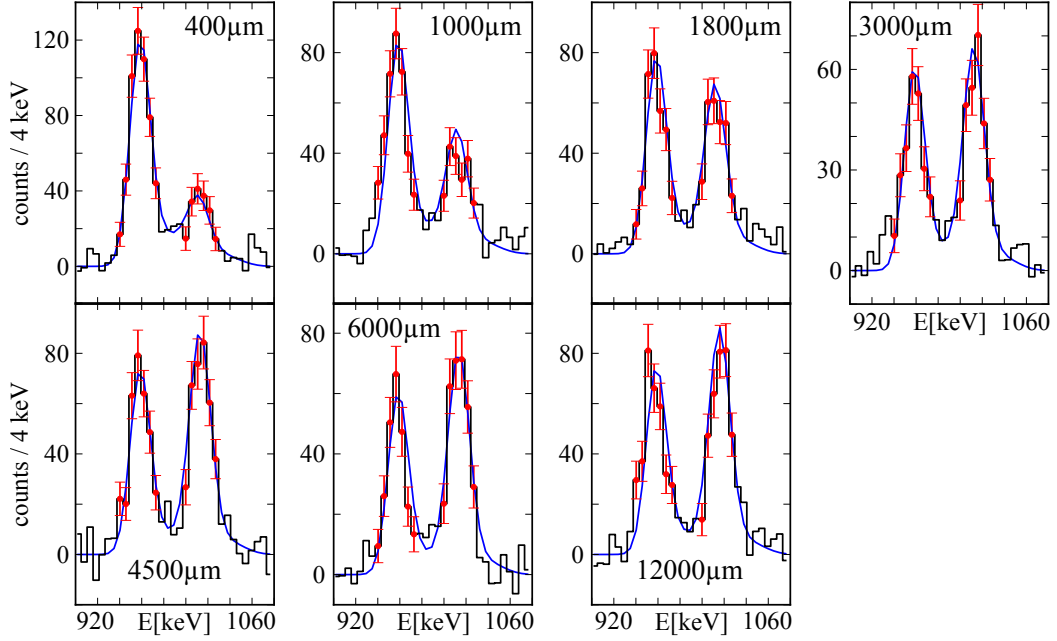
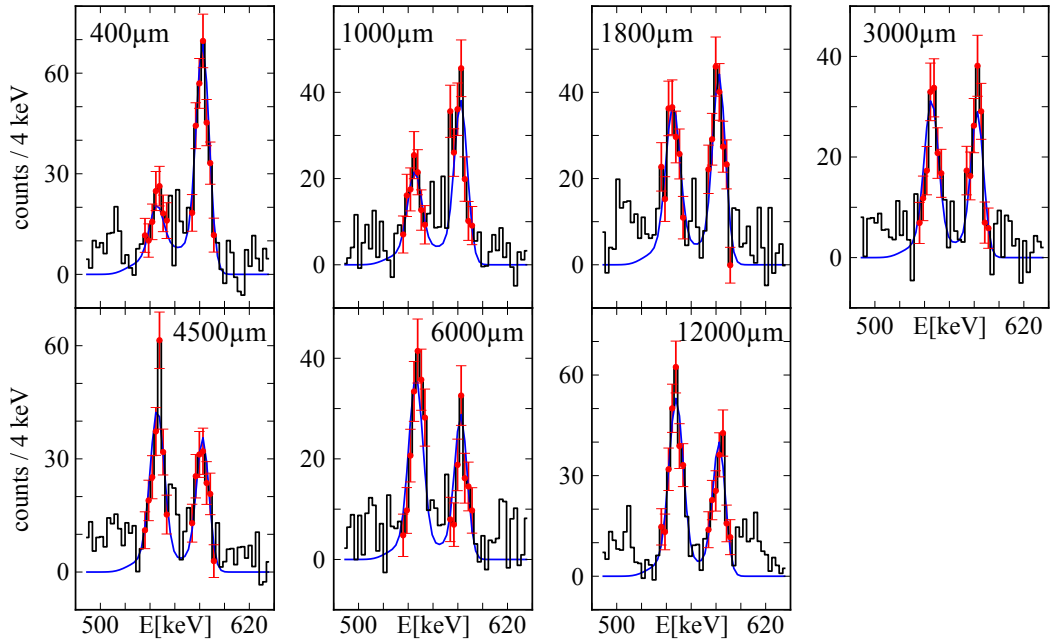
In the case of ^{64}Fe the fit algorithm did not converge. That made it necessary to divide the overall simultaneous fit into an automated and a manual part. First, all applying parameters were fit in an unconstrained way to all distances under 30° . In a second step, the parameters specific to the ring at 140° were fit in an unconstrained way to the corresponding data, while keeping τ and \mathbb{D} constant. In a final step, a variation of τ showed that a global minimum in χ^2 exists for both rings at the τ value of the ring at 30° . As the crucial parameter, τ , has been treated in a statistically sufficient way, this fit is—apart from minor technical constraints—in no way different from the one of τ in ^{66}Fe .

The results are summarised in Table 4.7 and plotted in Figure 4.4.

^{62}Fe

^{62}Fe suffered from an unidentified contamination in the data taken at 140° . It proved impossible to use this ring in the fitting procedure. The applicable parameters were fit to the ring at 30° and the ring specific parameters for 140° were determined within the limitations of the experimental data. In Figure 4.5, the results are plotted. For the 140° ring, the results obtained with 30° were plotted as a cross check. As before, all parameters are summarised in Table 4.7.

(a) ^{66}Fe , all distances at 30° (b) ^{66}Fe , all distances at 140° Figure 4.3: ^{66}Fe , all distances. Simultaneous fit.

(a) ^{64}Fe , all distances at 30° (b) ^{64}Fe , all distances at 140° Figure 4.4: ^{64}Fe , all distances. Simultaneous fit.

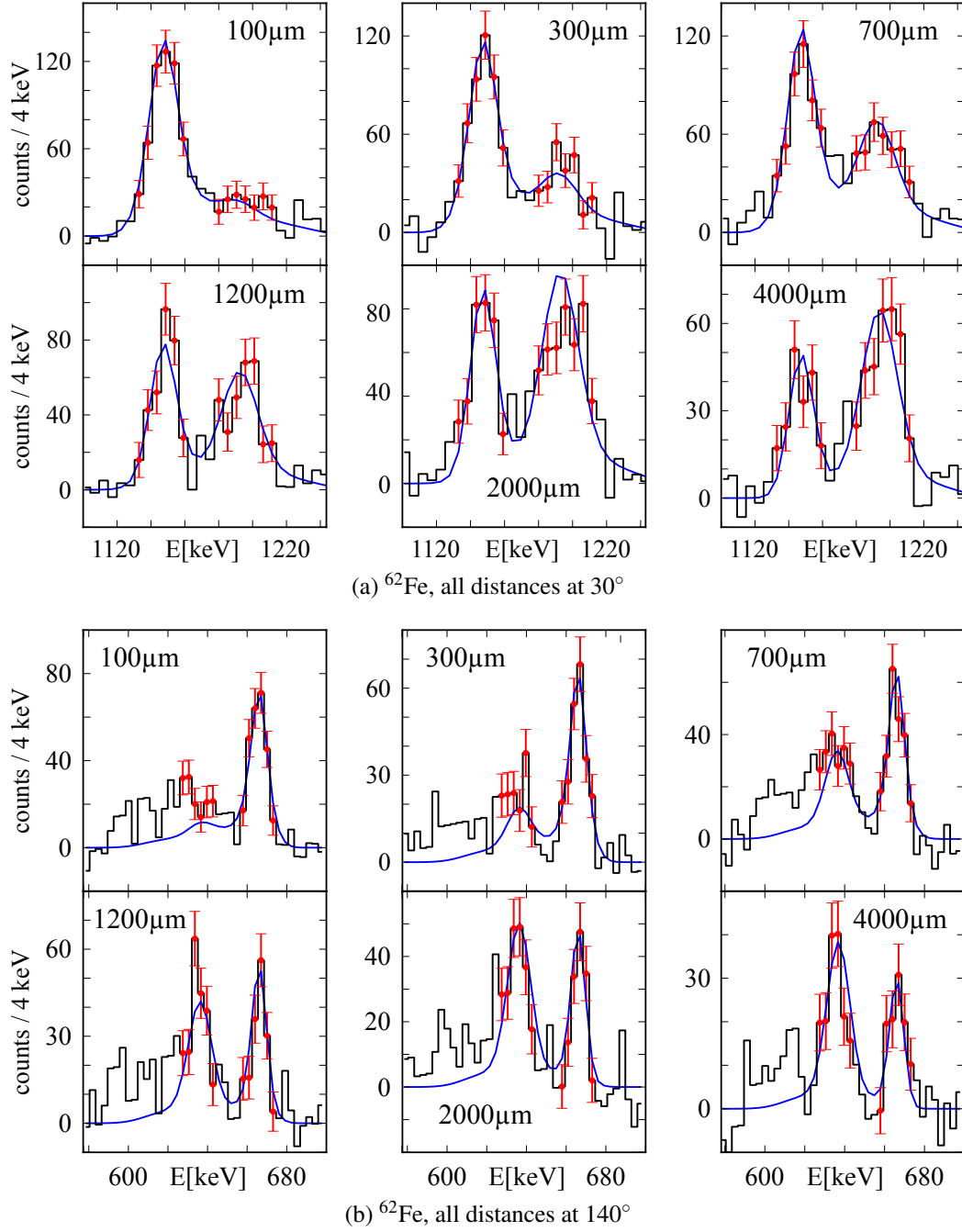


Figure 4.5: ^{62}Fe , all distances. Simultaneous fit to the data taken at 30° , results are also shown in comparison to the data taken at 140° .

Chapter 5

Discussion

5.1 Placement of Results

The level lifetime τ is related to the reduced transition probability $B(E2)$ via

$$1/\tau = 1.22 \cdot 10^9 \cdot E_\gamma^5 \cdot B(E2)$$

where the $B(E2)$ is defined as

$$B(E2 : J_i \rightarrow J_f) = \frac{1}{2J_i + 1} \langle \psi_i || E2 || \psi_f \rangle^2$$

Being a quantitative measure for E2 or electric quadrupole transition strength, the $B(E2)$ can serve as an indicator of the “collectivity” of a given transition.

Hardly any transition rates were known in the highly interesting $N = 40$ region around ^{68}Ni when the experiments presented in this work were undertaken, as shown in Figure 5.1. Only recently, Ljungvall et al. [33] reported lifetimes of the 2_1^+ states in $^{62,64}\text{Fe}$ hinting at an increase of collectivity in neutron rich iron nuclei towards $N = 40$. This work confirms this trend and the experiments presented state for the first time that the enhanced collectivity persists at $N = 40$ for ^{66}Fe .

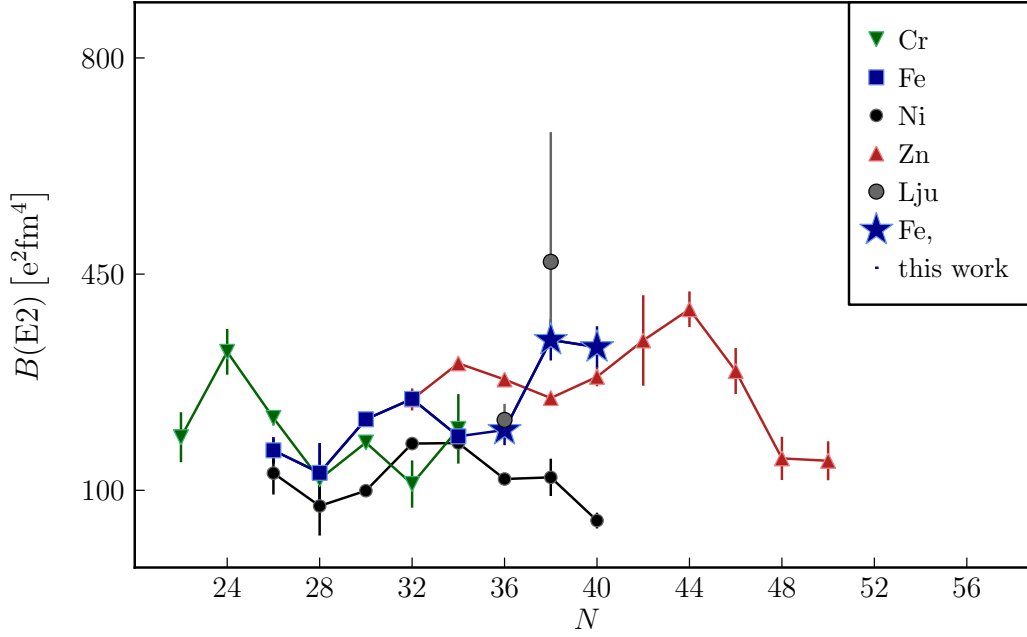


Figure 5.1: Experimental results and the nuclear neighbourhood. [1, 4, 9, 18, 22, 28, 29, 32, 33, 34, 40, 42, 45, 48]

A	τ [ps]	$B(E2)$ [$e^2\text{fm}^4$]	$B(E2)$ [$e^2\text{fm}^4$] _{Lju}
66	39.4(40)	332(34)	—
64	10.3(10)	344(33)	470^{+210}_{-110}
62	8.0(10)	198(25)	214(26)

Table 5.1: Experimental results compared to the values previously made available by Ljungvall et al. [33].

As illustrated in Figure 5.1 and Table 5.1, the present results agree very well within the errors given with the ones cited previously for ^{62}Fe . Ljungvall's major point is the increased collectivity at $N = 38$, here the new data present a significant improvement in terms of accuracy. The persistence of collectivity at ^{66}Fe , first reported based on this data set in [42], sheds a new light on the whole area. The present data set represents state of the art research on a statistically very sound and robust basis.

5.2 Interpretation of Results

Figures 5.2 and 5.3 show the experimental situation around $N = 40$ in terms of 2_1^+ energy and $B(E2)$ values where available. The first figure summarises the available energy information, the second one all that is known in terms of transition strength. The canonical shell closures at $N = 28$ and $N = 50$ can be observed as peaks in the 2_1^+ energy for all nuclei in the region, more explicitly for the doubly magic $^{56}_{28}\text{Ni}_{28}$. Similarly, a drop of transition strengths can be observed towards $N = 28$ and $N = 50$, while the latter one has still to be confirmed at a large neutron excess.

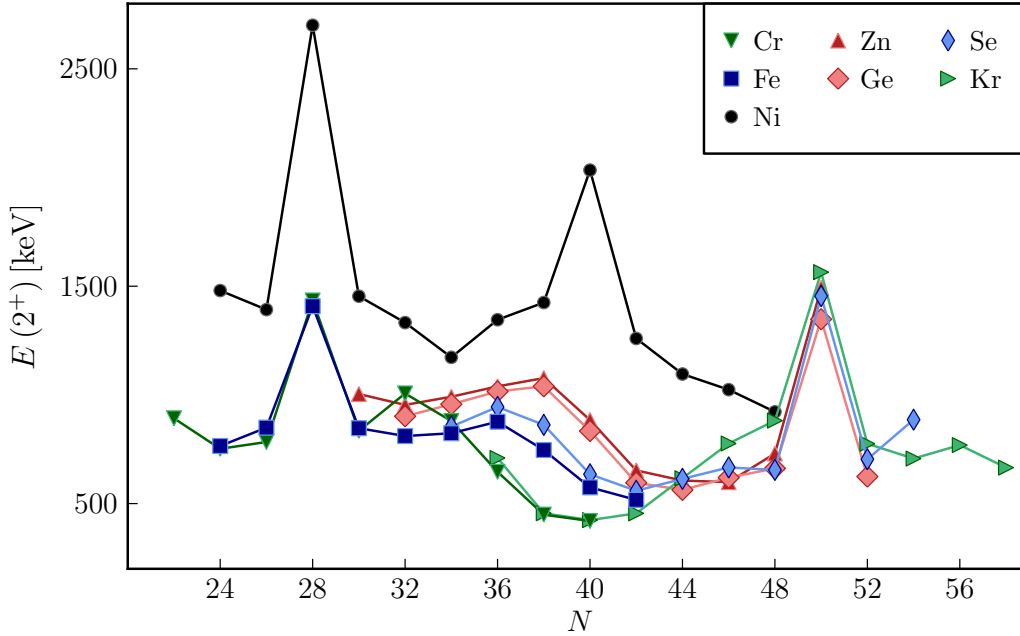


Figure 5.2: 2_1^+ Energies around $N = 40$ for Cr, Fe, Ni, Zn, Ge, Se, Kr. [1, 4, 9, 18, 22, 28, 29, 32, 34, 40, 42, 45, 48].

Apart from the magic numbers 2, 20, 28, 50, 82, 126, solutions of the three dimensional harmonic oscillator (2, 8, 20, 40, 70, ...) are still present in the underlying shell structure. The respective gaps are—apart from 2, 8 and 20—way smaller than the canonical ones, more steps than gaps, nonetheless they exist. The

harmonic oscillator “gap” at $N = 40$ and its evolution through the isotopic chains of the nuclear region is a subject of open debate [31]. Under pseudo doubly magic conditions¹, ${}^{68}_{28}\text{Ni}_{40}$, a clear peaking of the 2_1^+ energy is observed, similarly, the transition strength drops towards $N = 40$ for the Ni isotopes. None of these tendencies is observed in the neighbouring chains. Energies pass smoothly over the gap or show a reciprocal behaviour compared to that found in Ni. The rise in collectivity observed for neutron rich Fe, proton rich Kr and mid-shell Se, seems to contradict a subshell closure at $N = 40$.

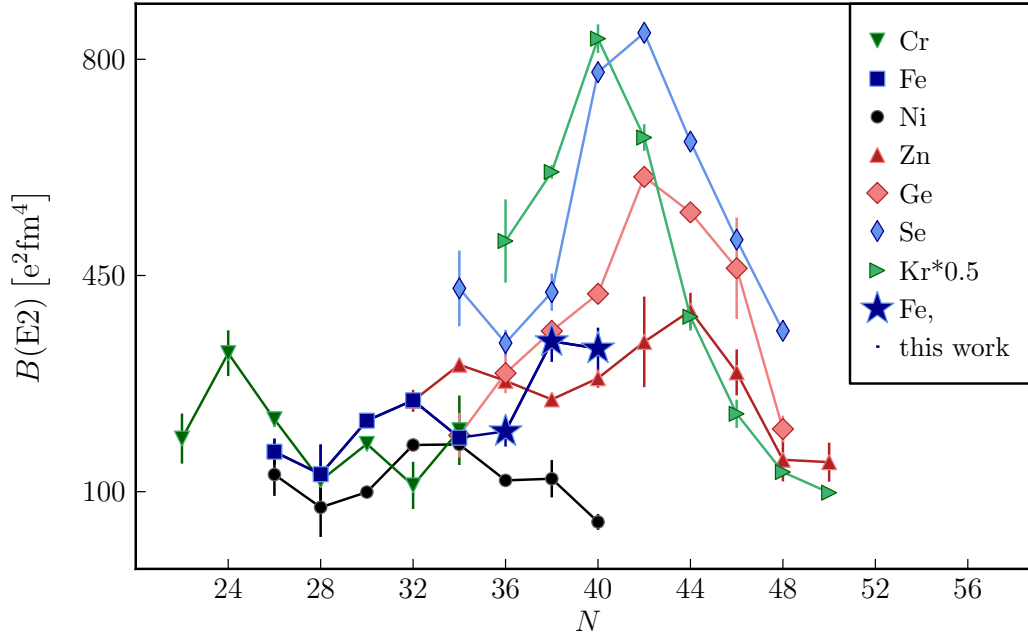


Figure 5.3: $B(E2; 0_1^+ \rightarrow 2_1^+)$ values around $N = 40$ for Cr, Fe, Ni, Zn, Ge, Se, Kr. [1, 4, 9, 18, 22, 28, 29, 32, 34, 40, 42, 45, 48].

¹shell-model magic in one species and harmonic oscillator magic in the other

5.2.1 Valence Proton Symmetry

The Valence Proton Symmetry (VPS) was introduced by Dewald et al. [17]. As a special case of the Valence Correlation Scheme [11], the VPS is a purely phenomenological approach to describe and predict transition probabilities in collective nuclei² at large and small isospin, respectively. The basic idea is to compare nuclei that have the same number of neutrons and the same number of valence protons, be it particles or holes. A schematic drawing is shown in Figure 5.4. For example, this makes $(_{48}\text{Cd}, _{52}\text{Te})$, $(_{46}\text{Pd}, _{54}\text{Xe})$, $(_{44}\text{Ru}, _{56}\text{Ba})$, $(_{42}\text{Mo}, _{58}\text{Nd})$ VPS partners. In the past, the symmetry has been applied to the region around $Z = 50$. Here, a very similar trend was observed for the behaviour of 2_1^+ energies of VPS partners, wherever there is an overlap. The partner's $B(E2)$ values need to be rescaled for the respective charge and mass ratios using $S = \frac{(Z_p/Z_h)^2}{A_p/A_h}$, where p, h indicate respectively the partner with proton holes and proton particles. This leads to a more than pleasing description for the Pd/Xe pair [17].

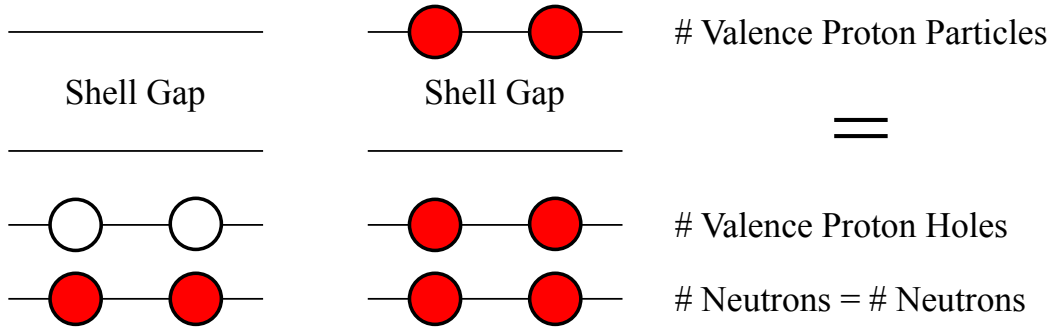


Figure 5.4: Both nuclei have the same number of neutrons. The number of valence proton particles, that is valence proton holes on the left hand side (open circles) or valence protons on the right hand side (red circles above the shell gap) is the same.

²where collective may be defined as complying to this description

Application to $Z = 28$

A short glance on the energies in Figure 5.2, leaves doubt in the canonical VPS partners around $Z = 28$, $({}_{26}\text{Fe}, {}_{30}\text{Zn})$, $({}_{24}\text{Cr}, {}_{32}\text{Ge})$. Obviously, the 2_1^+ energies do not align pairwise around ${}_{28}\text{Ni}$. But from the same plot, it becomes obvious that $({}_{26}\text{Fe}, {}_{34}\text{Se})$, $({}_{24}\text{Cr}, {}_{36}\text{Kr})$, $({}_{30}\text{Zn}, {}_{32}\text{Ge})$ align perfectly in their energy trend [28]. This leads to the assumption that a modified Valence proton symmetry with respect to $Z \approx 30$ is observed. Indeed, rescaling the partner's $B(E2)$ values accordingly to the respective charge and mass ratios³ using $S = \frac{(Z_L/Z_H)^2}{A_L/A_H}$ yields a pleasing agreement between the partner's trends in collectivity, wherever an overlap exists. The results are plotted in Figure 5.5. It has to be noted that this description is completely parameter free. Taking that into consideration, the lighter Se isotopes follow the trend given by ${}^{60,62}\text{Fe}$ quite well. For heavier iron nuclei, overall scale and trend are depicted correctly. So far, no transition probabilities for heavy Cr isotopes are known, no overlap between the scaled Kr and measured Cr data exists.

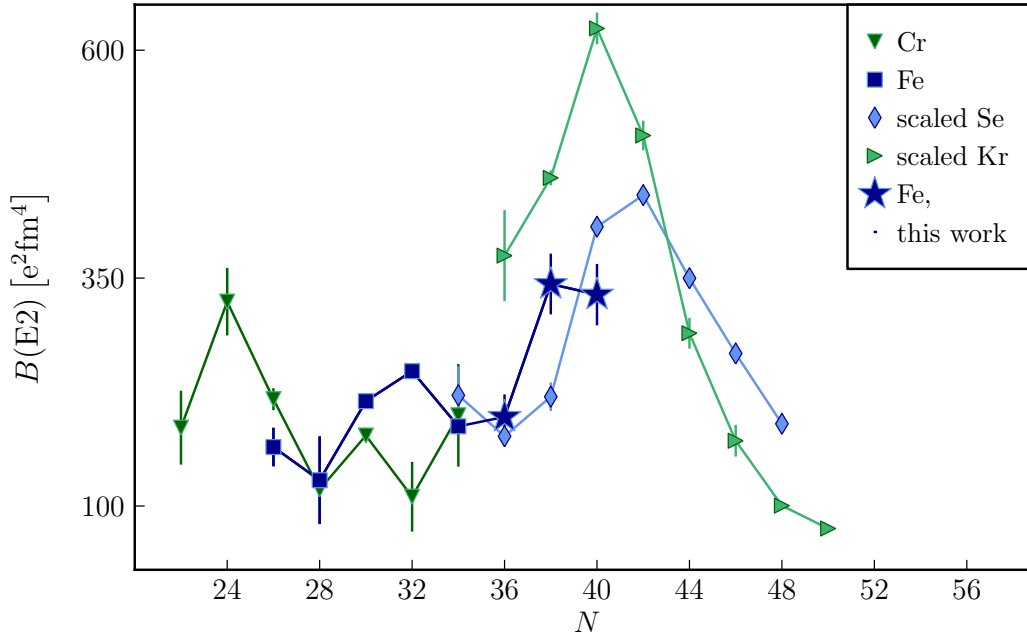


Figure 5.5: The modified Valence Proton Symmetry applied to Kr and Se in comparison to Cr and Fe [1, 4, 9, 18, 22, 28, 29, 32, 34, 40, 42, 45].

³where L, H indicate respectively the lighter/heavier partner

Symmetry with respect to $Z \approx 30$

The shift of the symmetry by two protons may be understood by studying the deformed shell structure [27] between $Z = 28$ and $Z = 50$ (cf. Figure 5.6 for a schematic drawing).

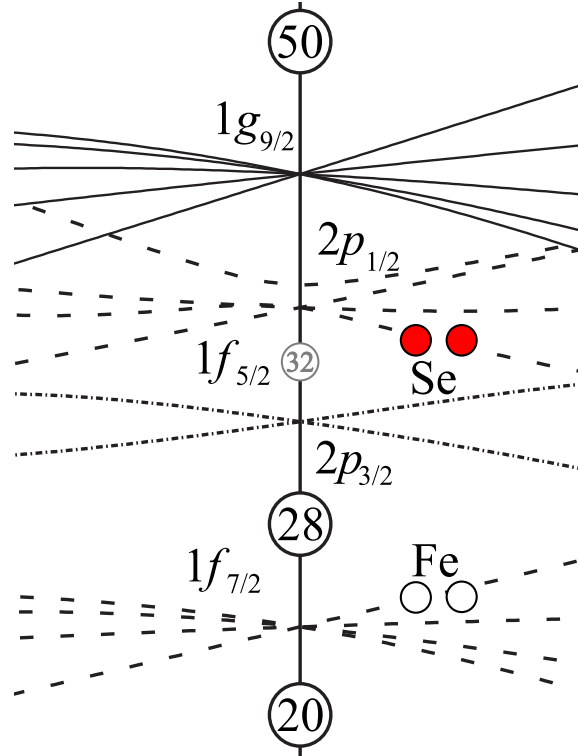


Figure 5.6: Schematic of the relevant Nilsson orbits. The vertical axis gives the level energy, the horizontal axis the deformation, centred around the spherical shape, both in arbitrary units. A detailed account can be found in the table of isotopes [19].

The following general observations can be made:

- The $2p_{3/2}$ shell lies isolated between $1f_{5/2}$ and $1f_{7/2}$. Nuclei occupying states in the $2p_{3/2}$ are expected to be dominated by the shell and are not expected to show collective behaviour. This is confirmed by the behaviour of the scaled $B(E2)$ for the supposed $(_{30}\text{Zn},_{32}\text{Ge})$ pair shown in Figure 5.7, the agreement is less pleasing than the paragon pairs $(_{26}\text{Fe},_{34}\text{Se})$, $(_{24}\text{Cr},_{36}\text{Kr})$.

Collectivity is the prime prerequisite for the VPS to apply, the isolation of the $2p_{3/2}$ shell makes it less suitable for this kind of phenomenology.

- However, a fully occupied $2p_{3/2}$ shell has no influence on deformation whatsoever, deformation driving and inhibiting effects cancel out to a large extent. This shifts the symmetry axis by two protons, making Fe and Se VPS partners, as highlighted in Figure 5.6.

The modified Valence Proton Symmetry with respect to $Z \approx 30$, first presented in [42], is a parameter free phenomenological description of the structure around $N = 40$ in Fe, Se, Cr and Kr. The scaled selenium values represent a prediction for the behaviour of even heavier iron nuclei. Analogously are the scaled krypton values a prediction for the behaviour of heavy chromium nuclei.

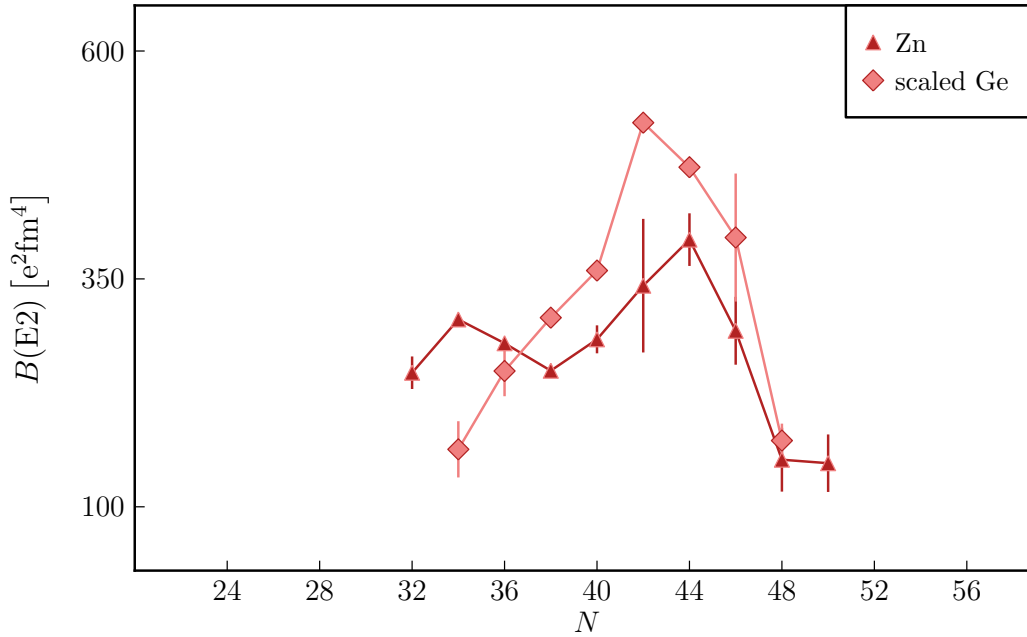


Figure 5.7: The modified Valence Proton Symmetry applied to Ge in comparison to Zn[18, 48].

5.2.2 Shell Model

The nuclear shell-model delivers excellent descriptions of nuclear structure. Calculations are based on an inert core and nucleons occupying orbits outside of this core, the valence nucleons and valence orbits (forming the valence space). Basically, a Hamiltonian of the form

$$H = H_{Core} + H_{Valence}$$

is considered. The spherical core has one of the canonical magic numbers 2, 20, 28, 50, 82, 126 [35] for protons and neutrons. The interactions in the valence space lead to collectivity, deformation and even to shifts in magic numbers [13] (redefining the core, of course).

To show its full power, the shell-model needs a large valence space and a realistic effective interaction between the valence nucleons. Increasing the size of the valence space is a problem of computation time and machine power. With increasing computing power this problem is reduced. Anticipating the discussion below, the valence space nowadays available to Lenzi et al. [31] was out of reach at the time of the calculations from [13]. The shaping and use of state-of-the-art nucleon-nucleon interactions is a skill on its own. It requires experience and a high degree of familiarity with the specific computer code in use.

The main feature of the interaction introduced in [31], named LNPS, is to be a so called *hybrid*. A hybrid interaction becomes necessary because a main focus of the work is to use a large valence space. This hybrid combines no less than three sets of realistic two-body interactions. Each is shaped to cover a subspace of the desired valence space. Special care was taken to match the effective single-particle energies to experimental constraints of the target region around $N = 40$ that were known before. The interaction was not fit to the present data for $^{62,64,66}\text{Fe}$.

Previous attempts to describe this region theoretically failed. On Hartree-Fock [24] and on shell-model basis [13] it was not possible to reproduce the experimentally observed rapid onset of deformation when removing proton pairs from semi-magic ^{64}Ni . The necessity to include the $1d_{5/2}$ orbital into the valence space

to describe the heavier Fe isotopes properly was first discussed in [13]. As hinted above, limitations in machine power forced Caurier et al. [13] to truncate the valence space further when including the high-lying $1d_{5/2}$ shell. A semi-magic $^{52}_{20}\text{Ca}_{32}$ core was used. When choosing a core, double-magicity is a prime criterion. So, the doubly-magic $^{48}_{20}\text{Ca}_{28}$ core would have been the first choice. It allows neutron excitations from the $1p_{3/2}$ shell into the valence space.

The last years brought great advances in computing power. Nowadays, up to 14 particle-14 hole excitations are possible on a ^{48}Ca core. This encompasses the full pf shell for protons and the $pfgd$ space (i.e. $0f_{5/2}$, $1p_{3/2}$, $1p_{1/2}$, $0g_{9/2}$, $1d_{5/2}$) for neutrons. The dimensions of the matrices involved may reach up to 10^{10} .

S. M. Lenzi contributed shell-model calculations for $^{62,64,66}\text{Fe}$ using the LNPS interaction to [42]. The results are summarised in Table 5.2 and compared to present experimental $B(E2)$ values and $E(2^+_1)$ values from [34].

A	τ [ps]	$E(2^+_1)$ [keV]	$E(2^+_1)_{\text{LNPS}}$ [keV]	$B(E2)$ [e ² fm ⁴]	$B(E2)_{\text{LNPS}}$ [e ² fm ⁴]
66	39.4(40)	575	570	332(34)	421
64	10.3(10)	746	747	344(33)	344
62	8.0(10)	877	835	198(25)	270

Table 5.2: Present experimental results compared to the shell model calculations using the LNPS interaction[31]. $E(2^+_1)$ values were taken from [34], $B(E2)_{\text{LNPS}}$ are from [42].

The agreement for the level energies of the more collective nuclei $^{64,66}\text{Fe}$ is tremendous. ^{62}Fe agrees within 5%. The $B(E2)$ for ^{64}Fe is reproduced exactly. $^{66,62}\text{Fe}$ agree within two, respectively three sigma. The rapid change of collectivity and the large valence space makes shell model calculations in this mass region extremely difficult. As the present data were neither considered in the fitting procedure nor in the modelling of the LNPS interaction, this is felt to be a particularly successful description.

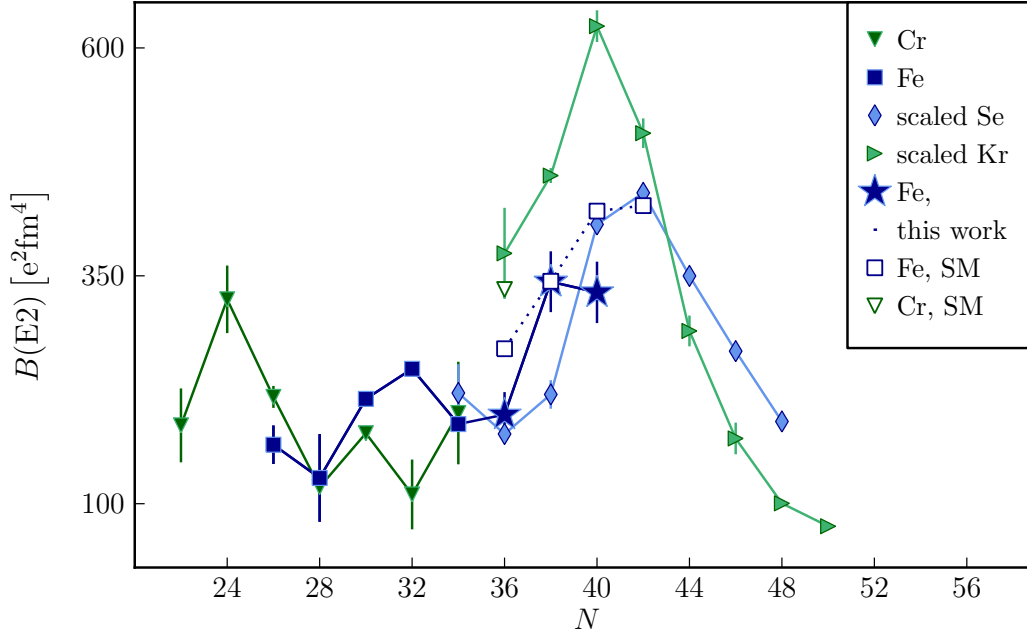


Figure 5.8: Recent shell model results (SM) compared to the present experimental data and the modified Valence Proton Symmetry applied to Kr and Se [1, 4, 9, 18, 22, 28, 29, 32, 34, 40, 42, 45].

Comparing shell model results with VPS predictions we find a striking agreement, as shown in Figure 5.8. The calculations for ^{68}Fe coincide exactly with the VPS prediction for scaled Se nuclei at $N = 42$. The LNPS value for ^{60}Cr fits perfectly into the scaled Kr chain at $N = 36$. Thus, we find fundamental support for our phenomenological description from the shell-model calculations.

5.3 Summary

Lifetimes of the 2_1^+ states in $^{62,64,66}\text{Fe}$ were measured model independently at the National Superconducting Cyclotron Laboratory. The previously known value for ^{62}Fe could be confirmed, for ^{64}Fe the experimental error was significantly reduced (compared to Ljungvall et al. [33]). The lifetime of the 2_1^+ state in ^{66}Fe was measured for the first time in this experiment [42]. This represents state of the art experiments on the very cutting edge of science.

A dedicated lineshape simulation tool implementing the Doppler shift attenuation effects in target and degrader, the relativistic Lorentz Boost and the solid angle subtended by the detectors was written. The program can deal with an arbitrary order of discretisation, in the case of this work a total of 36 steps was sufficient.

On the basis of the new and previously available $B(E2)$ data the development of collectivity throughout the mass region was discussed. The onset of collectivity for neutron rich iron isotopes at $N = 38$ reported by Ljungvall et al. could be confirmed whilst significantly improving the experimental error. Furthermore, it could be shown for the first time ([42]), that the collectivity persists at $N = 40$.

The scarceness of data for nuclei so far from stability inhibits our understanding of nuclear structure in this region. It is difficult to access with computational approaches. The straight forward modified Valence Proton Symmetry yields a description of collective nuclei in the region, except for the Zn/Ge pair for the reasons given. The level of agreement reached between a parameter free phenomenological approach and a shell-model calculation is astonishing. The LNPS shell model calculation is in beautiful agreement with the experimental data presented in this work, considering that this region of the nuclear chart proved so far particularly resistant to calculational approaches.

Appendix A

Lineshape Simulation of Plunger Data

A.1 General Considerations

We consider four different regimes, where the projectile is:

- in the target (nT, Δ_T)
- in flight between target and degrader (nF, Δ_F)
- in the degrader (nD, Δ_D)
- behind the degrader (afterwards) (nA, Δ_A).

Each of these is divided in n^* intervals of length Δ_* as illustrated in Figure A.1.

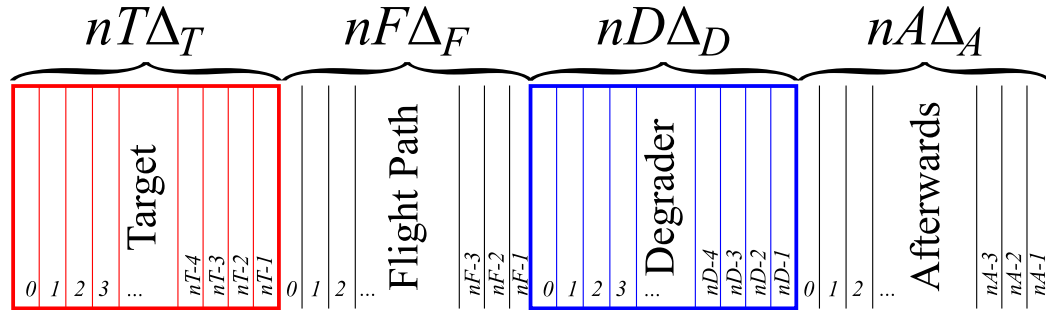


Figure A.1: Discretisation of target, degrader and run-out path

The projectile's velocity is assumed to be constant over the length of each of these. The intervals are consecutively numbered starting from zero. (The m -th element of the "Afterwards" will have the number $nT + nF + nD + m - 1$). The first point of the first interval is called s_0 , the first point of the second interval s_1 and so on.

The velocity in interval i is the velocity the projectile has when entering that interval. Thus, the velocity in the very first interval ($i = 0$) is the velocity of the original beam. Velocities¹ are given in terms of $\beta_i = v_i/c$. The lifetime τ must not be confused with the observed lifetime τ_{lab} in the laboratory frame. Their relation is of course given by $\tau = \sqrt{1 - \beta_i^2} \tau_{lab}$. Decays we observe are of the form $e^{-t/\tau_{lab}} = e^{-t \sqrt{1 - \beta_i^2}/\tau}$.

A.2 The Amplitudes

The basic concept of the simulation is to populate a unit number of nuclei in each interval of target and degrader and let it subsequently start to decay.

A.2.1 Excitation

A.2.1.1 Excitation in the target

Decay in the target To keep the notation simple we introduce the following abbreviation which will be used with $i \in [0, nT]$:

$$\frac{\Delta_T \sqrt{1 - \beta_i^2}}{\beta_i c \tau} = arg_{T_i}(\tau) = arg_{T_i} \quad (A.1)$$

The amplitude originating from decays in the first segment of the target is given by:

$$\begin{aligned} a_0 &= \text{decays on the line segment } \overline{s_0 s_1} \\ &= 1 - e^{-arg_{T_0}} \end{aligned}$$

¹Calculation of velocities is discussed in 4.1

where 1 is the initial population in the segment and e^{-argT_0} is the remainder of the population after the passage. Their difference is obviously the number of nuclei that decayed.

Analogously the amplitude originating from decays in the second segment of the target is given by:

$$\begin{aligned} a_1 &= \text{decays on the segment } \overline{s_1 s_2} \\ &= 1 - e^{-argT_1} + \left[1 - e^{-(argT_0 + argT_1)} - (1 - e^{-argT_0}) \right] \\ &= 1 - e^{-argT_1} + \left[e^{-argT_0} - e^{-(argT_0 + argT_1)} \right] \end{aligned}$$

where 1 is the initial population from the segment $\overline{s_1 s_2}$ and e^{-argT_1} is the remainder of that population after the passage through that segment.

$$1 - e^{-(argT_0 + argT_1)} \quad (\text{A.2})$$

is the number of nuclei populated in the segment $\overline{s_0 s_1}$ minus the number of nuclei that are remaining after the passage through $\overline{s_0 s_2}$.

$$(1 - e^{-argT_0}) \quad (\text{A.3})$$

gives, as indicated above, the number of nuclei that were populated and decayed in $\overline{s_0 s_1}$. The difference between equation A.2 and equation A.3 is the number of nuclei that were populated in $\overline{s_0 s_1}$ and decayed in $\overline{s_1 s_2}$.

Consequently, the amplitude originating from decays in the i -th segment—where $i \in [0, nT - 1]$ —of the target is given by:

$$a_i = \text{decays in the segment } \overline{s_i s_{i+1}} \quad (\text{A.4})$$

$$= 1 - e^{-argT_i} + \sum_{j=0}^{i-1} \left[e^{-\sum_{k=j}^{i-1} argT_k} - e^{-\sum_{k=j}^i argT_k} \right] \quad (\text{A.5})$$

$$= \sum_{j=0}^i \left[e^{-\sum_{k=j}^{i-1} argT_k} - e^{-\sum_{k=j}^i argT_k} \right] \quad (\text{A.6})$$

To obtain the unit population in the i -th segment, $\sum_{k=i}^0 \arg T_k = 0$ must be fulfilled in the software implementation of the last line. This may be circumvented by using the penultimate equation.

Decay in flight For each segment of the flightpath we consider decays from population in each segment of the target individually. This leads to $nT * nF$ expressions $b_{i,j}$, where $i \in [0, nF - 1]$, $j \in [0, nT - 1]$ and:

$$b_{i,j} = \begin{array}{l} \text{decays in the segment } \overline{s_{(nT+i)} s_{(nT+i+1)}} \\ \text{of nuclei that were excited in } \overline{s_j s_{j+1}} \end{array}$$

Analogously to equation A.1 we introduce:

$$\frac{\Delta_F \sqrt{1 - \beta_{nT}^2}}{\beta_{nT} c \tau} = \arg_F(\tau) = \arg_F \quad (\text{A.7})$$

The number of decays in the first segment of the flight path originating from nuclei that were populated in the first segment of the target is:

$$\begin{aligned} b_{0,0} &= \begin{array}{l} \text{decays in the segment } \overline{s_{(nT)} s_{(nT+1)}} \\ \text{of nuclei that were excited in } \overline{s_0 s_1} \end{array} \\ &= \left(1 - e^{-(\sum_{i=0}^{nT-1} \arg T_i) - \arg_F} \right) - \left(1 - e^{-\sum_{i=0}^{nT-1} \arg T_i} \right) \\ &= e^{-\sum_{i=0}^{nT-1} \arg T_i} - e^{-(\sum_{i=0}^{nT-1} \arg T_i) - \arg_F} \end{aligned}$$

where the first expression in the second line is the number of nuclei that have been populated in segment one of the target and have not decayed after the passage through the first segment of the flight path. The second expression is the number of nuclei that were populated in the first segment of the target and had not decayed at the beginning of the first segment of the flight path. The difference between the two is the number of nuclei that have been populated in the first segment of the target and decayed in the first segment of the flight path.

In general terms:

$$\begin{aligned}
b_{i,j} &= \text{decays in the segment } \overline{s_{(nT+i)} s_{(nT+i+1)}} \\
&\quad \text{of nuclei that were excited in } \overline{s_j s_{j+1}} \\
&= \left(1 - e^{-\left(\sum_{k=j}^{nT-1} \arg T_k\right) - (i+1) \arg F} \right) - \left(1 - e^{-\sum_{k=j}^{nT-1} \arg T_k - i \arg F} \right) \\
&= e^{-\sum_{k=j}^{nT-1} \arg T_k - i \arg F} - e^{-\left(\sum_{k=j}^{nT-1} \arg T_k\right) - (i+1) \arg F}
\end{aligned}$$

Decay in the degrader For each segment of the degrader we consider decays from population in each segment of the target individually. This leads to $nT * nD$ expressions $c_{i,j}$, where $i \in [0, nD - 1]$, $j \in [0, nT - 1]$.

Analogously to equation A.1 we introduce:

$$\frac{\Delta_D \sqrt{1 - \beta_{(nT+i)}^2}}{\beta_{(nT+i)} c \tau} = \arg_{D_i}(\tau) = \arg_{D_i} \quad (\text{A.8})$$

which will be used with $i \in [0, nD]$

We obtain in general terms:

$$\begin{aligned}
c_{i,j} &= \text{decays in the segment } \overline{s_{(nT+nF+i)} s_{(nT+nF+i+1)}} \\
&\quad \text{of nuclei that were excited in } \overline{s_j s_{j+1}} \\
&= + \left(1 - e^{-\left(\sum_{k=j}^{nT-1} \arg T_k\right) - nF \arg F - \sum_{k=0}^{i+1} \arg D_k} \right) \\
&\quad - \left(1 - e^{-\left(\sum_{k=j}^{nT-1} \arg T_k\right) - nF \arg F - \sum_{k=0}^i \arg D_k} \right) \\
&= e^{-\left(\sum_{k=j}^{nT-1} \arg T_k\right) - nF \arg F - \sum_{k=0}^i \arg D_k} - e^{-\left(\sum_{k=j}^{nT-1} \arg T_k\right) - nF \arg F - \sum_{k=0}^{i+1} \arg D_k}
\end{aligned}$$

Decay afterwards For each segment after the degrader we consider decays from population in each segment of the target individually. This leads to $nT * nA$ expressions $d_{i,j}$, where $i \in [0, nA - 1]$, $j \in [0, nT - 1]$.

Analogously to equation A.1 we introduce:

$$\frac{\Delta_A \sqrt{1 - \beta_{(nT+nD)}^2}}{\beta_{(nT+nD)} c \tau} = \arg_A(\tau) = \arg_A \quad (\text{A.9})$$

We obtain in general terms:

$$\begin{aligned} d_{i,j} &= \text{decays in the segment } \overline{s_{(nT+nF+nD+i)} s_{(nT+nF+nD+i+1)}} \\ &\quad \text{of nuclei that were excited in } \overline{s_j s_{j+1}} \\ &= + \left(1 - e^{-\left(\sum_{k=j}^{nT-1} \arg T_k\right) - nF \arg F - \sum_{k=0}^{nD-1} \arg D_k - (i+1) \arg A} \right) \\ &\quad - \left(1 - e^{-\left(\sum_{k=j}^{nT-1} \arg T_k\right) - nF \arg F - \sum_{k=0}^{nD-1} \arg D_k - i \arg A} \right) \\ &= + e^{-\left(\sum_{k=j}^{nT-1} \arg T_k\right) - nF \arg F - \sum_{k=0}^{nD-1} \arg D_k - i \arg A} \\ &\quad - e^{-\left(\sum_{k=j}^{nT-1} \arg T_k\right) - nF \arg F - \sum_{k=0}^{nD-1} \arg D_k - (i+1) \arg A} \end{aligned}$$

A.2.1.2 Excitation in the degrader

Decay in the degrader Excitation and subsequent decay of nuclei in the degrader is treated in strict analogy to paragraph A.2.1.1. Using equation A.8 the amplitude originating from decays in the i -th segment of the degrader—where $i \in [0, nD - 1]$ —is given by:

$$\begin{aligned} f_i &= \text{decays on the segment } \overline{s_{(nT+nF+i)} s_{(nT+nF+i+1)}} \\ &\quad \text{of states that were excited in the degrader} \\ &= 1 - e^{-\arg D_i} + \sum_{j=0}^{i-1} \left[e^{-\sum_{k=j}^{i-1} \arg D_k} - e^{-\sum_{k=j}^i \arg D_k} \right] \\ &= \sum_{j=0}^i \left[e^{-\sum_{k=j}^{i-1} \arg D_k} - e^{-\sum_{k=j}^i \arg D_k} \right] \end{aligned}$$

To obtain the unit population in the i -th segment, $\sum_{k=i}^0 \arg D_k = 0$ must be fulfilled in the software implementation of the last line. This may be circumvented by using the penultimate equation.

Decay afterwards The decay of states excited in the degrader after having passed the degrader is again treated analogously to the reaction on the target (cf. paragraph A.2.1.1). Using equation A.9 the amplitude originating from decays in the i -th segment of the path after the degrader of states populated in the j -th segment—where $i \in [0, nA - 1]$ and $j \in [0, nD - 1]$ —is given by:

$$\begin{aligned}
 h_{i,j} &= \text{decays in the segment } \overline{s_{(nT+nF+nD+i)} s_{(nT+nF+nD+i+1)}} \\
 &\quad \text{of nuclei that were excited in } \overline{s_{(nT+nF+j)} s_{(nT+nF+nD+j+1)}} \\
 &= \left(1 - e^{-\left(\sum_{k=j}^{nD-1} \arg D_k\right) - (i+1)\arg A} \right) - \left(1 - e^{-\sum_{k=j}^{nD-1} \arg D_k - i\arg A} \right) \\
 &= e^{-\sum_{k=j}^{nD-1} \arg D_k - i\arg A} - e^{-\left(\sum_{k=j}^{nD-1} \arg D_k\right) - (i+1)\arg A}
 \end{aligned}$$

A.2.2 Angles

The length of the flight path is significant in intermediate beam energy experiments. Therefore emission angles cannot be assumed to be constant over the whole path. As target and degrader are thin compared to their separation it is legitimate to assume that the emission angle is constant over target and degrader, respectively.

Let the degrader centre be the origin, let z_0 be the projection of the detector position on the beam axis (positive in forward, negative in backward angles), x_0 the projection on the horizontal axis and $z = nF * \Delta_F$ be the separation between target and degrader. y_0 may be assumed to be zero without loss of generality.

Target and degrader angles

The angle between target and detector is given by:

$$\cos(\theta_T) = \frac{z_0 + \frac{nD}{2} \Delta_D + (nF \Delta_F) + \left(\frac{nT}{2} \Delta_T\right)}{\sqrt{\left(z_0 + \frac{nD}{2} \Delta_D + (nF \Delta_F) + \left(\frac{nT}{2} \Delta_T\right)\right)^2 + x_0^2}} \quad (\text{A.10})$$

analogously the angle between the centre of the degrader and detector is given by:

$$\cos(\theta_D) = \frac{z_0}{\sqrt{z_0^2 + x_0^2}} \quad (\text{A.11})$$

There is no sign ambiguity left here, as z_0 has a different sign for forward and backward angles. The obtained angle is always counted with respect to the positive z -axis.

Angles on flightpath and afterwards

The angle from the centre of the i -th segment of the flightpath is given by:

$$\cos(\theta_{F_i}) = \frac{z_0 + \left(\frac{nD}{2} \Delta_D\right) - \frac{\Delta_F}{2} + (nF - 1 - i) \Delta_F}{\sqrt{\left(z_0 + \left(\frac{nD}{2} \Delta_D\right) - \frac{\Delta_F}{2} + (nF - 1 - i) \Delta_F\right)^2 + x_0^2}} \quad (\text{A.12})$$

The angle from the centre of the i -th segment after the degrader is given by:

$$\cos(\theta_{A_i}) = \frac{z_0 - \left(\frac{nD}{2} \Delta_D\right) + \frac{\Delta_A}{2} - (i \Delta_A)}{\sqrt{\left(z_0 - \left(\frac{nD}{2} \Delta_D\right) + \frac{\Delta_A}{2} - (i \Delta_A)\right)^2 + x_0^2}} \quad (\text{A.13})$$

A.2.3 Energies

Emission in the target

The observed energy for emission from the i -th segment of the target is:

$$E_{T_i} = \frac{E_0 \sqrt{1 - \beta_i^2}}{1 - \beta_i \cos(\theta_T)} \quad (\text{A.14})$$

Emission in flight

For the emission in the i -th segment of the flightpath we obtain:

$$E_{F_i} = \frac{E_0 \sqrt{1 - \beta_{(nT)}^2}}{1 - \beta_{(nT)} \cos(\theta_{F_i})} \quad (\text{A.15})$$

Emission in the degrader

Analogously the observed energy for the emission from the i -th segment of the degrader is:

$$E_{D_i} = \frac{E_0 \sqrt{1 - \beta_{(i+nT)}^2}}{1 - \beta_{(i+nT)} \cos(\theta_D)} \quad (\text{A.16})$$

Emission afterwards

And we obtain for the emission in the i -th segment of the path after the degrader:

$$E_{A_i} = \frac{E_0 \sqrt{1 - \beta_{(nT+nD)}^2}}{1 - \beta_{(nT+nD)} \cos(\theta_{A_i})} \quad (\text{A.17})$$

A.2.4 Efficiencies

The detection efficiency is depending on:

- Lorentz boost
- Solid Angle, $\epsilon_{\Omega}(z)$
- Detector efficiency, $\epsilon_{\text{Ge}}(E)$

Lorentz boost [30] and solid angle [26] are calculated, the detector efficiency is fit. In analogy to A.2.3 the Lorentz boost is given below:

Emission in the target

For emission from the i -th segment of the target:

$$\epsilon_{T_i} = \frac{1 - \beta_i^2}{(1 - \beta_i^2 \cos(\theta_T))^2} \quad (\text{A.18})$$

Emission in flight

For emission in the i -th segment of the flightpath:

$$\epsilon_{F_i} = \frac{1 - \beta_{(nT)}^2}{(1 - \beta_{(nT)}^2 \cos(\theta_{F_i}))^2} \quad (\text{A.19})$$

Emission in the degrader

For emission from the i -th segment of the degrader:

$$\epsilon_{D_i} = \frac{1 - \beta_{(i+nT)}^2}{(1 - \beta_{(i+nT)}^2 \cos(\theta_D))^2} \quad (\text{A.20})$$

Emission afterwards

For emission in the i -th segment of the path after the degrader:

$$\epsilon_{A_i} = \frac{1 - \beta_{(nT+nD)}^2}{(1 - \beta_{(nT+nD)}^2 \cos(\theta_{A_i}))^2} \quad (\text{A.21})$$

A.3 Spectra

A.3.1 Individual segments

A.3.1.1 Excitation in the target

Emission in the target

$$g_{a_i} = \frac{a_i \varepsilon_\Omega \left(\frac{nD}{2} \Delta_D + (nF \Delta_F) + \left(\frac{nT}{2} \Delta_T \right) \right) \varepsilon_{\text{Ge}}(E) \varepsilon_{T_i} e^{-\frac{(x-E_{T_i})^2}{2\sigma_T^2}}}{\sigma_T \sqrt{2\pi}}$$

Emission in flight

$$g_{b_{i,j}} = \frac{b_{i,j} \varepsilon_\Omega \left(\frac{nD}{2} \Delta_D - \frac{\Delta_F}{2} + (nF - 1 - i) \Delta_F \right) \varepsilon_{\text{Ge}}(E) \varepsilon_{F_i} e^{-\frac{(x-E_{F_i})^2}{2\sigma_T^2}}}{\sigma_T \sqrt{2\pi}}$$

Emission in the degrader

$$g_{c_{i,j}} = \frac{c_{i,j} \varepsilon_\Omega(0) \varepsilon_{\text{Ge}}(E) \varepsilon_{D_i} e^{-\frac{(x-E_{D_i})^2}{2\sigma_T^2}}}{\sigma_T \sqrt{2\pi}}$$

Emission afterwards

$$g_{d_{i,j}} = \frac{d_{i,j} \varepsilon_\Omega \left(-\frac{nD}{2} \Delta_D + \frac{\Delta_A}{2} - i \Delta_A \right) \varepsilon_{\text{Ge}}(E) \varepsilon_{A_i} e^{-\frac{(x-E_{A_i})^2}{2\sigma_T^2}}}{\sigma_T \sqrt{2\pi}}$$

A.3.1.2 Excitation in the degrader

Emission in the degrader

$$g_{f_i} = \frac{f_i \varepsilon_\Omega \left(\left(\frac{nT}{2} \Delta_T \right) + (nF \Delta_F) + \frac{nD \Delta_D}{2} \right) \varepsilon_{\text{Ge}}(E) \varepsilon_{D_i} e^{-\frac{(x-E_{D_i})^2}{2\sigma_D^2}}}{\sigma_D \sqrt{2\pi}}$$

Emission afterwards

$$g_{h_{i,j}} = \frac{h_{i,j} \varepsilon_\Omega \left(\left(\frac{nT}{2} \Delta_T \right) + (nF \Delta_F) + (nD \Delta_D) - \frac{\Delta_A}{2} + (i \Delta_A) \right) \varepsilon_{\text{Ge}}(E) \varepsilon_{A_i} e^{-\frac{(x-E_{A_i})^2}{2\sigma_D^2}}}{\sigma \sqrt{2\pi}}$$

A.3.2 Lineshape Function

$$g_{Target} = \mathcal{N} \left(\sum_{i=0}^{nT-1} g_{a_i} + \sum_{j=0}^{nT-1} \sum_{i=0}^{nF-1} g_{b_{i,j}} + \sum_{j=0}^{nT-1} \sum_{i=0}^{nD-1} g_{c_{i,j}} + \sum_{j=0}^{nT-1} \sum_{i=0}^{nA-1} g_{d_{i,j}} \right) \quad (\text{A.22})$$

$$g_{Degrader} = \mathcal{N} \mathbb{D} \frac{\Delta_T}{\Delta_D} \left(\sum_{i=0}^{nD-1} g_{f_i} + \sum_{j=0}^{nD-1} \sum_{i=0}^{nA-1} g_{h_{i,j}} \right) \quad (\text{A.23})$$

$$g(E, x, \mathcal{N}, \mathbb{D}, \sigma_T, \sigma_D) = g_{Target} + g_{Degrader} \quad (\text{A.24})$$

$g(E, x, \mathcal{N}, \mathbb{D}, \sigma_T, \sigma_D)$ is the lineshape function that is fit to the data set for a given ring, preferably simultaneously to all distances and all rings. \mathcal{N} is the scaling factor and \mathbb{D} is the ratio between excitation on degrader and target. This is especially not the ratio between the yields from these two. Typically, \mathcal{N} , \mathbb{D} , σ_T and σ_D will be fit parameters. $\frac{\Delta_T}{\Delta_D}$ is the ratio between target and degrader thicknesses. Remember, that in each interval a unit number of nuclei is populated.

Bibliography

- [1] ADRICH, P.; AMTHOR, A. M.; BAZIN, D.; BOWEN, M. D.; BROWN, B. A.; CAMPBELL, C. M.; COOK, J. M.; GADE, A.; GALAVIZ, D.; GLASMACHER, T.; MCDANIEL, S.; MILLER, D.; OBERTELLI, A.; SHIMBARA, Y.; SIWEK, K. P.; TOSTEVIN, J. A. ; WEISSHAAR, D.: In-beam gamma-ray spectroscopy and inclusive two-proton knockout cross section measurements at $N \approx 40$. In: *Phys. Rev. C* 77 (2008), May, No. 5, 054306–6. <http://link.aps.org/abstract/PRC/v77/e054306> 64, 65, 66, 68, 73
- [2] ALEXANDER, T. K.; ALLEN, K. W.: Lifetimes of the ^{16}O 6.13-MeV level and the ^{17}O 0.871-MeV level. In: *Canadian Journal of Physics* 43 (1965), 1563+. <http://dx.doi.org/doi:10.1139/p65-148>. – DOI doi:10.1139/p65-148 14
- [3] ALEXANDER, T.K.; BELL, A.: A target chamber for recoil-distance lifetime measurements. In: *Nuclear Instruments and Methods* 81 (1970), May, No. 1, 22–26. <http://www.sciencedirect.com/science/article/B73DN-471XPYG-S4/1/a9b049e2e61643c268504c25d016f8aa> 16
- [4] AOI, N.; TAKESHITA, E.; SUZUKI, H.; TAKEUCHI, S.; OTA, S.; BABA, H.; BISHOP, S.; FUKUI, T.; HASHIMOTO, Y.; ONG, H. J.; IDEGUCHI, E.; IEKI, K.; IMAI, N.; ISHIHARA, M.; IWASAKI, H.; KANNO, S.; KONDO, Y.; KUBO, T.; KURITA, K.; KUSAKA, K.; MINEMURA, T.; MOTOBAYASHI, T.; NAKABAYASHI, T.; NAKAMURA, T.; NAKAO, T.; NIIKURA, M. ; OKUMURA, T.: Development of Large Deformation in ^{62}Cr . In: *Phys. Rev. Lett.*

- 102 (2009), January, No. 1, 012502–. <http://link.aps.org/doi/10.1103/PhysRevLett.102.012502> 64, 65, 66, 68, 73
- [5] BATEMAN, H.: Solution of a system of differential equations occurring in the theory of radioactive transformations. In: *Proc. Cambridge Philos. Soc.* 15 (1910), S. 423–427 45
- [6] BAZIN, D.; CAGGIANO, J. A.; SHERRILL, B. M.; YURKON, J.; ZELLER, A.: The S800 spectrograph. In: *Nuclear Instruments and Methods in Physics Research Section B: Beam Interactions with Materials and Atoms* 204 (2003), May, 629–633. <http://www.sciencedirect.com/science/article/B6TJN-47RYJ82-2/2/6e4743dc558fb4f3abaeecac2d4df956>. – ISSN 0168–583X 25
- [7] BERZ, M.; JOH, K.; NOLEN, J. A.; SHERRILL, B. M. ; ZELLER, A. F.: Reconstructive correction of aberrations in nuclear particle spectrographs. In: *Phys. Rev. C* 47 (1993), February, No. 2, 537–. <http://link.aps.org/doi/10.1103/PhysRevC.47.537> 26
- [8] BETHE, H.: Zur Theorie des Durchgangs schneller Korpuskularstrahlen durch Materie. In: *Ann. Phys.* 397 (1930), No. 3, 325–400. <http://dx.doi.org/10.1002/andp.19303970303>. – ISSN 1521–3889 24
- [9] BÜRGER, A.; SAITO, T.R.; GRAWE, H.; HÜBEL, H.; REITER, P.; GERL, J.; GÓRSKA, M.; WOLLERSHEIM, H.J.; AL-KHATIB, A.; BANU, A.; BECK, T.; BECKER, F.; BEDNARCZYK, P.; BENZONI, G.; BRACCO, A.; BRAMBILLA, S.; BRINGEL, P.; CAMERA, F.; CLÉMENT, E.; DOORNENBAL, P.; GEISSEL, H.; GÖRGEN, A.; GREBOSZ, J.; HAMMOND, G.; HELLSTRÖM, M.; HONMA, M.; KAVATSYUK, M.; KAVATSYUK, O.; KMIECIK, M.; KOJOUHAROV, I.; KORTEN, W.; KURZ, N.; LOZEVA, R.; MAJ, A.; MANDAL, S.; MILLION, S. B. and M. B. and Muralithar; NEUŠER, A.; NOWACKI, F.; OTSUKA, T.; PODOLYÁK, Zs.; SAITO, N.; SINGH, A.K.; WEICK, H.; WHELDON, C.; WIELAND, O. ; WINKLER, M.: Relativistic

- Coulomb excitation of neutron-rich $^{54,56,58}\text{Cr}$: On the pathway of magicity from $N = 40$ to $N = 32$. In: *Physics Letters B* 622 (2005), August, No. 1-2, 29–34. <http://www.sciencedirect.com/science/article/B6TVN-4GMBG1G-1/2/79c85815c7c39d11a1c753f5e86110c5>. – ISSN 0370–2693 64, 65, 66, 68, 73
- [10] CALI, J. P.: Standard Reference Material 4218-C / National Institute of Standards. 1978 41
- [11] CASTEN, R. F.; ZAMFIR, N. V.: Valence correlation schemes and signatures of nuclear structure: A simple global phenomenology for $B(E2 : 2_1^+ \rightarrow 0_1^+)$ values. In: *Phys. Rev. Lett.* 70 (1993), January, No. 4, 402–. <http://link.aps.org/doi/10.1103/PhysRevLett.70.402> 67
- [12] CASTEN, Richard F.: *Nuclear Structure from a Simple Perspective*. 2nd. Oxford University Press, 2000. – 422–425 S. 7
- [13] CAURIER, E.; NOWACKI, F. ; POVES, A.: Large-scale shell model calculations for exotic nuclei. In: *The European Physical Journal A - Hadrons and Nuclei* 15 (2002), September, No. 1, 145–150. <http://dx.doi.org/10.1140/epja/i2001-10243-7> 7, 71, 72
- [14] CHESTER, A.; ADRICH, P.; BECERRIL, A.; BAZIN, D.; CAMPBELL, C.M.; COOK, J.M.; DINCA, D.-C.; MUELLER, W.F.; MILLER, D.; MOELLER, V.; NORRIS, R.P.; PORTILLO, M.; STAROSTA, K.; STOLZ, A.; TERRY, J.R.; ZWAHLEN, H.; VAMAN, C. ; DEWALD, A.: Application of the time-of-flight technique for lifetime measurements with relativistic beams of heavy nuclei. In: *Nuclear Instruments and Methods in Physics Research Section A: Accelerators, Spectrometers, Detectors and Associated Equipment* 562 (2006), June, No. 1, 230–240. <http://www.sciencedirect.com/science/article/B6TJM-4JHVMN2-H/2/5b35b9fb447c356c1240ee7315c0b319>. – ISSN 0168–9002 15, 18
- [15] DEWALD, A.; HARISSOPULOS, S. ; BRENTANO, P. von: The differential plunger and the differential decay curve method for the analysis of recoil

- distance Doppler-shift data. In: *Zeitschrift für Physik A Hadrons and Nuclei* 334 (1989), June, No. 2, 163–175. <http://dx.doi.org/10.1007/BF01294217> 45
- [16] DEWALD, A.; JOLIE, J.; PISSULLA, T.; ILIE, G.; FRANSEN, C.; MELON, B.; PETKOV, P.; TONEV, D.; STAROSTA, K.; GADE, A.; GLASMACHER, T.; WEISSHAAR, D.; MILLER, D.; ADRICH, P.; BROWN, B. A.; CHESTER, A.; VAMAN, C.; VOSS, P.; MARGINEAN, N.; GADEA, A.; DE ANGELIS, G.; UR, C. A. ; LISETSKIY, A. F.: *NSCL Proposal for: Recoil-distance lifetime measurement in neutron rich Fe isotopes using intermediate energy Coulomb excitation* 22
- [17] DEWALD, A.; STAROSTA, K.; PETKOV, P.; HACKSTEIN, M.; ROTHER, W.; ADRICH, P.; AMTHOR, A. M.; BAUMANN, T.; BAZIN, D.; BOWEN, M.; CHESTER, A.; DUNOMES, A.; GADE, A.; GALAVIZ, D.; GLASMACHER, T.; GINTER, T.; HAUSMANN, M.; JOLIE, J.; MELON, B.; MILLER, D.; MOELLER, V.; NORRIS, R. P.; PISSULLA, T.; PORTILLO, M.; SHIMBARA, Y.; STOLZ, A.; VAMAN, C.; VOSS, P. ; WEISSHAAR, D.: Collectivity of neutron-rich palladium isotopes and the valence proton symmetry. In: *Phys. Rev. C* 78 (2008), November, No. 5, 051302–5. <http://link.aps.org/abstract/PRC/v78/e051302> 8, 15, 18, 46, 67
- [18] ENSDF: Evaluated Nuclear Structure Data File. In: <http://www.nndc.bnl.gov/ensdf> 42, 64, 65, 66, 68, 70, 73
- [19] FIRESTONE, Richard B.; S.Y. FRANK CHU, Coral M. B. (Hrsg.): *Table of Isotopes CD-ROM*. 8th, 1998 Update. Wiley Interscience, 1998 69
- [20] FRISCH, O.: In: *Britisch Atomic Energy Report* BR-49 (1944) 27
- [21] GADE, A.; BAZIN, D.; CAMPBELL, C. M.; CHURCH, J. A.; DINCA, D. C.; ENDERS, J.; GLASMACHER, T.; HU, Z.; KEMPER, K. W.; MUELLER, W. F.; OLLIVER, H.; PERRY, B. C.; RILEY, L. A.; ROEDER, B. T.; SHERRILL, B. M. ; TERRY, J. R.: Detailed experimental study on intermediate-energy Coulomb excitation of ^{46}Ar . In: *Phys. Rev. C* 68 (2003), July, No. 1,

- 014302–. <http://link.aps.org/doi/10.1103/PhysRevC.68.014302> 17
- [22] GADE, A.; JANSSENS, R. V. F.; BAUGHER, T.; BAZIN, D.; BROWN, B. A.; CARPENTER, M. P.; CHIARA, C. J.; DEACON, A. N.; FREEMAN, S. J.; GRINYER, G. F.; HOFFMAN, C. R.; KAY, B. P.; KONDEV, F. G.; LAURITSEN, T.; MCDANIEL, S.; MEIERBACHTOL, K.; RATKIEWICZ, A.; STROBERG, S. R.; WALSH, K. A.; WEISSHAAR, D.; WINKLER, R.; ZHU, S.: Collectivity at $N = 40$ in neutron-rich ^{64}Cr . In: *Phys. Rev. C* 81 (2010), May, No. 5, 051304–. <http://link.aps.org/doi/10.1103/PhysRevC.81.051304> 64, 65, 66, 68, 73
- [23] GADE, Alexandra; GLASMACHER, Thomas: In-beam nuclear spectroscopy of bound states with fast exotic ion beams. In: *Progress in Particle and Nuclear Physics* 60 (2008), January, No. 1, 161–224. <http://www.sciencedirect.com/science/article/B6TJC-4PGY4TY-1/2/8bda5d0f9deafcf12ea8552015773cb2>. – ISSN 0146–6410 16
- [24] GAUDEFROY, L.; OBERTELLI, A.; PÉRU, S.; PILLET, N.; HILAIRE, S.; DELAROCHE, J. P.; GIROD, M.; LIBERT, J.: Collective structure of the $N = 40$ isotones. In: *Phys. Rev. C* 80 (2009), December, No. 6, 064313–. <http://link.aps.org/doi/10.1103/PhysRevC.80.064313> 71
- [25] GLASMACHER, T.: Coulomb excitation at intermediate energies. In: *Annual Review of Nuclear and Particle Science* 48 (1998), December, No. 1, 1–31. <http://dx.doi.org/10.1146/annurev.nucl.48.1.1>. – ISSN 0163–8998 16
- [26] GUEST, P. G.: The Solid Angle Subtended by a Cylinder. In: *Rev. Sci. Instrum.* 32 (1961), February, No. 2, 164–165. <http://link.aip.org/link/?RSI/32/164/1> 53, 86
- [27] GUSTAFSON, C.; LAMM, I. L.; NILSSON, B.; NILSSON, S. G.: Nuclear deformabilities in the rare-earth and actinide regions with excursions off the

- stability line and into the super-heavy region. In: *Arkiv För Fysik* 36 (1966), September, No. 69, S. 613–627 69
- [28] HOTELING, N.; WALTERS, W. B.; JANSSENS, R. V. F.; BRODA, R.; CARPENTER, M. P.; FORNAL, B.; HECHT, A. A.; HJORTH-JENSEN, M.; KRÓLAS, W.; LAURITSEN, T.; PAWLSTROKAT, T.; SEWERYNIAK, D.; WANG, X.; WÖHR, A.; WRZESINACUTESKI, J. ; ZHU, S.: Yrast structure of ^{64}Fe . In: *Phys. Rev. C* 74 (2006), December, No. 6, 064313–. <http://link.aps.org/doi/10.1103/PhysRevC.74.064313> 64, 65, 66, 68, 73
- [29] JONES, E. F.; GORE, P. M.; HAMILTON, J. H.; RAMAYYA, A. V.; HWANG, J. K.; DELIMA, A. P.; ZHU, S. J.; BEYER, C. J.; LUO, Y. X.; MA, W. C.; RASMUSSEN, J. O.; LEE, I. Y.; WU, S. C.; GINTER, T. N.; STOYER, M.; COLE, J. D.; DANIEL, A. V.; TER-AKOPIAN, G. M. ; DONANGELO, R.: Identification of ^{88}Se and new levels in $^{84,86}\text{Se}$. In: *Phys. Rev. C* 73 (2006), January, No. 1, 017301–. <http://link.aps.org/doi/10.1103/PhysRevC.73.017301> 64, 65, 66, 68, 73
- [30] LARMOR, Joseph: A Dynamical Theory of the Electric and Luminiferous Medium. Part III. Relations with Material Media. In: *Philosophical Transactions of the Royal Society of London. Series A, Containing Papers of a Mathematical or Physical Character* 190 (1897), 205–493. <http://rsta.royalsocietypublishing.org/content/190/205.short> 45, 47, 86
- [31] LENZI, S. M.; NOWACKI, F.; POVES, A. ; SIEJA, K.: Island of inversion around ^{64}Cr . In: *Phys. Rev. C* 82 (2010), November, No. 5, 054301–. <http://link.aps.org/doi/10.1103/PhysRevC.82.054301> 9, 66, 71, 72
- [32] LJUNGVALL, J.; GÖRGEN, A.; GIROD, M.; DELAROCHE, J.-P.; DEWALD, A.; DOSSAT, C.; FARNEA, E.; KORTEN, W.; MELON, B.; MENEGAZZO, R.; OBERTELLI, A.; ORLANDI, R.; PETKOV, P.; PISSULLA, T.; SIEM, S.; SINGH, R. P.; SREBRNY, J.; THEISEN, Ch.; UR, C. A.; VALIENTE-DOBÓN,

- J. J.; ZELL, K. O. ; ZIELIŃSKA, M.: Shape Coexistence in Light Se Isotopes: Evidence for Oblate Shapes. In: *Phys. Rev. Lett.* 100 (2008), March, No. 10, 102502–. <http://link.aps.org/doi/10.1103/PhysRevLett.100.102502> 64, 65, 66, 68, 73
- [33] LJUNGVALL, J.; GÖRGEN, A.; OBERTELLI, A.; KORTEN, W.; CLÉMENT, E.; FRANCE, G. de; BÜRGER, A.; DELAROCHE, J.-P.; DEWALD, A.; GADEA, A.; GAUDEFROY, L.; GIROD, M.; HACKSTEIN, M.; LIBERT, J.; MENGONI, D.; NOWACKI, F.; PISSULLA, T.; POVES, A.; RECCHIA, F.; REJMUND, M.; ROTHER, W.; SAHIN, E.; SCHMITT, C.; SHRIVASTAVA, A.; SIEJA, K.; VALIENTE-DOBÓN, J. J.; ZELL, K. O. ; ZIELIŃSKA, M.: Onset of collectivity in neutron-rich Fe isotopes: Toward a new island of inversion? In: *Phys. Rev. C* 81 (2010), June, No. 6, 061301–. <http://link.aps.org/doi/10.1103/PhysRevC.81.061301> 21, 63, 64, 75
- [34] LUNARDI, S.; LENZI, S. M.; VEDOVA, F. D.; FARNEA, E.; GADEA, A.; MARGINEAN, N.; BAZZACCO, D.; BEGHINI, S.; BIZZETI, P. G.; BIZZETI-SONA, A. M.; BUCURESCU, D.; CORRADI, L.; DEACON, A. N.; ANGELLIS, G. d.; FIORETTO, E.; FREEMAN, S. J.; IONESCU-BUJOR, M.; IORDACHESCU, A.; MASON, P.; MENGONI, D.; MONTAGNOLI, G.; NAPOLI, D. R.; NOWACKI, F.; ORLANDI, R.; POLLAROLO, G.; RECCHIA, F. ; SCARLASSARA, F.: Spectroscopy of neutron-rich Fe isotopes populated in the $^{64}\text{Ni} + ^{238}\text{U}$ reaction. In: *Phys. Rev. C* 76 (2007), September, No. 3, 034303–. <http://link.aps.org/doi/10.1103/PhysRevC.76.034303> 42, 64, 65, 66, 68, 72, 73
- [35] MAYER-GOEPPERT, Maria: On Closed Shells in Nuclei. II. In: *Phys. Rev.* 75 (1949), June, No. 12, 1969–. <http://link.aps.org/doi/10.1103/PhysRev.75.1969> 7, 71
- [36] MILLER, P.; MARTI, F.; POE, D.; STEINER, M.; STETSON, J. ; WU, X.Y.: Commissioning of the Coupled Cyclotron Facility at NSCL. In: *Particle Accelerator Conference, 2001. PAC 2001. Proceedings of the 2001 DOI - 10.1109/PAC.2001.987829* Bd. 4, 2001, S. 2557–2559 vol.4 12

- [37] MORRISSEY, D. J.; SHERRILL, B. M.; STEINER, M.; STOLZ, A. ; WIEDENHOEVER, I.: Commissioning the A1900 projectile fragment separator. In: *Nuclear Instruments and Methods in Physics Research Section B: Beam Interactions with Materials and Atoms* 204 (2003), May, 90–96. <http://www.sciencedirect.com/science/article/B6TJN-47J4JSW-G/2/f6c4327a123246d7510eae7f414a9d42>. – ISSN 0168–583X 12
- [38] MORRISSEY, David J.; SHERRILL, Bradley M.: Radioactive Nuclear Beam Facilities Based on Projectile Fragmentation. In: *Philosophical Transactions: Mathematical, Physical and Engineering Sciences* 356 (Sep. 15, 1998), No. 1744, 1985–2006. <http://www.jstor.org/stable/55109>. – ISSN 1364503X 7
- [39] MUELLER, W. F.; CHURCH, J. A.; GLASMACHER, T.; GUTKNECHT, D.; HACKMAN, G.; HANSEN, P. G.; HU, Z.; MILLER, K. L. ; QUIRIN, P.: Thirty-two-fold segmented germanium detectors to identify γ -rays from intermediate-energy exotic beams. In: *Nuclear Instruments and Methods in Physics Research Section A: Accelerators, Spectrometers, Detectors and Associated Equipment* 466 (2001), July, No. 3, 492–498. <http://www.sciencedirect.com/science/article/B6TJM-43KBJ1J-8/2/48cdfb18ad236d485031aa4e59feffed>. – ISSN 0168–9002 13
- [40] OBERTELLI, A.; BAUGHER, T.; BAZIN, D.; DELAROCHE, J. P.; FLAVIGNY, F.; GADE, A.; GIROD, M.; GLASMACHER, T.; GOERGEN, A.; GRINYER, G. F.; KORTEN, W.; LJUNGVALL, J.; MCDANIEL, S.; RATKIEWICZ, A.; SULIGNANO, B. ; WEISSHAAR, D.: Shape evolution in self-conjugate nuclei, and the transitional nucleus ^{68}Se . In: *Phys. Rev. C* 80 (2009), September, No. 3, 031304–. <http://link.aps.org/doi/10.1103/PhysRevC.80.031304> 64, 65, 66, 68, 73
- [41] OTSUKA, Takaharu; SUZUKI, Toshio; HONMA, Michio; UTSUNO, Yutaka; TSUNODA, Naofumi; TSUKIYAMA, Koshiroh ; HJORTH-JENSEN, Morten: Novel Features of Nuclear Forces and Shell Evolution in Exotic Nuclei. In:

- Phys. Rev. Lett.* 104 (2010), January, No. 1, 012501–. <http://link.aps.org/doi/10.1103/PhysRevLett.104.012501> 7
- [42] ROTHER, W.; DEWALD, A.; IWASAKI, H.; LENZI, S. M.; STAROSTA, K.; BAZIN, D.; BAUGHER, T.; BROWN, B. A.; CRAWFORD, H. L.; FRANSEN, C.; GADE, A.; GINTER, T. N.; GLASMACHER, T.; GRINYER, G. F.; HACKSTEIN, M.; ILIE, G.; JOLIE, J.; MCDANIEL, S.; MILLER, D.; PETKOV, P.; PISSULLA, Th.; RATKIEWICZ, A.; UR, C. A.; VOSS, P.; WALSH, K. A.; WEISSHAAR, D. ; ZELL, K.-O.: Enhanced Quadrupole Collectivity at $N = 40$: The Case of Neutron-Rich Fe Isotopes. In: *Phys. Rev. Lett.* 106 (2011), January, No. 2, 022502–. <http://link.aps.org/doi/10.1103/PhysRevLett.106.022502> 64, 65, 66, 68, 70, 72, 73, 75
- [43] STAROSTA, K.; DEWALD, A.; DUNOMES, A.; ADRICH, P.; AMTHOR, A. M.; BAUMANN, T.; BAZIN, D.; BOWEN, M.; BROWN, B. A.; CHESTER, A.; GADE, A.; GALAVIZ, D.; GLASMACHER, T.; GINTER, T.; HAUSMANN, M.; HOROI, M.; JOLIE, J.; MELON, B.; MILLER, D.; MOELLER, V.; NORRIS, R. P.; PISSULLA, T.; PORTILLO, M.; ROTHER, W.; SHIMBARA, Y.; STOLZ, A.; VAMAN, C.; VOSS, P.; WEISSHAAR, D. ; ZELEVINSKY, V.: Shape and Structure of $N=Z^{64}\text{Ge}$: Electromagnetic Transition Rates from the Application of the Recoil Distance Method to a Knock-out Reaction. In: *Phys. Rev. Lett.* 99 (2007), July, No. 4, 042503–4. <http://link.aps.org/abstract/PRL/v99/e042503> 8, 15, 46
- [44] STAROSTA, K.; VAMAN, C.; MILLER, D.; VOSS, P.; BAZIN, D.; GLASMACHER, T.; CRAWFORD, H.; MANTICA, P.; TAN, H.; HENNIG, W.; WALBY, M.; FALLU-LABRUYERE, A.; HARRIS, J.; BREUS, D.; GRUDBERG, P. ; WARBURTON, W.K.: Digital Data Acquisition System for experiments with segmented detectors at National Superconducting Cyclotron Laboratory. In: *Nuclear Instruments and Methods in Physics Research Section A: Accelerators, Spectrometers, Detectors and Associated Equipment* 610 (2009), November, No. 3, 700–709. <http://www.sciencedirect.com/science/article/>

B6TJM-4X7GM97-2/2/d7c662703703dd11e3b5b5a8175de442.
– ISSN 0168-9002 13

- [45] T. RZACA-URBAN; W. URBAN; A. KACZOR; J.L. DURELL; M.J. LEDDY; M.A. JONES; W.R. PHILLIPS; A.G. SMITH; B.J. VARLEY; I. AHMAD; L.R. MORSS; M. BENTALEB; E. LUBKIEWICZ ; N. SCHULZ: Shapes of the neutron-rich $^{88-94}\text{Kr}$ nuclei. In: *Eur. Phys. J. A* 9 (2000), No. 2, 165-169. <http://dx.doi.org/10.1007/s100500070033>. – DOI 10.1007/s100500070033 64, 65, 66, 68, 73
- [46] TARASOV, O.B.; BAZIN, D.: LISE++ : design your own spectrometer. In: *Nuclear Physics A* 746 (2004). <http://dx.doi.org/10.1016/j.nuclphysa.2004.09.063>. – DOI 10.1016/j.nuclphysa.2004.09.063 12, 19, 47
- [47] TARASOV, O.B.; BAZIN, D.: LISE++: Radioactive beam production with in-flight separators. In: *Nuclear Instruments and Methods in Physics Research Section B: Beam Interactions with Materials and Atoms* 266 (2008), October, No. 19-20, 4657-4664. <http://www.sciencedirect.com/science/article/B6TJN-4SR7115-9/2/2812b311ac0f7b4d7b0066dc548acfdc>. – ISSN 0168-583X 12, 19, 47
- [48] WALLE, J. Van d.; AKSOUH, F.; BEHRENS, T.; BILDSTEIN, V.; BLAZHEV, A.; CEDERKÄLL, J.; CLÉMENT, E.; COCOLIOS, T. E.; DAVINSON, T.; DELAHAYE, P.; EBERTH, J.; EKSTRÖM, A.; FEDOROV, D. V.; FEDOSSEEV, V. N.; FRAILE, L. M.; FRANCHOO, S.; GERNHAUSER, R.; GEORGIEV, G.; HABS, D.; HEYDE, K.; HUBER, G.; HUYSE, M.; IBRAHIM, F.; IVANOV, O.; IWANICKI, J.; JOLIE, J.; KESTER, O.; KÖSTER, U.; KRÖLL, T.; KRÜCKEN, R.; LAUER, M.; LISETSKIY, A. F.; LUTTER, R.; MARSH, B. A.; MAYET, P.; NIEDERMAIER, O.; PANTEA, M.; RAABE, R.; REITER, P.; SAWICKA, M.; SCHEIT, H.; SCHRIEDER, G.; SCHWALM, D.; SELIVERSTOV, M. D.; SIEBER, T.; SLETTEN, G.; SMIRNOVA, N.; STANOIU, M.; STEFANESCU, I.; THOMAS, J.-C.; VALIENTE-DOBÓN, J. J.; DUPPEN, P. V.; VERNEY, D.; VOULOT, D.; WARR, N.; WEISSHAAR, D.; WENANDER, F;

- WOLF, B. H. ; ZIELINACUTESKA, M.: Low-energy Coulomb excitation of neutron-rich zinc isotopes. In: *Phys. Rev. C* 79 (2009), January, No. 1, 014309–. <http://link.aps.org/doi/10.1103/PhysRevC.79.014309> 64, 65, 66, 70
- [49] WARNER, David: Nuclear physics: Not-so-magic numbers. In: *Nature* 430 (2004), July, No. 6999, 517–519. <http://dx.doi.org/10.1038/430517a>. – ISSN 0028–0836 7
- [50] WINTHER, Aage; ALDER, Kurt: Relativistic coulomb excitation. In: *Nuclear Physics A* 319 (1979), May, No. 3, 518–532. <http://www.sciencedirect.com/science/article/B6TVB-473M8N3-MP/2/fccb05628855a4c400357b0ca6a7eaf>. – ISSN 0375–9474 11, 16, 46
- [51] YURKON, J.; BAZIN, D.; BENENSON, W.; MORRISSEY, D. J.; SHERRILL, B. M.; SWAN, D. ; SWANSON, R.: Focal plane detector for the S800 high-resolution spectrometer. In: *Nuclear Instruments and Methods in Physics Research Section A: Accelerators, Spectrometers, Detectors and Associated Equipment* 422 (1999), February, No. 1-3, 291–295. <http://www.sciencedirect.com/science/article/B6TJM-3VR1CVW-23/2/7753723b7fa2e6fd2c3eb18627ee6905>. – ISSN 0168–9002 25

Dank

Mein besonderer Dank gilt Prof. Dr. Jan Jolie für die Vergabe und Betreuung dieser Arbeit. Prof. Dr. Achim Rosch danke ich für seine Bereitschaft, der Prüfungskommission vorzusitzen. Priv.-Doz. Dr. Alfred Dewald hat mir großzügig die Möglichkeit gegeben, in seiner Plungergruppe mitzuarbeiten, dafür danke ich ihm. Die Arbeit in dieser Gruppe hat mir viel Freude bereitet.

Mit eindrucksvoller Geduld hat meine Frau Judith die letzten drei Jahre über sich ergehen lassen. Vielen Dank.

Vielen Dank für konstruktive Gespräche auch an meine Kollegen Matthias Hackstein, Thomas Pissulla, Andreas Wendt und die Kaffeebude in der Chemie.

Dr. Christoph Fransen und Dr. Andrey Blazhev standen immer für Fragen zur Verfügung, vielen Dank.

Unter meinen Koautoren gilt mein besonderer Dank Prof. Dr. Krzysztof Starosta, Phil Voss, Prof. Dr. Hironori Iwasaki, Prof. Dr. Pavel Petkov, Prof. Dr. Silvia M. Lenzi, Dr. Dirk Weißhaar und Andrew Ratkiewicz. Danke auch an Dr. D. Bazin, T. Baugher, Prof. Dr. B. A. Brown, H. L. Crawford, Prof. Dr. A. Gade, Dr. T. N. Ginter, Prof. Dr. T. Glasmacher, Dr. G. F. Grinyer, Dr. G. Ilie, S. McDaniel, Dr. D. Miller, Dr. C. A. Ur, K. A. Walsh und vor allem an Dr. K.-O. Zell.

Für die Betreuung durch Prof. Dr. Evgeny Epelbaum und das gewährte Stipendium danke ich der Bonn-Cologne Graduate School of Physics and Astronomy.

Erklärung

Ich versichere, dass ich die von mir vorgelegte Dissertation selbstständig angefertigt, die benutzten Quellen und Hilfsmittel vollständig angegeben und die Stellen der Arbeit – einschließlich Tabellen, Karten und Abbildungen –, die anderen Werken im Wortlaut oder dem Sinn nach entnommen sind, in jedem Einzelfall als Entlehnung kenntlich gemacht habe; dass diese Dissertation noch keiner anderen Fakultät oder Universität zur Prüfung vorgelegen hat; dass sie – abgesehen von unten angegebenen Teilpublikationen – noch nicht veröffentlicht worden ist sowie, dass ich eine solche Veröffentlichung vor Abschluss des Promotionsverfahrens nicht vornehmen werde. Die Bestimmungen der Promotionsordnung sind mir bekannt. Die von mir vorgelegte Dissertation ist von Prof. Dr. Jan Jolie betreut worden.

Nachfolgende Teilpublikationen liegen vor:

ROTHER, W.; DEWALD, A.; IWASAKI, H.; LENZI, S. M.; STAROSTA, K.; BAZIN, D.; BAUGHER, T.; BROWN, B. A.; CRAWFORD, H. L.; FRANSEN, C.; GADE, A.; GINTER, T. N.; GLASMACHER, T.; GRINYER, G. F.; HACKSTEIN, M.; ILIE, G.; JOLIE, J.; MCDANIEL, S.; MILLER, D.; PETKOV, P.; PISSULLA, TH.; RATKIEWICZ, A.; UR, C. A.; VOSS, P.; WALSH, K. A.; WEISSHAAR, D.; ZELL, K.-O.: Enhanced Quadrupole Collectivity at $N=40$: The Case of Neutron-Rich Fe Isotopes. In: *Phys. Rev. Lett.* 106 (2011), Januar, Nr. 2, 022502.

ROTHER, W.; DEWALD, A.; IWASAKI, H.; LENZI, S. M.; STAROSTA, K.; BAZIN, D.; BAUGHER, T.; BROWN, B. A.; CRAWFORD, H. L.; FRANSEN, C.; GADE, A.; GINTER, T. N.; GLASMACHER, T.; GRINYER, G. F.; HACKSTEIN, M.; ILIE, G.; JOLIE, J.; MCDANIEL, S.; MILLER, D.; PETKOV, P.; PISSULLA, TH.; RATKIEWICZ, A.; UR, C. A.; VOSS, P.; WALSH, K. A.; WEISSHAAR, D.; ZELL, K.-O.: *Observation of isotonic symmetry for enhanced quadrupole collectivity in neutron-rich $^{62,64,66}\text{Fe}$ isotopes at $N=40$* . In: *arXiv:1006.5297v1 [nucl-ex]* (2010), Juni.

Lebenslauf

Name:	Wolfram Rother
Anschrift:	Weyertal 18 50937 Köln
Geburtsdatum und -ort:	05.03.1983
Geburtsort:	Krefeld
Familienstand:	Verheiratet
Email:	wolfram.rother@googlemail.com
Hoch-/Schulbildung:	
Seit SS 2007	Mitglied der Bonn Cologne Graduate School of Physics and Astronomy Diplom Physiker, Gesamtnote „sehr gut“ (22.08.2008; Note: 1,1) Diplomarbeit: „Development of a New Recoil Distance Technique using Coulomb Excitation in Inverse Kinematics“ (Note: 1,0)
2003 - 2008	Studium der Physik, Universität zu Köln Vordiplom, Gesamtnote „sehr gut“ (30.08.2005; Note: 1,4)
2002 - 2003	Ausbildung zum staatlich geprüften Rettungssanitäter im Rahmen des Zivildienstes beim Deutschen Roten Kreuz, Neuss.
2002	Abitur, Gymnasium am Moltkeplatz zu Krefeld
Berufliche Laufbahn:	
Seit 2008	Institut für Kernphysik, Universität zu Köln, Wissenschaftlicher Mitarbeiter
2006 - 2008	Institut für Kernphysik, Universität zu Köln, Studentische Hilfskraft
Auslandserfahrung:	
WS 2005/2006	Auslandssemester als Stipendiat der französischen Regierung, Université Blaise Pascal, Clermont-Ferrand, Frankreich
1999	Halbjähriger Aufenthalt, Pensionnat Jean-Baptiste de la Salle, Rouen, Frankreich
Veröffentlichungen	
2011	<ul style="list-style-type: none">• W. Rother, et al.: Phys. Rev. Lett. 106, 022502
2010	<ul style="list-style-type: none">• K. A. Gladnishki, et al.: Phys. Rev. C 82, 037302• L. Coquard, et al.: Phys. Rev. C 82, 024317• J. Ljungvall, et al.: Phys. Rev. C (Rapid) 81, 061301• M.G. Procter, et al.: Phys. Rev. C 81, 054320• P.J.R. Mason, et al.: Phys. Lett. B 683, 1, 17-20• G. Rainovski, et al.: Phys. Lett. B 683, 1, 11-16
2009	<ul style="list-style-type: none">• L. Coquard, et al.: Phys. Rev. C (Rapid) 80, 061304• D. Radeck, et al.: Phys. Rev. C 80, 044331• H. Iwasaki, et al.: Phys. Rev. Lett. 102, 202502• D. Miller, et al.: Phys. Rev. C 79, 054306• L. Bettermann, et al.: Phys. Rev. C 79, 034315
2008	<ul style="list-style-type: none">• A. Dewald, et al.: Phys. Rev. C (Rapid) 78, 051302• K. Starosta, et al.: Phys. Rev. Lett. 99, 042503• A. Costin, et al.: Phys. Rev. C 74, 067301